



NRL/MR/6720--00-8433

# Advanced Radiation Theory Support Annual Report 1999, Final Report

*Radiation Hydrodynamics Branch  
Plasma Physics Division*

May 22, 2000

Approved for public release; distribution unlimited.

20000605 143

# REPORT DOCUMENTATION PAGE

Form Approved  
OMB No. 0704-0188

Public reporting burden for this collection of information is estimated to average 1 hour per response, including the time for reviewing instructions, searching existing data sources, gathering and maintaining the data needed, and completing and reviewing the collection of information. Send comments regarding this burden estimate or any other aspect of this collection of information, including suggestions for reducing this burden, to Washington Headquarters Services, Directorate for Information Operations and Reports, 1215 Jefferson Davis Highway, Suite 1204, Arlington, VA 22202-4302, and to the Office of Management and Budget, Paperwork Reduction Project (0704-0188), Washington, DC 20503.

1. AGENCY USE ONLY (Leave Blank)		2. REPORT DATE May 22, 2000		3. REPORT TYPE AND DATES COVERED Final Report	
4. TITLE AND SUBTITLE Advanced Radiation Theory Support Annual Report 1999, Final Report				5. FUNDING NUMBERS	
6. AUTHOR(S) Radiation Hydrodynamics Branch					
7. PERFORMING ORGANIZATION NAME(S) AND ADDRESS(ES) Naval Research Laboratory Washington, DC 20375-5320				8. PERFORMING ORGANIZATION REPORT NUMBER NRL/MR/6720--00-8433	
9. SPONSORING/MONITORING AGENCY NAME(S) AND ADDRESS(ES) Defense Threat Reduction Agency 6801 Telegraph Road Alexandria, VA 22310				10. SPONSORING/MONITORING AGENCY REPORT NUMBER	
11. SUPPLEMENTARY NOTES This research was sponsored by the Defense Threat Reduction Agency under Job Order Title "Advanced Radiation Theory Support," MIPR No. 99-2011/1363.					
12a. DISTRIBUTION/AVAILABILITY STATEMENT Approved for public release; distribution unlimited.				12b. DISTRIBUTION CODE	
13. ABSTRACT (Maximum 200 words)  This program describes the work of the Radiation Hydrodynamics Branch during FY 99 in support of the DTRA PRS program. Critical issues covered are: (1) Theory and modeling of enhanced energy dissipation in Z-pinch plasmas, (2) Experimentally and theoretically comparing uniform fill versus annular shell gas puff behavior of a series of Ar:Ne mixture experiments on Saturn, (3) Large initial radius Z-pinch load behavior on Saturn, Double Eagle, and Decade Quad pulsed power machines, (4) Novel approaches for producing 10 keV photons from long pulse machines, and (5) Kinetic energy and viscous dissipation in moderate atomic number plasmas.					
14. SUBJECT TERMS Decade Quad Enhanced energy dissipation Diagnostic line ratios Long time implosions Large radius implosions Radiation MHD Transport coefficients Rayleigh-Taylor instability Plasma radiation source Z-pinch physics				15. NUMBER OF PAGES 142	
				16. PRICE CODE	
17. SECURITY CLASSIFICATION OF REPORT UNCLASSIFIED	18. SECURITY CLASSIFICATION OF THIS PAGE UNCLASSIFIED	19. SECURITY CLASSIFICATION OF ABSTRACT UNCLASSIFIED	20. LIMITATION OF ABSTRACT UL		

# CONTENTS

Executive Summary .....	v
I. Model of Enhanced Energy Deposition in a Z-pinch Plasma .....	1
II. Comparison of Radiative Properties and Stability of Uniform Fill Versus Annular Shell Z Pinches .....	51
III. Kinetic Energy Dissipation in Moderate Atomic Number Plasmas .....	91
IV. Performance Assessment for Decade Quad Gas Puff Loads .....	112
V. Novel Approach to Producing $\sim 10$ keV X Rays with Plasma Radiation Sources Powered by Long Pulse Drivers .....	124

## EXECUTIVE SUMMARY

This report describes the theory support of DTRA's Plasma Radiation Source (PRS) program carried out by NRL's Radiation Hydrodynamics Branch (Code 6720) in FY 1999. Included is work called for in DTRA MIPR 99-2011/1363, 6720 Radiation Theory Support and in Sandia National Laboratories document number BE-6078, Z-pinch Theory and Spectroscopy.

This year was a continuation of focussed efforts to design new experiments, to analyze the data from PRS experiments as it became available and warranted analysis, and to evaluate the results of experiments on existing machines with special emphasis on evaluating the feasibility of increasing x-ray yields using large radius PRS loads. As a result of these efforts, noteworthy strides were made in the areas of plasma diagnostics, model assessment, improved understanding of Z-pinch phenomena, and how these factors affect PRS load and experiment design.

Experiments in the 1970s revealed that the total radiation was often noticeably larger than the kinetic energy imparted to the PRS load. However, with the DTRA sponsored long pulse aluminum experiments recently performed on Saturn and promoted by Code 6720, the total radiative yields were not just noticeably larger, but factors of 3-4 times as large as the kinetic energy. This made it clear that there is indeed an additional source of enhanced energy coupling to the plasma load after stagnation. With the goal of harnessing this energy by properly designed future PRS loads, this Branch put extensive effort into understanding this phenomenon. In particular the work of Rudakov and Sudan, which attributes this additional energy to macroscopic magnetohydrodynamic turbulent pinch heating, has been extended to the point where the theory can now explain much of the post stagnation plasma behavior. One useful feature of this theory is that it eliminates the need to employ artifices to limit the radiative collapse behavior in our models. This is an exciting development in understanding Z-pinch behavior that has eluded the PRS community for over two decades.

The constant checking of model results against data analyses of carefully designed experiments, together with continuous critique of the assumptions that go into the models, has proven to be a good method for making sustained progress in a field as complex as PRS development. Past checking of the assumptions of our models by comparing with experiments



revealed the importance of discriminating between line broadening produced by turbulent plasma motion and that due to large ion temperatures. This is a challenging but important task. Knowing the source of this broadening is important because it reveals information about the distribution of energy between ions and electrons in the core plasma. If high ion temperatures are the source of this broadening, as predicted by our models, then their reduction will be a vital design goal for future experiments. Because the high ion temperatures extend the time it takes to ionize into the K-shell and because they promote plasma cooling due to softer x-ray emission from the L-shell, their influence will especially effect those experiments intended to produce copious high energy,  $> 8keV$ , x rays. Our Branch continues to focus on this important issue; special attention was paid to designing novel loads that reduce this ionization time as well as to assessing the physics that is needed in modeling of the development and structure of shock fronts in these plasmas.

In order to design large radius loads that radiate efficiently, it is important that the large radius experiments be properly diagnosed and analyzed. To aid in the accomplishment of this goal, software was developed that automates and speeds up the routine analysis of data from Ar puff shots. This accomplishment allows inferences of vital pinch parameters such as temperature, density, and mass participation, to be made within minutes after each shot. At present very few DTRA experiments are so carefully analyzed and quantified. The feasibility of transferring this software to the PRS community at large is now being explored and discussed.

In this report the progress made in model development and assessment, and in diagnostic development for the purpose of improving our understanding of large radius Z pinch behavior is discussed section by section:

(1) It was concluded from early experiments that load kinetic energy was often insufficient to account for the measured radiative yields. It was assumed that the additional dissipation required to explain the yields was due to some anomalous resistivity, since the classical Ohmic dissipation was too slow a process to generate enough energy. Until now, no theory of this enhanced dissipation has been developed. It is important to have such a theory because recent long pulse experiments have shown that the additional energy coupled to the plasma can be factors of 3-4 times the kinetic energy. Given understanding and control of this phenomenon, this substantial energy could potentially be tapped by proper load design to increase K-shell yields.

Here is presented an analytical model describing this additional energy deposition based on the concept of macroscopic magnetohydrodynamic (MHD) turbulent pinch heating proposed by Rudakov and Sudan [Phys. Reports 283, 253 (1997)]. The pinch plasma is modeled as a foam-like medium saturated with toroidal "magnetic bubbles" produced by the development of surface  $m = 0$  Rayleigh-Taylor and MHD instabilities. As the bubbles converge to the pinch axis, their magnetic energy is converted to thermal energy of the plasma through  $pdV$  work. Explicit formulas for the average dissipation rate of this process and the corresponding contribution to load resistance are presented. The possibility of using this enhanced (relative to Ohmic heating) dissipation mechanism to power novel radiation sources and produce high K-shell yields is discussed.

(2) Gas puff Z-pinch implosions, with Ne:Ar and Kr:Ar mixtures, at the 7 MA current level with approximately uniform and annular gas injection profiles have shown significant increases in x-ray power, reduction in pinch diameters in some cases, and increase in argon K-shell radiated yields with the uniform fill loads. Spectral analyses show that the uniform fill loads produce higher density, higher temperature pinches, in which more of the initial mass participates in K-shell x-ray emission. One-dimensional radiation-MHD calculations indicate that the uniform fill profile implosions would be less efficient producers of K-shell emissions than the annular cases. However, comparisons of the calculations with the data reveals that the uniform fill implosions produced plasma conditions and associated emissions that were much closer to the 1D calculated parameters than the annular implosions. Time-resolved pinhole images confirm that the uniform fill implosions have more axial uniformity. Two-dimensional radiation-MHD calculations demonstrate that the initial conditions, snowplow stabilization, field penetration and axial mass flow all contribute to the improvement in implosion uniformity. The work presented in this section was a joint collaboration between code 6720 Branch members and C. Deeney, M. R. Douglas, R. B. Spielman, and T. J. Nash of Sandia National laboratories as well as N. F. Roderick of the University of New Mexico and P. T. Springer and K. L. Wong of Lawrence Livermore National Laboratory.

(3) Through experiments by the PRS community and theoretical and spectral analyses largely developed by this Branch, it has become apparent that understanding the physics that takes place in the core of the plasma upon stagnation of the Z-pinch is a key to improving K-shell yield efficiencies as well as going up in photon energy. To achieve the optimal plasma core conditions

for producing K-shell x rays in moderate atomic number Z pinches, a fast thermalization of kinetic energy is necessary. Generally there are two ways to accomplish this: either by fluid compression or through the more sudden and nonlinear process of shock wave generation and dissipation. In this section a closer examination of the development and structure of shock fronts as well as a critique of past methods of modeling shock fronts is presented. Recent analysis has shown that the historical artificial treatment of shocks that ascribes all the viscosity to the ions is erroneous. In fact, depending on the ionization state of the plasma, real viscosity can favor heating of the electrons. The process of studying this problem in highly ionizable plasmas was begun last year with the development of a new description of the electron pressure tensor in spherical and planar geometry. This year the work was extended to the cylindrically symmetric geometry of a Z pinch where it is needed in order to investigate the generation of steep gradient structures and rapid ionization processes in and near the core of the Z pinch: This investigation may have special relevance to the design of nested array or nested load experiments.

(4) In this section we evaluate the future performance on Decade Quad of the large radius argon loads that have been developed for Double Eagle and Saturn. These are evolutionary loads in that the knowledge attained from their usage on Double Eagle and Saturn will allow us to mitigate the risks associated with large radius implosions and to ultimately design loads that make Decade Quad a successful argon PRS machine. In particular, the double puff nozzle loads used in the Double Eagle and Saturn long pulse experiments are assessed in terms of their future performance on Decade Quad. As was the case for last years analysis of the 7 cm diameter uniform fill loads, this assessment is accomplished by projecting Decade Quad argon K-shell yields by scaling in energy from the experimental Saturn and Double Eagle yields. In accord with last years large radius experimental results, the yields achieved using the double puff nozzle project to nearly 40 kJ of K-shell emission on Decade Quad. Unfortunately, the projected Decade Quad yields based upon the experimental Saturn yields are about 25 kJ. A likely reason for this diminished projection, which was alluded to in last years Annual Report, is due to K-shell yield saturation in the low coupled-energy-per-ion regime. The results of this energy scaling analysis as well as a more complete description of the phenomenon of yield saturation and techniques for mitigating its effects are presented.

(5) Our Branch, L. I. Rudakov, and E. Waisman were commissioned to explore novel approaches for producing  $\sim 10$  keV x rays from PRS loads powered by long pulse drivers. The White Paper on this subject is presented.

Simulations performed by our Branch have identified one of the main problems of generating a hard spectra, even at 60 MA and 100 ns rise time. That is that the energy exchange between electrons and ions is slow, requiring thousands of electron-ion collisions. Under most conditions this results in the electron energy being lost through softer radiation from lower ionization states before the H- and He-like ionization states are achieved. The only way of minimizing these losses is to increase simultaneously the stagnated plasma density and its confinement time. Then opacity would help decrease radiative losses and there will be enough time for ionization to the K-shell. In this section, three recent advances are described that lead to increased density and confinement time at stagnation that could help solve the problem of generating substantial yields of  $\sim 10$  keV quanta using low cost pulse power. These advances are: 1) make use of the enhanced energy deposition in Z-pinch plasmas (as described in Sec. 1), 2) increase density by increasing the confinement current using a modification of the concept of current multiplication suggested by O. Zucker, and 3) increase the current rise rate using an "inductive switch", rather than a plasma opening switch POS. The advantage of the inductive switch over the POS is that the switching and load sections of the inductive switch are spatially separated, so that no plasma from the switching section reaches the imploding load.

# **I. Model of Enhanced Energy Deposition in a Z-Pinch Plasma**

## **I. Introduction**

In plasma radiation sources (PRS), Z-pinch loads are imploded to convert the magnetic energy supplied by the pulsed power driver into the kinetic energy of the load, which is then converted into plasma thermal energy at stagnation, and then, finally, into x-ray radiation.<sup>1</sup> One of the most important characteristics of PRS is the total energy coupled to the pinch and available to conversion into radiation. The early PRS experiments (e. g., see Refs. 2, 3) have discovered a remarkable fact: the total radiation yield was noticeably larger than the kinetic energy imparted to the load. In late 1970s, analysis of these and similar experiments and their one-dimensional (1-D) numerical simulation<sup>4</sup> led to the conclusion that the additional, or enhanced, dissipation is due to some anomalous resistivity, since the classical Ohmic dissipation was found too slow to generate enough energy. Since then, no theory of this enhanced dissipation, which plays a major role in supplying energy to the pinch, has been developed.

A new physical mechanism of enhanced energy dissipation was recently proposed by Rudakov and Sudan.<sup>5</sup> The enhanced energy dissipation was explained by convergence to the pinch axis and subsequent annihilation of toroidal magnetic flux tubes, “magnetic bubbles”, which results in a deposition of their magnetic energy into the plasma in the form of heating and macroscopic MHD turbulent motion. Independently, two-dimensional (2-D) numerical simulations of Z-pinch implosions (see Ref. 6 and references therein) have consistently reproduced, without invoking anomalous resistivity, a lot of experimental features that have not been predicted with lesser dimensional

approaches. These features include “a larger drive current in the load, more energy extracted from the pulsed power system, and thus the possibility of enhanced radiation yields.”<sup>6</sup> Since the enhanced dissipation as we describe it is essentially a 2-D  $r$ - $z$  MHD process, a fully accurate 2-D  $r$ - $z$  MHD modeling should reproduce it. We believe that 2-D Eulerian simulations of Ref. 6 to some extent do so. At the moment, it is not clear, however, whether the numerical resolution available for 2-D is sufficient to accurately describe all the relevant effects, including reconnection of current and formation of the closed current loops, the “magnetic bubbles”. This problem needs further study.

The enhanced energy deposition has thus been shown to be a hydrodynamic (although essentially non-1-D), rather than a kinetic effect. Still, more work is needed to fully understand and describe this mechanism. In particular, still no theory is available to estimate the rate of the enhanced deposition.

In the present paper, we develop a theoretical model that describes an enhanced energy deposition mechanism that is dissipative in nature. We present explicit formulas for the average enhanced dissipation rate and the corresponding contribution to the resistance of the load, which compare favorably to the experimental data and simulation results. These formulas permit incorporation into a 1-D radiation-MHD code. Finally, we discuss the possibility of using this dissipation mechanism to power novel PRS intended to produce high K-shell yields in the long current pulse regime.

The paper is structured as follows. In Section II, we present analytical estimates and experimental data showing that the enhanced energy dissipation is a major contributor into the pinch plasma energy balance. In Section III, our theoretical model is introduced, and analytical formulas for the enhanced dissipation rate and the

corresponding contribution to effective pinch resistance are derived. In Section IV, these formulas are compared to experimental data and numerical results and applied to a variety of Z-pinch issues, from modification of the Pease-Braginskii equilibrium conditions to generation of intense K-shell radiation in the long pulse regime. In Section V we conclude with a discussion.

## II. The background.

The “kinetic” or “mechanical” or “magnetic” energy  $E_k$  coupled to the pinch during the implosion can be estimated as work done by magnetic pressure:

$$E_k = \int \frac{B^2}{8\pi} \cdot 2\pi R l \cdot \left( -\frac{dR}{dt} \right) dt = \int_{R_f}^{R_i} \frac{I^2 l}{c^2 R} dR = a l \frac{I_m^2}{c^2} \ln \frac{R_i}{R_f} = \frac{a}{2} \Delta L (\text{nH}) I_m (\text{MA})^2 \text{ kJ}, \quad (1)$$

where  $l$  is the pinch length,  $R_i$  is the initial radius of the pinch,  $R_f$  is its final radius at stagnation,  $I_m$  is the peak current,  $\Delta L (\text{nH}) = 2 \cdot l (\text{cm}) \cdot \ln(R_f / R_i)$  is the change of the pinch inductance in the implosion,  $a$  is a dimensionless coefficient of order unity that accounts for the current pulse shape:  $a = 1$  for a constant current,  $a \approx 0.6$  for typical current pulses in multi-MA machines (for details, see Ref. 7).

When the pinch column assembles at the axis, it has already been severely distorted by the Rayleigh-Taylor instability during its acceleration phase. Then the pinch is no longer accelerated, but it still experiences the  $m = 0$  MHD sausage instability, whose growth rate is of order of  $1/\tau_A$ . Recall that  $\tau_A = R_f / v_A$  is the Alfvén time expressed via the Alfvén velocity

$$v_A = \frac{B}{(4\pi\rho)^{1/2}} = \frac{I_m}{c\mu^{1/2}} = 10^8 \cdot \frac{I_m (\text{MA})}{\mu (\mu\text{g/cm})^{1/2}} \text{ cm/s}, \quad (2)$$

where  $\mu$  is the line mass of the pinch. For most relevant experiments,  $R_f \sim 1 \text{ mm}$ ,  $v_A \sim (3-5) \cdot 10^7 \text{ cm/s}$ , so that  $\tau_A \sim 2-3 \text{ ns}$ . One might expect the instabilities to make the pinch disintegrate within the time  $\sim \tau_A$ , but this does not happen. Instead, the quasi-cylindrical pinch column stays near the axis for about  $(5-10) \cdot \tau_A$ . Referring to this period of time, it is sometimes said that the pinch is “cooking” near the axis, as observed on the soft x-ray images that include a significant fraction of the total Z-pinch emission. The big question is whether an appreciable amount of magnetic energy can be coupled to the pinch while it is “cooking”.

There is plenty of magnetic energy in the vacuum cavity surrounding the stagnated pinch: magnetic energy delivered to the load unit exceeds the Bennett thermal energy contained in the pinch plasma by a factor of  $\ln(R_w / R_f) \approx 3$  (where  $R_w$  is the radius of the current return can), and there is more of it in the inner magnetically insulated transmission lines. The “cooking” pinch, however, appears to have little chance to tap this energy. Since in the “cooking” phase  $dR/dt \approx 0$ , the magnetic pressure no longer performs the  $pdV$  work accelerating or compressing the pinch column as a whole. The only mechanism that can couple more magnetic energy into the pinch seems to be Ohmic heating, that is, diffusion of magnetic energy into the pinch. To estimate the role of Ohmic heating, we introduce the conventional parameters characterizing it. The rate of diffusion (magnetic diffusivity) is expressed via the plasma conductivity  $\sigma$  as  $\nu_m = c^2 / 4\pi\sigma [\text{cm}^2/\text{s}]$ . The characteristic velocity associated with this rate and the length scale  $R_f$  is



$$v_{Ohm} = \frac{v_m}{R_f}. \quad (3)$$

An important dimensionless parameter of the pinch, the magnetic Reynolds number  $Rm$ , is the ratio of the two characteristic velocities:

$$\begin{aligned} Rm &= \frac{v_A}{v_{Ohm}} = \frac{v_A R_f}{v_m} = \frac{4\pi\sigma v_A R_f}{c^2} \\ &= \frac{3(2\pi)^{1/2} m_u^{3/2} Z^{3/2} I_m^4 R_f}{2m_e^{1/2} e^2 c^6 \ln \Lambda \bar{Z} (1 + \bar{Z})^{3/2} \mu^2} = 1.3 \cdot 10^7 \frac{Z^{3/2} I_m^4 (\text{MA}) R_f (\text{mm})}{\ln \Lambda \bar{Z} (1 + \bar{Z})^{3/2} \mu^2 (\mu\text{g/cm})}. \end{aligned} \quad (4)$$

Here,  $\ln \Lambda$  is the Coulomb logarithm. In Eq. (4) the temperature that enters the classical resistivity is expressed via the pinch current using the Bennett relation,

$$T = \frac{I_m^2 m_i}{2c^2 (1 + \bar{Z}) \mu} \cong \frac{Z}{1 + \bar{Z}} \frac{I_m^2 m_u}{c^2 \mu} = 10.4 \frac{Z}{1 + \bar{Z}} \frac{I_m^2 (\text{MA})}{\mu (\mu\text{g/cm})} \text{ keV}, \quad (5)$$

where  $m_u$  is the atomic mass unit,  $\bar{Z}$  is the mass-averaged ion charge for the plasma whose atomic number is  $Z$ , and the atomic mass  $A \approx 2Z$  both for high- $Z$  elements and for deuterium. This way we tend to underestimate the magnetic Reynolds number, since the plasma temperature near the pinch boundary, where most of the current flows, might be higher than the mass-averaged Bennett temperature. Still, according to the estimate (4),  $Rm \gg 1$  (typically,  $Rm$  is of order of  $10^3$  or greater) for all situations of interest.

Since  $Rm \gg 1$ , the current flows in and heats the skin layer, whose depth is  $\delta = (v_m t)^{1/2}$ , much less than the pinch radius. The average current density in the skin layer is  $j = I_m / 2\pi R_f \delta$ . Then the Ohmic heating during the time interval  $t$  after stagnation could be estimated as

$$E_{Ohm} = \int_0^t 2\pi R_f l \frac{j^2}{\sigma} dt' = 4 \frac{I_m^2 l}{c^2} \frac{(v_m t)^{1/2}}{R_f} = 4 \frac{I_m^2 l}{c^2} \frac{(t / \tau_A)^{1/2}}{Rm^{1/2}}. \quad (6)$$

Substituting (4) into (6), we find that the Ohmic heating due to classical resistivity,  $E_{Ohm}$ , is much smaller than the  $\mathbf{J} \times \mathbf{B}$  work during the implosion,  $E_k$ , if the pinch confinement time is not too high:

$$\frac{t}{\tau_A} \ll \frac{Rm}{4}, \quad (7)$$

For typical conditions of the PRS experiments, the right-hand side of (7) is of order of  $10^2$ - $10^3$ , whereas the confinement time typically does not exceed  $10\tau_A$ . Since the stagnated Z-pinchs observed in experiments are distorted by instabilities, the “surface area” through which the magnetic energy could penetrate into the plasma could be much larger than  $2\pi Rl$ . This makes the contribution of the classical resistivity much higher than the above estimates would suggest, although still insufficient to account for all the difference between the work of magnetic pressure during the implosion phase,  $E_k$ , and the observed total x-ray yield,  $Y$ .

The above indicates that the energy coupled to the pinch seems to be reasonably estimated by (1). If the pinch load is an annular plasma shell, then during the run-in phase of the implosion its thermal pressure is much less than the magnetic pressure driving it, so that  $E_k$  is an estimate for the kinetic energy to be thermalized at stagnation. For a uniform fill load,  $E_k$  estimates the sum of kinetic and thermal energy delivered to the shock-driven plasma. The classical Ohmic heating during the “cooking” phase adds a relatively small (compared to  $E_k$ ) amount of energy to the plasma. Let us test this conclusion, substituting into (1) the typical parameters of PRS experiments on GIT-4 in Russia,<sup>8</sup> Double Eagle,<sup>9</sup> Saturn in short<sup>10</sup> and long pulse regime,<sup>11,12</sup> and the Z generator.<sup>13</sup> The results, shown in Table 1, are consistent with the implosion kinetic

energies estimated for these cases using the 0-D slug/circuit model. The experiments, however, consistently demonstrate that the pinches dissipate much more energy than could be imparted to the pinch plasma during the run-in phase of the implosion, in the form of kinetic energy or otherwise. As for the above examples, the total measured radiation yields in all cases are substantially larger than the above estimates, see Table 1.

The dependence (1) of  $E_k$  on the compression ratio is weak. Therefore, the discrepancy between the estimated energies and observed yields cannot be explained by simply assuming a higher than 20-fold radial plasma compression averaged over the pinch length. To obtain the above yields with the aid of (1), the corresponding radial compression ratios must be taken way above those consistent with experimental data: from 100 for Double Eagle and Z to 250 for GIT-4 and more than 1000 for Saturn.

Since 100- to 1000-fold compressions are obviously unrealistic, one concludes that some additional mechanism of energy dissipation in the "cooking" regime must be at work. This mechanism adds a major contribution, of order of 50%, and sometimes much more, to the plasma energy balance. Its effect is not limited to a particular device or experimental conditions; it is consistently observed in numerous PRS experiments, from those performed in the 1970-80s on Blackjack 3 and PITHON,<sup>2,3</sup> to more recent experiments on Double Eagle, Saturn and Z. In other words, this effect is pervasive. How do we explain it?

The early analysis<sup>4</sup> determined that magnetic energy seemed to penetrate into the plasma column much faster than classical resistive diffusion would permit, which seemed to indicate enhanced, that is, anomalous resistivity. Simulations of Ref. 4 have shown, however, that this must have been some non-conventional kind of anomalous resistivity,

whose manifestation did not correlate with conditions favorable for either two-stream or ion-sound instabilities. No theory providing a satisfactory explanation of the enhanced dissipation via any kind of anomalous transport, like resistivity or micro-turbulence has been suggested ever since. Recent analysis<sup>5</sup> and simulations<sup>6</sup> have demonstrated that invoking anomalous resistivity is not really necessary. In the “cooking” phase, after stagnation, most of the energy might couple to the pinch through the  $pdV$  work associated with the 2-D plasma flow in the unstable plasma column. Numerical modeling of this effect involves detailed description of individual bubbles and spikes formed in the pinch plasma, therefore being very demanding on computer power. Additionally, evaluating the contribution of this particular dissipation mechanism to the total plasma energy balance in the 2-D simulations is not straightforward. Other contributing factors include, for instance, effective lowering of the pinch inductance due to the 2-D structure that allows for higher current level to be sustained for a longer period of time than is possible for a 0-D model that achieves the same effective compression (see Fig. 14 of Ref. 6), or increased Ohmic heating along the 2-D current path that is many times the length  $l$  of the diode.

Our goal is to develop the approach to this effect suggested in Ref. 5. We are interested in describing the enhanced energy dissipation in a Z-pinch column, whose parameters are averaged over time and axial distance (and thereby, over individual bubbles and spikes). Thus we seek a quasi-1-D description, that must account for the essential features of the 2-D flow that are responsible for the enhanced energy dissipation. This description can be used to produce explicit formulas for the dissipation

rate, and further advanced to the point of being incorporated into a 1-D radiative-MHD code.

### III. Enhanced dissipation due to magnetic bubbles

#### A. The concept

Consider a magnetic bubble that emerges as a neck at the surface of the pinch as a result of nonlinear development of the  $m = 0$  mode of the MHD and/or RT instability [Fig. 1(a)]. Following Ref. 5, suppose that the plasma closes behind it, thus forming a doughnut-shaped, toroidal bubble, completely entrained by its own current loop, as shown in Fig. 1(b). Here, we assume full azimuthal symmetry, as in  $r$ - $z$  numerical simulations, and describe only toroidal bubbles that carry azimuthal magnetic field lines. This is the simplest physical picture sufficient to describe the effect we are interested in, the enhanced dissipation. Motion of the bubbles through the plasma is well ordered, being determined by the plasma parameters. The concept of a foam-like plasma saturated with toroidal bubbles is self-consistent. If two or more bubbles collide (this process is not included in the version of the bubble model described below), due to simple geometry of the problem, they would coalesce, without any dissipation, into one bubble, conserving volume, cross-sectional area, magnetic energy and magnetic flux. Let us now describe the motion of a bubble.

The bubble carries magnetic flux and magnetic energy but contains no mass. Assuming the smaller radius of the torus,  $R_b$ , is much less than the other characteristic lengths, we can express the parameters of the bubble via the fluid variables of the plasma

surrounding it. In particular, the azimuthal magnetic field inside the bubble,  $B_b$ , is determined by the condition of total pressure equilibrium at the bubble boundary

$$\frac{B_b^2}{8\pi} = \frac{B^2}{8\pi} + p. \quad (8)$$

Neglecting diffusive losses of magnetic flux from the bubble, we can relate  $B_b$  and  $R_b$ :

$$B_b R_b^2 = \frac{2I}{Rc} \bigg|_{t=t_b} R_{b0}^2 = \text{const}, \quad (9)$$

where  $t = t_b$  is the instant when the given bubble emerged at the surface.

The radial force per unit volume on the bubble can be expressed as

$$F_b = -\rho g - \frac{2p}{r}, \quad (10)$$

where  $g = -a$  is the effective gravity experienced by the accelerated plasma volume.

When the plasma is accelerated inward,  $a < 0$ , then  $g > 0$ , so that the buoyancy force  $-\rho g$  is negative. The bubble, rising in the gravitational field, is driven to the axis. This contribution to  $F_b$  is associated with the RT instability. The remaining term in (10) is due to the non-gradient term  $-B^2 / 4\pi r$  (curvature stress) in the equation of motion for the Z-pinch geometry, where the radial force per unit volume equals  $-\nabla(B^2 / 8\pi + p) - B^2 / 4\pi r$ . The total pressure per unit volume is the same in the bubble and in the plasma around it, whereas the curvature stress in the bubble is larger by  $-2p / r$ , see (8). This contribution to  $F_b$ , which is, of course, associated with the MHD sausage instability, always drives the bubble to the axis.

Since the bubble has no inertia, the radial force has to be balanced by the drag force,  $C\rho R_b v_r^2$  per unit length of the bubble, where  $C$  is a dimensionless drag coefficient

(below we assume  $C = 1$ , the value appropriate for a straight rigid cylinder at not-too-high Reynolds numbers<sup>14</sup>), and  $v_r$  is the velocity of the bubble relative to the plasma. Then we obtain:

$$v_r = - \left( \frac{\pi R_b}{r} \right)^{1/2} \left| g r + \frac{2p}{\rho} \right|^{1/2} \operatorname{sgn} \left( g r + \frac{2p}{\rho} \right). \quad (11)$$

Here,  $R_b$  can be expressed with the aid of (8)-(9). The  $\operatorname{sgn}$  function emerges when the square root is extracted, to ensure that the bubble moves in the same direction as the radial force (10) drives it.

When the bubble is driven to the pinch axis, the magnetic flux it carries is conserved, but its magnetic energy,  $E_b$ , is not. Rather, it decreases as

$$\frac{E_b(t)}{E_{b0}} = \frac{r(t)c [8\pi p(r(t),t) + B(r(t),t)^2]^{1/2}}{2I(t_b)}, \quad (12)$$

mainly because the volume of the bubble diminishes proportionally to its larger radius,  $r = r(t)$ . The energy is dissipated in the pinch plasma, both through the  $pdV$  work (displacing the plasma) and through the work of the drag force. The latter includes both dissipation in a boundary layer and generation of sonic waves due to motion of an object (bubble) through the plasma at subsonic velocity. As the bubble reaches the axis,  $r(t) \rightarrow 0$  [Fig. 1(c)], all of the energy that it initially carried has been dissipated.

In other words, once the magnetic bubble pinches off and is completely entrained by its own current loop, becoming a fully formed flux tube [Fig. 1(b)], it could be visualized as a contracting rubber band. As it moves to the pinch axis, the magnetic flux it carries is conserved (the band is still there), but the magnetic energy (tensile energy of the rubber) decreases, being converted to the energy of the plasma through the  $pdV$

(displacement) and the drag force work. Release of this magnetic energy accounts for a major contribution to the energy balance of the pinch plasma. This is essentially the mechanism of enhanced dissipation. The presence of the bubbles effectively increases the surface of the plasma, where it could be pushed (and thereby heated) by the magnetic field, hence increasing the dissipation rate. One can even recognize some similarity of the “cooking” Z-pinch regime with the conventional cooking process. The energy balance of the boiling water is similarly affected by the effective increase of its surface available for evaporation due to formation of the bubbles.

The bubbles are driven inward by a combination of magnetic buoyancy and curvature stress. (Similarly, the coronal magnetic activity generates the “magnetic flux ropes,” which then rise in the solar gravitational field, as discovered long ago by Parker.<sup>15)</sup> It should be emphasized that the enhanced energy dissipation is due to the inward motion of “empty” bubbles (the plasma density inside the bubbles must be much less than outside) rather than to the interchange of the neighboring flux tubes containing both plasma and magnetic flux. The latter process only redistributes the energy within the plasma column and cannot couple additional magnetic energy from the vacuum to the pinch. Not surprisingly, an equilibrium Z-pinch with a sharp boundary is always unstable with respect to the  $m = 0$  perturbations (in other words, it is always ready to absorb more magnetic bubbles), whereas a diffuse equilibrium Z-pinch could be stable with respect to the  $m = 0$  interchange of the neighboring flux tubes, provided that the Kadomtsev stability criterion, Eq. (4.3) of Ref. 16, is satisfied.



## B. The model equations

The pinch plasma is modeled as a foam-like medium saturated with toroidal "magnetic bubbles". Let  $\rho$  be the plasma density outside the bubbles, and  $\alpha$  the volume fraction occupied by the bubbles ( $0 \leq \alpha < 1$ ). Consider a "bubble fluid," whose density is  $-\rho$ , superimposed on the plasma, so that the total density is zero in the volume fraction  $\alpha$ , which makes the average mass density  $\bar{\rho} = (1 - \alpha)\rho$ . The plasma momentum density is  $\rho v_p$ , the momentum density of the "bubble fluid" is  $-\alpha\rho v_b$ , the total momentum density thus being  $\bar{P} = \rho(v_p - \alpha v_b)$ . Let us introduce  $V = \bar{P} / \bar{\rho} = (v_p - \alpha v_b) / (1 - \alpha)$  as the center-of-mass velocity of the fluid containing the bubbles. Then velocities of the plasma and the bubbles,  $v_p$  and  $v_b$ , are expressed as

$$v_p = V + \frac{\alpha v_r}{1 - \alpha}, \quad v_b = V + \frac{v_r}{1 - \alpha}, \quad (13)$$

where  $v_r = v_b - v_p$  is the velocity of the bubbles relative to the plasma. Of course, since the bubbles contain no mass, the center-of-mass position is that of the plasma. However, when a bubble whose volume is  $\mathcal{V}_b$  moves from point 1 to point 2, the corresponding amount of mass,  $\rho \mathcal{V}_b$ , has to be moved from point 2 to point 1, which also affects the center-of-mass position. Separating the bubble and the plasma motions, we specifically exclude the contribution to the plasma velocity due to the bubble motion, assuming that it is concentrated in the vicinity of a bubble, whereas  $v_p$  is defined as the average macroscopic plasma velocity far from the bubbles. Defining  $d/dt = \partial/\partial t + V(\partial/\partial r)$ , we note that in the expression (11) for  $v_r$ , we have:  $g = -dV/dt$ .

The mass conservation equation therefore is conventional:

$$\frac{\partial}{\partial t}(1-\alpha)\rho + \frac{1}{r}\frac{\partial}{\partial r}r(1-\alpha)\rho V = 0, \quad (14)$$

because  $\bar{\rho} = (1-\alpha)\rho$  is the true average density in the volume that contains bubbles.

The induction equation for the bubbles is

$$\frac{\partial}{\partial t}\alpha B_b + \frac{\partial}{\partial r}\alpha B_b \left( V + \frac{v_r}{1-\alpha} \right) = 0, \quad (15)$$

where  $B_b$  is given by (8) and resistive losses of magnetic flux from the bubbles are

neglected. The inductive equation for the plasma includes finite resistivity  $\sigma$ :

$$\frac{\partial}{\partial t}(1-\alpha)B + \frac{\partial}{\partial r}(1-\alpha)BV - \frac{\partial}{\partial r}(1-\alpha)\frac{c^2}{4\pi\sigma r}\frac{\partial}{\partial r}rB = 0, \quad (16)$$

The equation of motion is

$$(1-\alpha)\rho \frac{dV}{dt} + \frac{\partial p}{\partial r} + \frac{B}{4\pi r}\frac{\partial}{\partial r}(rB) + \frac{2\alpha p}{r} = 0, \quad (17)$$

where the additional term in the left-hand side of (17) accounts for the extra curvature stress experienced by the bubbles, as discussed in Section II.A.

The electron energy equation is

$$\begin{aligned} \frac{d}{dt}(1-\alpha)E_{Te} + \frac{(1-\alpha)(E_{Te} + p_e)}{r}\frac{\partial}{\partial r}rV - \frac{\partial}{\partial r}(1-\alpha)\kappa_e\frac{\partial T_e}{\partial r} \\ = p_e\frac{d\alpha}{dt} + (1-\alpha)\frac{j^2}{\sigma} - (1-\alpha)Q_\Delta - Q_{rad}, \end{aligned} \quad (18)$$

where  $j = (c/4\pi r)(\partial/\partial r)(rB)$  is the current density in the plasma,  $\kappa_e$  is the electron thermal conductivity,  $Q_\Delta = (3m_e/m_i)(n_e/\tau_e)(T_e - T_i)$  is the electron-ion energy exchange rate,  $Q_{rad}$  accounts for energy losses or heating due to radiation. The ion energy equation is

$$\begin{aligned} \frac{d}{dt}(1-\alpha)E_{Ti} + \frac{(1-\alpha)(E_{Ti} + p_i)}{r} \frac{\partial}{\partial r} rV \\ = p_i \frac{d\alpha}{dt} - \alpha v_r \left( \rho g + \frac{2p}{r} \right) + (1-\alpha)Q_\Delta. \end{aligned} \quad (19)$$

Summation of Eqs (18), (19) yields the plasma energy equation:

$$\begin{aligned} \frac{d}{dt}(1-\alpha)E_T + \frac{(1-\alpha)(E_T + p)}{r} \frac{\partial}{\partial r} rV - \frac{1}{r} \frac{\partial}{\partial r} r(1-\alpha)\kappa_e \frac{\partial T}{\partial r} \\ = p \frac{d\alpha}{dt} - \alpha v_r \left( \rho g + \frac{2p}{r} \right) + (1-\alpha) \frac{j^2}{\sigma} - Q_{rad}, \end{aligned} \quad (20)$$

where  $E_T = E_{Te} + E_{Ti}$ ,  $p = p_e + p_i$ . In the right-hand side of Eq. (20) we have two extra terms that describe enhanced energy dissipation. The first term describes the effect of displacing the plasma by changing the volume fraction occupied by the bubbles – in other words, this term represents plasma heating due to the  $pdV$  work done by the bubbles converging to the axis. This work is transformed into thermal energy of electrons and ions at the rates proportional to their respective pressures. The second term is the energy release due to the drag force between the plasma and the bubbles moving through it. Equation (11) demonstrates that its contribution is always positive, as it should be. Most of this energy is dissipated in the ion fluid; its fraction delivered to the electron fluid is estimated as  $Z \cdot (m_e T_e / m_i T_i)^{1/2}$ , which is much less than unity for all cases of interest.

The system of Eqs. (15)-(20) satisfies the basic conservation laws. Conservation of mass in a cylinder whose radius  $R(t)$  satisfies  $dR/dt = V(R(t), t)$ , is easily derived from Eq. (15). For a steady-state equilibrium, we derive from (17) the Bennett relation (5) without any modification.

Magnetic flux contained in the bubbles per unit length of the pinch varies with time according to

$$\frac{d\Phi_b}{dt} = \frac{d}{dt} \int_0^R \alpha B_b dr = \left. \frac{\alpha B_b v_r}{1-\alpha} \right|_{r=R(t)} = - \left. \frac{\alpha v_r}{1-\alpha} \right|_{r=R(t)} \frac{2I}{Rc}, \quad (21)$$

since at the outer boundary of the plasma  $B_b = 2I/Rc$ . If the pinch is accelerated inward ( $g > 0$ ) or steady ( $g = 0$ ), then  $v_r < 0$ , see Eq. (11), so the pinch absorbs magnetic flux from the vacuum due to penetration of the magnetic bubbles.

From the induction equation (16) we find the time variation of the magnetic flux in the plasma,  $\Phi_p$ :

$$\frac{d\Phi_p}{dt} = \frac{d}{dt} \int_0^R (1-\alpha) B dr = (1-\alpha) \frac{c^2}{4\pi\sigma R} \frac{\partial}{\partial r} (rB) \Big|_{r=R} - cI\mathcal{R}, \quad (22)$$

where the averaged resistance  $\mathcal{R}$  per unit length of the pinch column is defined as

$$\mathcal{R} = \lim_{r \rightarrow 0} \frac{\pi R^2 j(r)}{I} \frac{[1-\alpha(r)]}{\pi R^2 \sigma(r)}. \quad (23)$$

Here, we suppose the pinch column to extend to the axis. The right-hand side of Eq. (23)

in effect determines the rate coefficient for *magnetic flux dissipation at the pinch axis*.

Note that the electric field near the pinch axis determines the “averaged” value of resistance (23), see Eqs. (2), (3) of Ref. 17.

Multiplying Eqs. (15), (16), (17) by  $B_b$ ,  $B$ , and  $V$ , respectively, and summing the results with (20), we derive the energy conservation equation in the form

$$\frac{\partial}{\partial t} E_{total} + \frac{1}{r} \frac{\partial}{\partial r} r q_{total} = -Q_{rad}. \quad (24)$$

Here, the total energy density is given by

$$E_{total} = (1-\alpha)E_T + \frac{1}{2}(1-\alpha)\rho V^2 + \frac{B^2}{8\pi} + \alpha p, \quad (25)$$

the last term being due to the excess of magnetic energy in the bubbles, as expressed by (8). The total energy flux is

$$q_{total} = (1-\alpha)E_T V + (1+\alpha)pV + \frac{1}{2}\rho(1-\alpha)V^3 + \frac{B^2 V}{4\pi} + \frac{2\alpha v_r}{1-\alpha} \left( \frac{B^2}{8\pi} + p \right) - (1-\alpha)\kappa_e \frac{\partial T_e}{\partial r} - (1-\alpha) \frac{c^2 B}{16\pi^2 \sigma r} \frac{\partial}{\partial r} rB. \quad (26)$$

Let us write down the energy conservation equation for the whole system pinch + circuit.

Variation of magnetic flux in vacuum outside of the pinch could be expressed as

$$\frac{d\Phi_{vac}}{dt} = \frac{d}{dt} \int_R^{R_w} \frac{2I}{rc} dr = \frac{d}{dt} \frac{2I}{c} \ln \frac{R_w}{R} = -\frac{2I\dot{R}}{c^2 R} + \frac{2\dot{I}}{c} \ln \frac{R_w}{R}, \quad (27)$$

where  $R_w$  is the radius of return current can. Variation of magnetic energy in the vacuum is

$$\frac{d}{dt} E_{vac} = \frac{d}{dt} 2\pi \int_R^{R_w} \frac{1}{8\pi} \left( \frac{2I}{rc} \right)^2 r dr = \frac{d}{dt} \frac{I^2}{c^2} \ln \frac{R_w}{R} = -\frac{I^2 \dot{R}}{c^2 R} + \frac{2I\dot{I}}{c^2} \ln \frac{R_w}{R}. \quad (28)$$

Integrating (24) with the aid of (21)-(23), we obtain:

$$\begin{aligned} \frac{d}{dt} E_{pinch} &= \frac{d}{dt} 2\pi \int_0^R E_{total} r dr \\ &= - \left[ \left( V + \frac{2\alpha v_r}{1-\alpha} \right) \frac{B^2}{8\pi} - (1-\alpha)\kappa_e \frac{\partial T_e}{\partial r} - (1-\alpha) \frac{c^2 B}{16\pi^2 \sigma r} \frac{\partial}{\partial r} rB \right]_{r \rightarrow R-0} \cdot 2\pi R - \dot{E}_{rad} \quad (29) \\ &= -\frac{I^2 \dot{R}}{c^2 R} + \frac{I}{c} \frac{d\Phi_b}{dt} + \frac{I}{c} \frac{d\Phi_p}{dt} + I^2 \mathcal{R} - \dot{E}_{rad}, \end{aligned}$$

where  $\dot{E}_{rad} = 2\pi \int Q_{rad} r dr$ , and the absence of conductive heat flux through the outer pinch boundary has been assumed. Then the energy conservation relation is

$$\frac{d}{dt} (E_{vac} + E_{pinch}) + \dot{E}_{rad} = IU, \quad (30)$$

where

$$U = \frac{1}{c} \left( \frac{d\Phi_{vac}}{dt} + \frac{d\Phi_b}{dt} + \frac{d\Phi_p}{dt} \right) + I\mathcal{R} \quad (31)$$

is the voltage applied to the load unit, as it should be.

Equation (11), as well as most other equations of our model, is formally justified only in the limit  $R_b / r \rightarrow 0$ . It should be noted, however, that we are constructing a model rather than developing a full theory of MHD turbulence in a Z-pinch, which is an infinitely more complicated task. Our main concern is a correct bookkeeping of energy and magnetic flux in a not-too-complicated quasi 1-D description. We have shown above that model equations satisfy the basic conservation laws independently of the smallness of the parameter  $R_b / r$ , which, for this type of a model, appears to be a sufficient justification even slightly beyond its formal limits of applicability. Of course, dissipation of magnetic flux near the axis, where  $R_b / r$  tends to infinity, requires a separate consideration. Note, however, that the bubbles reaching the axis have already converted most of their initial energy to the plasma, see Eq. (12).

From (21), (30), (31) we find the energy source for the enhanced dissipation:

$$P_{enh} = \frac{Il}{c} \frac{d\Phi_b}{dt} = -\frac{2\alpha v_r}{1-\alpha} \bigg|_{r=R(t)} \frac{I^2 l}{c^2 R} = \frac{2\alpha}{1-\alpha} \left( \frac{\pi R_b}{R} \right)^{1/2} \left( gR + \frac{2p}{\rho} \right)^{1/2} \bigg|_{r=R(t)} \frac{I^2 l}{c^2 R}. \quad (32)$$

For an accelerated plasma shell,  $g \equiv I^2 / \mu R c^2$ ; for a pinch column in a Bennett equilibrium (5),  $2p / \rho \equiv I^2 / \mu R c^2$ . Replacing the expression in parentheses in (32) by  $I^2 / \mu R c^2$  for all cases, we transform (32) to an expression equivalent to Eq. (13) of Ref. 5:

$$P_{enh} = \zeta \frac{I^3 l}{\mu^{1/2} c^3 R}, \quad \text{where } \zeta = \left[ \frac{2\alpha}{1-\alpha} \bigg|_{r=R(t)} \left( \frac{\pi R_b}{R} \right)^{1/2} \right]. \quad (33)$$

The expression for  $\zeta$  represents the boundary condition at  $r = R(t)$  that has to be externally supplemented to the model. The value of  $\alpha$  at the pinch boundary means the effective fraction of the pinch length occupied by the incoming bubbles. It cannot be equal to unity (otherwise we return to a purely 1-D situation), but should not be much less than unity, either, since the bubble penetration is an instability-driven process over all the pinch length. The same could be said about the ratio  $R_b / R$  at the pinch surface: the bubbles whose radii are too small move slowly and are absorbed by larger bubbles. The dimensionless constant  $\zeta$  must be expressed via the macroscopic pinch characteristics, which are, in the limit  $Rm \gg 1$ ,  $I$ ,  $l$ ,  $R$ , and  $\mu$ , and fundamental constants. Since no meaningful dimensionless combination could be constructed of these (the dimensionless ratio  $I / I_A$ , where  $I_A = m_e c^3 / e = 17 \text{ kA}$  is the Alfvén current, is hardly relevant here), we have to assume this coefficient to be a constant. Physically, this assumption is equivalent to a hypothesis that the processes responsible for enhanced dissipation develop in a similar way in all Z-pinchs with  $Rm \gg 1$ . This hypothesis is consistent with the idea that after stagnation the  $m = 0$  instability is highly active and yet does not disrupt or destroy the pinch column. The late nonlinear stage of most hydro instabilities is characterized by some universal, self-similar laws of asymptotic behavior, loss of memory about the details of initial conditions (for classical RT and Richtmyer-Meshkov instabilities, cf. Ref. 18). In our case, the early- or intermediate-time perturbation growth, which is certainly affected by the gas-puff irregularities, or the wire initiation process, the number of wires and the width of the inter-wire gaps, the (still not fully understood) stabilization mechanisms in the nested wire array loads,<sup>19,13</sup> is

supposed to determine the final pinch radius  $R_f$  at stagnation (for a more initially uniform or otherwise better stabilized load,  $R_f$  would be less), which is maintained long after the memory of these details is lost. Of course, this is a hypothesis (not yet a theory!) which should be tested both in experiments and in simulation. Reasonable choice of the constant  $\zeta$  involves a certain degree of arbitrariness. For instance, combinations  $\alpha = 1/5$  to  $1/4$  and  $R_b / R = 1/4$  yields the value of  $\zeta$  between 0.44 and 0.59. In what follows, we will postulate  $\zeta = 1/2$ , in much the same way as the dimensionless coefficient  $1/16$  has been postulated in the expression for Bohm diffusion.<sup>20</sup> Then we come to the final form

$$P_{enh} = \frac{I^3 l}{2\mu^{1/2} c^3 R} = \frac{1}{2} \frac{I^3 (\text{MA}) l (\text{cm})}{\mu^{1/2} (\mu\text{g/cm}) R (\text{mm})} \text{ TW}, \quad (34)$$

which corresponds to effective additional non-linear resistance

$$\mathcal{R}_{enh} = \frac{Il}{2\mu^{1/2} c^3 R} = \frac{I (\text{MA}) l (\text{cm})}{2\mu^{1/2} (\mu\text{g/cm}) R (\text{mm})} \text{ Ohm}. \quad (35)$$

To clarify the physical meaning of these expressions, let us compare them with those describing conventional mechanisms of energy coupling. Note that we can re-write Eq. (34) as

$$P_{enh} = \frac{B^2}{8\pi} \cdot \frac{v_A}{2} \cdot 2\pi R l, \quad (36)$$

which simply says that magnetic energy, whose density at the pinch boundary equals  $B^2 / 8\pi = I^2 / 2\pi c^2 R^2$ , is carried by the bubbles into the pinch volume through its surface area  $2\pi R l$ , at the characteristic speed which is of order of, and slightly less than, the



Alfvén velocity  $v_A$ . Similarly, the power that goes into the acceleration of the plasma shell could be presented as

$$P_{kin} = \frac{B^2}{8\pi} \cdot \left( -\frac{dR}{dt} \right) \cdot 2\pi R l, \quad (37)$$

and the Ohmic heating power is

$$P_{Ohm} = \frac{B^2}{8\pi} \cdot \frac{v_m}{\delta} \cdot 2\pi R l. \quad (38)$$

From (1), we find that the peak velocity of the shell is  $v_A \sqrt{2a \ln(R_i / R_f)} \approx 2v_A$ ,

that is, somewhat higher than the velocity  $v_A / 2$  characteristic of the enhanced dissipation. Therefore the enhanced dissipation contribution is relatively small during the run-in phase. Near stagnation, when the radial velocity  $\dot{R}$  drops,  $P_{enh}$  starts dominating over  $P_{kin}$ . Comparing Ohmic and enhanced dissipation power, we find:

$$\frac{P_{enh}}{P_{Ohm}} = \frac{v_A \delta}{2v_m} \equiv \left( \frac{Rm}{4} \cdot \frac{t}{\tau_A} \right)^{1/2} \gg 1 \text{ at } t \sim t_A, \quad (39)$$

see (4). We see that the enhanced dissipation dominates at stagnation, in the “cooking” regime, since the velocity  $v_m / \delta$  characteristic of the magnetic diffusion is much less than  $v_A$ . Note that the  $P_{enh}$  is the energy delivered to the plasma column per unit time in the form of magnetic bubbles. Actual dissipation of this energy, its conversion into the thermal energy of the plasma, occurs with a delay of order of  $\tau_A$ , as the bubbles lose their magnetic energy while moving to the axis.

The next step in advancing the model of a foam-like Z-pinch plasma described by Eqs. (14)-(20), the enhanced power source (34) and the corresponding non-linear resistance (35), is to develop a 1-D radiative-MHD code to solve these equations coupled

to the appropriate equations that describe ionization dynamics and radiation generation and transport. These also have to be appropriately modified for a foam-like plasma, to take into account, for instance, that the actual plasma density,  $\rho$ , is higher outside of the bubbles than  $\rho(1 - \alpha)$ , the volume-averaged value at this point, which affects both radiation emission rate and opacity. This work is now under way, and results will be reported separately. In what follows, we analyze whether the available experimental data and simulation results support the main assumptions on which this model is based.

#### IV. Implications of the model

##### A. Enhanced dissipation in experiments and 2-D simulations

To compare the power scaling given by (34), we show in Fig. 2 the peak total radiation powers observed in experiments on Saturn<sup>10-12</sup> and Z<sup>13</sup> versus the quantity  $I_m^3 l / 2c^3 \mu^{1/2} R_f$ . The correlation between the two variables appears to be quite impressive. It helps to demonstrate the dual role of the RT and MHD instabilities. On the one hand, the instability mitigation techniques, like the use of nested wire arrays<sup>19,13</sup> help producing tighter pinches, thus increasing the enhanced dissipation power at stagnation, which is inversely proportional to  $R_f$ . Figure 2 demonstrates that, all the other parameters being equal, the peak radiation power scales as  $1/R_f$ . On the other hand, the enhanced energy deposition is driven precisely by the development of the same instabilities. We come to the following important conclusion: Effective PRS operation (in contrast, e. g., with laser fusion<sup>21</sup>) requires achieving an optimal trade-off between mitigation of instability and employing the instability-driven energy deposition, rather than a complete suppression of the instabilities.

The combination  $I_m^3 l / 2c^3 \mu^{1/2} R_f$  should be regarded as a scaling parameter rather than an estimate for the enhanced dissipation power at any given instant. Indeed, the current decreases due to increased inductance during the implosion, so that the pinch current is not equal to the peak current amplitude,  $I_m$ , when  $R = R_f$ . We can compare (34) directly with the powers observed in recent experiments and obtained in the simulations. Consider, for instance, the Z26 shot simulated in Ref. 6. According to this simulation, the peak power delivered to the pinch by the  $\mathbf{J} \times \mathbf{B}$  forces is about 80 TW, whereas the peak power delivered to the pinch in the form of kinetic energy,  $dE_{kin} / dt$ , is about 35 TW. The remainder, mostly  $p dV$ -generated power of 35 to 45 TW, could be accounted for, if we substitute into (34)  $\mu = 2 \text{ mg/cm}$  and  $R_f = 0.75 \text{ mm}$ , the observed value. Then  $P_{enh} = 35 \text{ to } 45 \text{ TW}$  if the current is between 10.5 and 11.5 MA, which is a fair estimate of the Z current near stagnation. Taking the pinch confinement time  $\tau$  for Z26 equal to the width of the radiation pulse,<sup>6</sup>  $\tau_{FWHM} = 7.5 \text{ ns}$ , one estimates the energy coupled to the pinch via the enhanced dissipation mechanism as  $E_{enh} = P_{enh} \tau_{FWHM} \approx 300 \text{ kJ}$ . Subtracting this value from the difference between the total yield,  $Y = 1800 \text{ kJ}$ , and the above estimate of the energy coupled to the pinch during the implosion/compression phase,  $E_k = 1250 \text{ kJ}$ , we find the remainder, 250 kJ, to be very close to contribution of the Ohmic heating obtained in the 2-D simulation.<sup>6</sup> We can conclude that for the short-pulse Z implosions, contribution of the enhanced dissipation to the total yield is important, although not dominant.

In another example, we can test the scaling of  $P_{enh}$  with the pinch length,  $l$ . All other parameters being constant,  $P_{enh}$  is simply proportional to  $l$ . In a recent experiment<sup>22</sup>

the length of a Z load was decreased by a factor of 2, from 2 cm to 1 cm. According to the estimates of Ref. 22, decreased inductance of the load unit resulted in increasing the peak current  $I_m$  by a factor somewhere between 1.15 and 1.34 (the latter number corresponds to estimated increase of current at stagnation). This would decrease the kinetic energy estimated from Eq. (1) by a factor from  $(1/2) \times 1.15^2$  to  $(1/2) \times 1.34^2 = 0.66$  to 0.9. The observed total x-ray yield did not decrease at all. Since the line mass of the shortened Z-pinch load has been increased by 30%, the combined effect of mass and current variations on the value of  $P_{enh}$  results in the factor of  $(1/2) \times 1.34^3 / \sqrt{1.3} = 1.06$ , which means that the enhanced dissipation power does not change at all. This is consistent with the experiment<sup>22</sup> that demonstrated no change in the peak radiation power emitted by the shortened load. The small decrease in  $E_k$  in this shorter length experiment may also have been compensated by an additional contribution from enhanced dissipation as a result of increased confinement time.

In the GIT-4 tungsten experiments at  $\mu = 370 \text{ } \mu\text{g/cm}$  [8], substituting the observed value of  $R_f = 0.42 \text{ mm}$  into (2) and multiplying the result by the observed confinement time, 30 ns, we obtain the enhanced energy deposition 25 kJ, quite close to the difference between  $Y$  and  $E_k$ , see Table 1.

In Saturn short-pulse experiments with tungsten wire arrays,<sup>10</sup> the total radiated energy exceeded the 0-D estimate of kinetic energy by about 300 kJ, that is, by a factor of ~3. The current amplitude was varied in the range 6.4 to 6.6 MA, line mass between 450 and 614  $\mu\text{g/cm}$ , pinch radius at stagnation from 0.45 to 0.8 mm, and the pinch confinement time can be estimated from the width of the radiation pulse as about 13 ns.

For these parameters, Eq. (34) yields  $P_{enh}$  in the range between 15 and 27 TW, that is, around 20 TW. The total energy coupled to the pinch via the enhanced dissipation mechanism is therefore estimated as  $\sim 20 \text{ TW} \times 13 \text{ ns} = 260 \text{ kJ}$ , quite close to the experimental value.

In the long-pulse Saturn experiments with tungsten wire arrays,<sup>11</sup> the ratio of observed radiated yield  $Y$  to the 0-D kinetic energy  $E_k$  was 3.5. Some results of these experiments are summarized in Table 2. For all shots, the pinch length was 2 cm. The 0-D kinetic energy  $E_k$  was found for all shots using the Saturn circuit model rather than Eq. (1). In calculating  $P_{enh}$ , the pinch radius at stagnation was taken 0.5 mm, as inferred from the x-ray images of Ref. 11. The yield  $Y_{FP}$  corresponds to the energy emitted during the first radiation pulse, to be consistent with the above value of the pinch radius. The agreement between  $E_k + E_{enh}$  and  $Y_{FP}$  is found to be quite good, except for the two shots with the highest load masses. It is not clear, however, whether our estimates are applicable to the latter cases, for which the observed implosion times were considerably longer than those predicted by the circuit model.<sup>11</sup>

In the long-pulse Saturn experiments with aluminum wire arrays,<sup>12</sup> the excess of the total yield over the 0-D kinetic energy for the best shots was even higher, up to  $(1160 \text{ kJ})/(280 \text{ kJ}) \approx 3.8$ . The data first reported in Ref. 12, which will be published in detail elsewhere, was obtained in collaboration with C. A. Coverdale using calibrated bolometers in the same way as done for tungsten in Ref. 11. Substituting parameters of these experiments (current from 7 to 8 MA, line mass from 328 to 957  $\mu\text{g/cm}$ , pinch radius at stagnation  $\sim 1 \text{ mm}$ ) into Eq. (34), we find that  $P_{enh}$  varies in the same range,

between 15 and 23 TW. The increase in the total radiated energy in these long pulse experiments compared to the experiments<sup>10</sup> is basically due to increased confinement time, about 30 ns for the first radiation pulse. A similar estimate of the dissipative energy coupled to the long pulse pinch yields  $\sim 20 \text{ TW} \times 30 \text{ ns} = 600 \text{ kJ}$ , again very close to the difference in experimental radiative yield and 0-D kinetic energy.

It is interesting to compare the resistance (35) to the values of enhanced resistance employed in Ref. 23 to match the experimental results of argon gas-puff implosions on Double Eagle. There it was found that a simple multiplication of the classical Spitzer resistance by a large constant factor was not sufficient to match the experimental results because of the fast decrease of the resistance with increased temperature. The best fit was achieved if the resistance was assumed to correspond to a constant electron temperature  $\sim 20 \text{ eV}$ . Evaluating the electron temperature that would make the classical resistance equal to  $\mathcal{R}_{enh}$  for parameters of these experiments ( $I_m = 3 \text{ MA}$ ,  $l = 4 \text{ cm}$ ,  $\mu = 100 \text{ } \mu\text{g/cm}$ ,  $R_f$  from 1.5 to 2 mm), we obtain the values in the range from 18 to 27 eV, very close to the above estimate.

The 2-D simulations demonstrate decrease in the inductance of the imploding Z-pinch compared to the 0-D slug model (Fig. 14 of Ref. 6), which appears to be consistent with experimental data. Since the thermodynamic free energy<sup>24</sup> for arbitrary distribution of a given current  $I$  is  $\tilde{\mathcal{F}} = -LI^2/2c^2$ , the  $\mathbf{J} \times \mathbf{B}$  forces are always directed so as to increase the inductance  $L$ , thereby decreasing  $\tilde{\mathcal{F}}$ . How could additional degrees of freedom in 2 dimensions lead to decreasing the inductance  $L$  rather than make it increase even faster? The concept of rising magnetic bubbles helps understand this. As the bubble is formed [Fig 1(a)], magnetic flux is supplied to it directly from the power source, and

the inductance of the load increases accordingly. However, as soon as the current reconnects, and the fully formed flux tube penetrates into the pinch column, it is also disconnected from the driver [Fig 1(b)], decreasing the volume where the driver current creates magnetic flux, and thereby, decreasing the load inductance. The nonlinear resistance (3) exactly corresponds to the rate of magnetic flux losses from the driver circuit to the magnetic bubbles:  $I\mathcal{R}_{enh} = (1/c)(d\Phi_b/dt)$ .

Analysis of these and many other examples demonstrates that our expression (34) for the enhanced dissipation power  $P_{enh}$  is consistent with the available experimental data and simulation results. This agreement adds credibility to the physical assumptions of the bubble model from which the formula is derived. In what follows, we apply this formula to reconsider an old problem of power balance in a steady-state Z-pinch, and to analyze a new challenge of producing K-shell radiation in long-pulse Z-pinch implosions.

#### B. Power balance in an equilibrium Z-pinch

Consider a steady-state Z-pinch in pressure (Bennett) and power balance, where radiation losses are exactly equilibrated by Ohmic heating. Then the classical Spitzer expression for the heating term leads to a single characteristic value of current at which the equilibrium is possible,  $I_{PB}$ , the well-known Pease-Braginskii current.<sup>25</sup> In Section III.B we have shown, however, that the enhanced dissipation (34) dominates over the Ohmic dissipation over the whole relevant range of Z-pinch parameters. In view of this, the conditions for power balance in a steady-state Z-pinch have to be reconsidered.

Following Ref. 25, let us assume that radiation losses from the pinch are primarily due to bremsstrahlung, which is the case for fully stripped hydrogen or other low-Z plasma that does not emit any lines or recombination radiation. The power of

bremsstrahlung radiation losses from a fully ionized, optically thin Z-pinch plasma column is estimated as

$$P_{brems} = \frac{16}{3} \left( \frac{2\pi}{3} \right)^{1/2} \frac{Z^3 e^6 n^2 T_e^{1/2}}{m_e^{3/2} c^3 \hbar} \cdot \pi R^2 l = \frac{4}{3} \left( \frac{2}{3\pi} \right)^{1/2} \frac{Z e^6}{m_e^{3/2} m_u^2 c^3 \hbar} \cdot \frac{\mu^2 T_e^{1/2} l}{R^2}. \quad (40)$$

Let us assume the power balance,  $P_{brems} = P_{enh}$ , and express the equilibrium electron temperature  $T_e$  in (40) from the Bennett equilibrium condition (5), where we assume  $\bar{Z} = Z$ , as in the original analysis.<sup>25</sup> In contrast with the case of classical Ohmic heating, the radial dependence of the enhanced dissipation (34),  $\propto R^{-1}$ , is different from the radiative power,  $\propto R^{-2}$ . Consequently, the pinch radius now enters the equilibrium condition, making the equilibrium possible for any values of current and mass. The equilibrium condition can be presented as

$$\begin{aligned} \mu_{eq}(I_m, R, Z) &= \frac{3^{3/4} \pi^{1/4} (m_e m_u)^{3/4} (c\hbar)^{1/2} (1+Z)^{1/4} I_m R^{1/2}}{2^{7/4} e^3 Z^{3/4}} \\ &= 332 \frac{(1+Z)^{1/4}}{Z^{3/4}} I_m (\text{MA}) R^{1/2} (\text{mm}) \mu\text{g/cm}. \end{aligned} \quad (41)$$

As seen from (41), the equilibrium condition is fairly close to the relevant range of the experimental Z-pinch parameters. For instance, taking a fully ionized neon plasma ( $Z = 10$ ) “cooking” in an equilibrium at  $I_m = 18$  MA,  $R = 1$  mm, we find:

$\mu_{eq} = 1940 \mu\text{g/cm}$ . This corresponds to a Bennett temperature of 1.58 keV, which is consistent with the full ionization of neon. Since  $P_{brems} \propto R^{-2}$  and  $P_{enh} \propto R^{-1}$ , the power equilibrium in an optically thin Z-pinch is unstable: e. g., a small increase  $\delta R$  of the pinch radius causes  $P_{enh}$  to decrease less than  $P_{brems}$ , thus creating an imbalance in favor of



heating and further expansion. Consequently, a pinch with line mass  $\mu > \mu_{eq}$  for a given  $I_m$  and  $R$  is predicted to collapse, a pinch with  $\mu < \mu_{eq}$  - to bounce.

Note that, similarly to the case originally analyzed by Pease and Braginskii,<sup>25</sup> existence of the equilibrium does not guarantee that we can organize the implosion to a given final radius, say, 1 mm in such a way that the pinch does not bounce. Otherwise, a bremsstrahlung-only PRS powered by the enhanced dissipation could have been an attractive option, particularly for generating harder x-rays. At the moment, however, such a PRS design does not appear feasible because a fully ionized high-Z plasma is more likely to bounce from the axis (since the rate of radiation losses is not high enough to ensure inelastic implosion) than to remain stagnated near it. It would be instructive, however, to use the above formulas for estimating the parameters of bremsstrahlung-only PRS. These results are interesting as the worst-case estimates for the driver parameters required for producing the given amount of x-ray energy in the given spectral range at a given efficiency. Presumably, the requirements on the pulsed power driver will be less demanding if more effective line radiation mechanisms are used to provide the desired x-ray output.

Since the spectrum of thermal bremsstrahlung radiation is exponential,  $J_\omega d\omega \propto \exp(-\hbar\omega/T)d\omega$  (the temperature is expressed in energy units), we conclude that the fraction  $\eta$  of the total energy emitted by the optically thin pinch in the spectral range  $\hbar\omega > E$  is estimated as  $\eta = \exp(-E/T_B)$ , where  $T_B$  is the Bennett temperature (5). Therefore,

$$T_B = \frac{E}{\ln(1/\eta)}. \quad (42)$$

On the other hand, to make the bremsstrahlung emission most effective, we must have  $Z$  as high as possible, which leads to an estimate

$$T_B = I_H Z^2, \quad (43)$$

where  $I_H = 13.6$  eV is the ionization energy of hydrogen. Substituting (41)-(43) into (5), we find the following estimates for the pinch current  $I$ , line mass  $\mu$ , ion and electron densities,  $n_i$  and  $n_e$ , enhanced resistivity per cm,  $\mathcal{R}_{enh}$  and the resistive voltage drop,  $U_{enh}$ , that correspond to generating a fraction  $\eta$  of the total radiation in the spectral range  $\hbar\omega > E$  by bremsstrahlung mechanism in a “cooking” quasi-steady Z pinch of radius  $R$  powered by the enhanced energy dissipation:

$$I = 10.9 \frac{E^{3/4}(\text{keV}) R^{1/2}(\text{mm})}{[\ln(1/\eta)]^{3/4}} \text{MA}, \quad (44)$$

$$\mu = 1240 \frac{E^{1/2}(\text{keV}) R(\text{mm})}{[\ln(1/\eta)]^{1/2}} \mu\text{g/cm}, \quad (45)$$

$$n_i = \frac{1.38 \cdot 10^{21}}{R(\text{mm})} \text{cm}^{-3}, \quad n_e = \frac{1.18 \cdot 10^{22} E^{1/2}(\text{keV})}{R(\text{mm})} \text{cm}^{-3}, \quad (46)$$

$$\mathcal{R}_{enh} = 0.155 \frac{E^{1/2}(\text{keV})}{[\ln(1/\eta)]^{1/2} R(\text{mm})} \text{Ohm/cm}, \quad (47)$$

$$U_{enh} = 1.69 \frac{E^{5/4}(\text{keV})}{[\ln(1/\eta)]^{1/4} R^{1/2}(\text{mm})} \text{MV/cm}. \quad (48)$$

Parameters characteristic of such PRS regimes operating at the efficiency 5% and 10% for  $\hbar\omega > 2$  keV, 4 keV, and 13 keV, are shown in Table 3. These are indeed seen to correspond to the worst-case scenario of x-ray generation: production of Al, Ar and Ti K-shell radiation at the same level of efficiency on Saturn and Z was possible at lower current levels at stagnation than 8 and 13.5 MA, respectively. Therefore, it would be

reasonable to expect that production of x-ray radiation in the spectral range 13 keV at 5% efficiency is possible at current levels below 32 MA.

If the radiative energy losses, as happens in most cases, are determined by mechanisms different from bremsstrahlung, then the equilibrium condition (41) should be modified appropriately. Our above conclusion that the power balance is possible for any pinch current obviously remains valid. Whether the corresponding equilibrium would be unstable, as described above, depends primarily on the opacity of the pinch plasma. If the pinch were optically thick, so that a substantial fraction  $\epsilon$  of its radiation was trapped, then an increase  $\delta R$  in the pinch radius would cause the optically thick radiation losses to increase proportionally to the increased surface area of the pinch, that is, by  $\epsilon \delta R / R$ . On the other hand, the optically thin radiation losses would decrease as  $-(1 - \epsilon) \cdot 2 \delta R / R$ , making the total variation proportional to  $(3\epsilon - 2) \delta R / R$ . If this exceeds the variation of the enhanced dissipation with  $\delta R$ ,  $-\delta R / R$ , then the imbalance would be in favor of radiation losses, causing the pinch to contract back to its initial equilibrium radius. The condition for this is  $\epsilon > 1/3$ . In other words, if the pinch were optically thick for more than 30% of its radiation, then the steady state corresponding to the power balance would be stable. Indeed, calculations of radiation losses in a krypton Z-pinch in the temperature range from 0.4 to 2 keV with line opacity taken into account<sup>26</sup> demonstrate that for a given value of  $\mu$  the total emission power can decrease with increased  $R$  slower than  $1/R$ , cf. Fig. 3 of Ref. 26.

### C. K-shell Plasma Radiation Source powered by enhanced dissipation

The imploding Z-pinchs used as plasma radiation sources are copious sources of x-rays in the range up to several keV that corresponds with the K-shell emission of argon

and titanium.<sup>1,27</sup> Optimal K-shell PRS load design is based on the zero and one-dimensional analyses<sup>7,28-30</sup> that lead to a requirement that the kinetic-energy-per-ion in the imploded plasma must be high enough to provide efficient conversion of kinetic energy into radiation. According to the 1-D analysis, the main energy source for the K-shell radiation is the kinetic energy, which must be converted into thermal energy at stagnation rapidly enough to provide ionization to He- and H-like states before too much energy is lost through softer x-ray emission.

The kinetic energy (1) of the imploding plasma, available for conversion into thermal energy and then to radiation, scales as  $m_i(R_i/\tau)^2/2$ , where  $R_i$  is the initial radius of the pinch,  $\tau$  is the current rise time. For effective K-shell radiation, the kinetic energy must exceed the threshold energy  $E_i$  needed to strip the ion down to the K-shell, by a factor of  $\eta \sim 2.5$  to 3. Therefore, the ratio  $R_i/\tau$  scales as  $\sqrt{\eta E_i/m_i}$ . Advancement to higher energy of x-rays involves using high-Z materials. Since  $E_i$  scales as  $\sim Z^{3.662}$ , see Ref. 30,  $m_i$  scales as  $Z$ , and the energy of the K-shell quanta  $\hbar\omega$  scales as  $Z^2$ , we find that  $R_i$  scales as  $\tau(\hbar\omega)^{0.666}$ . If we need to generate harder x-rays (increase  $\hbar\omega$ ), and want to use for this purpose a low-cost, long implosion current driver (increase  $\tau$ ), then the initial radius  $R_i$  of the imploded shell should be increased accordingly. This means a stronger distortion of the shell by the RT instability during the run-in phase,<sup>31</sup> which might result in a low quality of implosion, producing little or no K-shell radiation at all.

The above problem could possibly be mitigated if we consider an alternative power source provided by enhanced dissipation. Let fast thermalization of kinetic energy of implosion produce rapid ionization. However, once the K-shell plasma has been

produced in the Z-pinch, it could be maintained in a quasi-steady state by continuously coupling the magnetic energy to the plasma column via the enhanced dissipation mechanism. Then the pinch would be "cooked" near the axis for a long time, producing K-shell radiation. The enhanced dissipation mechanism could also be used to facilitate ionization to the He- and H-like states, if a pinch of a relatively large mass is imploded from a small radius at an earlier stage of the current pulse rise. Then both electron-ion temperature equilibration and ionization would take place in a denser plasma, characterized by a larger "confinement parameter"  $n\tau_A \propto \mu^{3/2} / IR$ .

The recent results on long-pulse Al implosions on Saturn<sup>12</sup> provide some indications that the K-shell emission in the "cooking" regime is possible. Let us find out whether the enhanced dissipation (34) indeed represents a sufficient energy source for maintaining the inner core of the "cooking" plasma column in the K-shell ionization state, thereby producing appreciable K-shell yield.

We simulated evolution of an argon plasma column, using the 1-D radiative-MHD code described in Ref. 29. The code was modified to include the enhanced dissipation energy source in the simplest way, by distributing the additional power (34) uniformly over the plasma mass. This kind of simulation, though not a self-consistent treatment of the foam-like plasma described by the model of Section II, appears to be accurate enough for the proof-of-the-principle estimates.

Running the code for an argon pinch driven by the Double Eagle circuit, we have verified that the additional resistance (35) plays a minor role before stagnation, as explained in Section III.B, so that the pinch peak current and the implosion time remain in agreement with the experimental data, as they were without the extra term.<sup>29</sup> Then a

series of runs was done for a plasma column carrying a constant current  $I = I_m = 4 \text{ MA}$ , and starting from a Bennett equilibrium at  $R = 3 \text{ mm}$ . The results are presented in Figs. 3-5.

Figure 3 shows the time history of the pinch parameters for a low-mass plasma column,  $\mu = 100 \text{ } \mu\text{g/cm}$ . After some early bounces, the column expands, as expected from the results of Section IV.B. The enhanced dissipation decreases, and so does the radiation power, due to decreasing density. Plasma temperature remains approximately constant,  $\sim 2 \text{ keV}$ , quite close to the Bennett temperature for the given current and mass,  $1.67 \text{ keV}$ . Conversely, high load mass  $\mu = 400 \text{ } \mu\text{g/cm}$  produces much higher radiation losses (Fig. 4), which results in a radiative collapse of the pinch, whose temperature remains below  $200 \text{ eV}$ , considerably less than the Bennett temperature.

The efficient quasi-steady conversion of magnetic energy into K-shell radiation in the “cooking” regime is achieved for the optimal choice of the load mass,  $\mu = 200 \text{ } \mu\text{g/cm}$ . Figure 5 demonstrates the pinch slowly contracting in  $60 \text{ ns}$  from the initial  $3 \text{ mm}$  radius to the final  $1 \text{ mm}$  radius. The average temperature stays close to the Bennett value,  $0.83 \text{ keV}$ . The average K-shell power maintained during the last  $50 \text{ ns}$  is about  $0.8 \text{ TW/cm}$ , which corresponds to a very substantial K-shell yield of  $40 \text{ kJ/cm}$ .

Of course, much more work is needed to provide a self-consistent numerical analysis of the K-shell radiation generation in the “cooking” regime based on the model of Section III. Still, the present numerical results demonstrate that the enhanced dissipation mechanism described in this paper is a sufficiently strong energy source to support a high-power K-shell radiator in a quasi-steady regime for tens of nanoseconds. These results confirm a high potential of the additional energy source for K-shell PRS,

which justifies further studies, particularly for the purpose of producing K-shell radiation of high-Z elements in the long-pulse regime.

## V. Conclusions

We have developed a quasi-1-D model of enhanced energy dissipation in a Z-pinch, advancing the bubble model suggested in Ref. 5. Explicit formulas for the average enhanced dissipation rate and the corresponding contribution to the resistance of the load have been derived and favorably compared to the experimental data and simulation results. We have demonstrated that the model shows promise of capturing the essential physics of the enhanced energy deposition mechanism, which is a sufficient reason to stimulate its further development. Typically, the energy coupling through this mechanism contributes from 50 to 75% of the total Z-pinch energy balance. This mechanism of energy coupling, which in the relevant parameter range always dominates over the classical resistance during the stagnation phase, must be taken into account when the power balance in a radiating Z-pinch is analyzed. Having re-done the Pease-Braginskii's type of power balance analysis,<sup>25</sup> we have shown that a quasi-steady-state equilibrium is possible for any pinch current at any radius, and that the equilibrium would be stable or unstable depending on whether the pinch plasma column is optically thin or thick to its own radiation. The results of our 1-D numerical simulations clearly demonstrate the feasibility of generating appreciable amounts of argon K-shell radiation in a quasi-steady Z-pinch column powered mainly by the enhanced dissipation.

To advance further, a self-consistent treatment of the enhanced dissipation mechanism in a simulation is needed in order to make more quantitative comparisons

between calculations and experiments. This self-consistent model will help us investigate the issue of pinch radii, both K-shell and L-shell, that presently are not very well reproduced in available simulations, cf. the discussion in Ref. 32. We believe that our approach will help address one of the recurring issues of the Z-pinch physics that still plagues both 1-D and 2-D simulations, the problem of radiative collapse. Recall that the azimuthal magnetic field carried by the bubbles responds to transverse compression as an ideal gas with  $\gamma_{eff} = 2$ , as explained in Ref. 24. That is, the bubble component of the foam-like Z-pinch plasma is much stiffer than the radiating plasma component, whose effective  $\gamma$  is close to unity. Both saturation of the pinch column with the bubbles and conversion of their energy into the thermal energy of the plasma add to the build-up of the plasma counter-pressure, thus tending to stop the collapse. Development of the fully self-consistent 1-D radiation hydro code that accounts for the enhanced dissipation through the bubble model described in Section III is presently under way.

Finally, we would like to highlight the fact that some of the basic physical assumptions of the bubble model could be experimentally tested even before any predictions made with a self-consistent 1-D code become available. First of all, the main feature of the model is the concept of the pinch plasma as a foam-like medium saturated with the bubbles containing axial magnetic field. Measuring the azimuthal magnetic field inside the pinch could test this concept. Our prediction is that the magnetic field does not decay near the pinch axis; rather, inside of the pinch column it remains of the same order as the field near the pinch boundary.

Another possible test involves directly affecting bubble formation and penetration to the axis in an experiment. Suppose that for given experimental conditions the observed



pinch radius at stagnation is 1 mm. Let a 1-mm radius plastic cylinder be mounted at the pinch axis, in the same way as done in the experiments on dynamic hohlraum.<sup>33</sup> Its presence would not prevent the plasma from converging to about the same final radius. However, when the pinch plasma is stagnated near this cylinder, no magnetic bubble could penetrate through the plastic to the axis, coupling additional energy to the plasma. Our prediction is that in this case the total radiative energy output will decrease by a factor of 2 or more compared to the case when there is no obstacle at the axis. A fair estimate for the radiative yield in this case would be the kinetic energy gained by the plasma shell during the run-in phase.

#### Acknowledgements

The authors thank J. P. Apruzese, K. G. Whitney, A. E. Robson, M. Krishnan, R. B. Baksht, I. Vitkovitsky, and D. L. Peterson for many helpful discussions. Contribution of C. A. Coverdale to the long-pulse Al radiation measurements on Saturn is gratefully acknowledged. This work was supported by Defense Threat Reduction Agency MIPR 99-2011/1363.

## References

- <sup>1</sup> N. R. Pereira and J. Davis, J. Appl. Phys. **64**, R1 (1988).
- <sup>2</sup> J. C. Riordan, J. S. Pearlman, M. Gersten, and J. E. Rauch, in *Sub-Kilovolt X-ray Emission from Imploding Wire Plasmas*, AIP Conf. Proc. No. 75, edited by D. Attwood and B. Henke (American Institute of Physics, New York, 1981), p. 35.
- <sup>3</sup> M. Krishnan, C. Deeney, T. Nash, P. D. LePell, and K. Childers, in *Dense Z-Pinches*, AIP Conf. Proc. No. 195, edited by N. R. Pereira, J. Davis and N. Rostoker (American Institute of Physics, New York, 1989), p. 17.
- <sup>4</sup> D. G. Colombant, M. Lampe, J. Davis and H. W. Bloomberg, "Dynamics and radiative Yields from Aluminum Multiple Wire Arrays," NRL Memorandum Report 3840, Naval Research Laboratory, Washington, D. C. 20375 (1978); copies may be ordered from NTIS, Springfield, VA 22161, order no. ADA059883.
- <sup>5</sup> L. I. Rudakov and R. N. Sudan, Phys. Reports **283**, 253 (1997).
- <sup>6</sup> D. L. Peterson, R. L. Bowers, K. D. McLenithan, C. Deeney, G. A. Chandler, R. B. Spielman, M. K. Matzen, and N. F. Roderick, Phys. Plasmas **5**, 3302 (1998).
- <sup>7</sup> J. Katzenstein, J. Appl. Phys. **52**, 676 (1981).
- <sup>8</sup> R. B. Baksht, S. P. Bugaev, I. M. Datsko, A. A. Kim, B. M. Kovalchuk, V. A. Kokshenev, G. A. Mesyats, Laser and Particle Beams **11**, 587 (1993).
- <sup>9</sup> J. C. Riordan, P. L. Coleman, B. H. Failor, J. S. Levine, Y. Song, E. M. Waisman, C. Deeney, J. S. McGurn, J. P. Apruzese, J. Davis, A. Fisher, B. Moosman, J. W. Thornhill, B. V. Weber, K. G. Whitney, Bull. Am. Phys. Soc. **43**, 1905 (1998).
- <sup>10</sup> C. Deeney, T. J. Nash, R. B. Spielman, J. F. Seaman, G. C. Chandler, K. W. Struve, J. L. Porter, W. A. Stygar, J. S. McGurn, D. O. Jobe, T. L. Gilliland, J. A. Torres,

- M. F. Vargas, L. E. Ruggles, S. Breeze, R. C. Mock, M. R. Douglas, D. L. Fehl, D. H. McDaniel, M. K. Matzen, D. L. Peterson, W. Matuska, N. F. Roderick, and J. J. MacFarlane, *Phys. Rev. E* **56**, 5945 (1997).
- <sup>11</sup> C. Deeney, C. A. Coverdale, M. R. Douglas, K. W. Struve, R. B. Spielman, W. A. Stygar, D. L. Peterson, N. F. Roderick, M. G. Haines, F. N. Beg, and J. Ruiz-Camacho, *Phys. Plasmas* **6**, 3576 (1999).
- <sup>12</sup> M. R. Douglas, C. Deeney, R. B. Spielman, N. F. Roderick, and M. G. Haines, in *IEEE Conference Record – Abstracts, IEEE International Conference on Plasma Science*, June 20-24, 1999 Monterey, CA (Institute of Electrical and Electronics Engineers, Piscataway, NJ, 1999), p. 230; C. Deeney, M. R. Douglas, C. A. Coverdale, R. B. Spielman, D. L. Peterson, N. F. Roderick, M. G. Haines, T. J. Nash, M. Derzon, J. McGurn, D. Jobe, T. Gilliland, S. Breeze, J. Torres and J. F. Seamen, *ibid*, p. 232.
- <sup>13</sup> C. Deeney, M. R. Douglas, R. B. Spielman, T. J. Nash, D. L. Peterson, P. L'Eplattenier, G. A. Chandler, J. F. Seamen, and K. W. Struve, *Phys. Rev. Lett.* **81**, 4883 (1998).
- <sup>14</sup> G. K. Batchelor, *Fluid Dynamics* (Cambridge University Press, Cambridge, 1967), p. 339.
- <sup>15</sup> E. N. Parker, *ApJ*. **121**, 491 (1955); *Cosmical Magnetic Fields* (Clarendon, Oxford, 1979).
- <sup>16</sup> B. B. Kadomtsev, in *Reviews of Plasma Physics*, edited by M. A. Leontovich (Consultants Bureau, New York, 1966), Vol. 2, p. 153.
- <sup>17</sup> W. M. Manheimer, *Phys. Fluids* **17**, 1767 (1974).

- <sup>18</sup> D. L. Youngs, *Physica D* **12**, 32 (1984); K. I. Read, *Physica D* **12**, 45 (1984).
- <sup>19</sup> J. Davis, N. A. Gondarenko, and A. L. Velikovich, *Appl. Phys. Lett.* **70**, 170 (1997);  
R. E. Terry, J. Davis, C. Deeney, and A. L. Velikovich, *Phys. Rev. Lett.* **83**, 4305  
(1999).
- <sup>20</sup> D. Bohm, in *The Characteristics of Electrical Discharges in Magnetic Fields*, edited  
by A. Guthrie and R.K. Wakerling, (McGraw-Hill, New York , 1949), pp. 1, 87.
- <sup>21</sup> J. Lindl, *Phys. Plasmas* **2**, 3933 (1995); S. E. Bodner, D. G. Colombant, J. H. Gardner,  
R. H. Lemberg, S. P. Obenschain, L. Phillips, A. J. Schmitt, J. D. Sethian,  
R. L. McCrory, W. Seka, C. P. Verdon, J. P. Knauer, B. B. Afeyan, and H. Powell,  
*Phys. Plasmas* **5**, 1901 (1998).
- <sup>22</sup> R. B. Spielman, C. Deeney, G. A. Chandler, M. R. Douglas, D. L. Fehl, M. K. Matzen,  
D. H. McDaniel, T. J. Nash, J. L. Porter, T. W. L. Sanford, J. F. Seamen, W. A. Stygar,  
K. W. Struve, S. P. Breeze, J. S. McGurn, J. A. Torres, D. M. Zagar, T. L. Gilliland,  
D. O. Jobe, J. L. McKenney, R. C. Mock, M. Vargas, and T. Wagoner, *Phys Plasmas*  
**5**, 2105 (1998).
- <sup>23</sup> C. Deeney, P. D. LePell, B. H. Failor, J. S. Meachum, S. Wong, J. W. Thornhill,  
K. G. Whitney, and M. C. Coulter, *J. Appl. Phys.* **75**, 2781 (1994).
- <sup>24</sup> L. D. Landau and E. M. Lifshitz, *Electrodynamics of Continuous Media* (Pergamon,  
New York, 1984).
- <sup>25</sup> R. S. Pease, *Proc. Phys. Soc. London* **B70**, 11 (1957); S. I. Braginskii, *Sov. Phys. JETP*  
**6**, 494 (1958).
- <sup>26</sup> J. P. Apruzese and P. Kepple, *op. cit.* in Ref. 3, p. 108.
- <sup>27</sup> C. Deeney, C. A. Coverdale, M. R. Douglas, T. J. Nash, R. B. Spielman, K. W.

- Struve, K. G. Whitney, J. W. Thornhill, J. P. Apruzese, R. W. Clark, J. Davis, F. N. Beg, and J. Ruiz-Camacho, *Phys. Plasmas* **6**, 2081 (1999).
- <sup>28</sup> D. Mosher, "Coupling of Imploding Plasma Loads to High Power Generators," NRL Memorandum Report 3687, Naval Research Laboratory, Washington, D.C. 20375, 1978; copies may be ordered from NTIS, Springfield, VA 22161, order no. ADA052575; S. Wong, C. Gilman, P. Sincerny, Y. Young, IEEE Conference Record – Abstracts, IEEE International Conference on Plasma Science, Ottawa, 1982 (Institute of Electrical and Electronics Engineers, Piscataway, NJ, 1982), p. 37; M. Gersten, W. Clark, J. E. Rauch, G. M. Wilkinson, J. Katzenstein, R. D. Richardson, J. Davis, D. Duston, J. P. Apruzese, and R. Clark, *Phys. Rev. A* **33**, 477 (1986); J. P. Apruzese and J. Davis, "K-shell Yield Scaling Law for Conventional PRS Loads," NRL Memorandum Report 5406, Naval Research Laboratory, Washington, D.C. 20375 (1984); copies may be ordered from NTIS, Springfield, VA 22161, order no. ADA145155; K. G. Whitney, J. W. Thornhill, J. P. Apruzese, and J. Davis, *J. Appl. Phys.* **67**, 1725 (1990);
- <sup>29</sup> J. W. Thornhill, K. G. Whitney, and J. Davis, *J. Quant. Spectr. Rad. Transfer* **44**, 251 (1990).
- <sup>30</sup> K. G. Whitney, J. W. Thornhill, J. L. Giuliani, Jr., J. Davis, L. A. Miles, E. E. Nolting, V. L. Kenyon, W. A. Speicer, J. A. Draper, C. R. Parsons, P. Dang, R. B. Spielman, T. J. Nash, J. S. McGurn, L. E. Ruggles, C. Deeney, R. R. Prasad, and L. Warren, *Phys. Rev. E* **50**, 2166 (1994).
- <sup>31</sup> F. L. Cochran, J. Davis, and A. L. Velikovich, *Phys. Plasmas* **2**, 2765 (1995).
- <sup>32</sup> J. H. Hammer, J. L. Eddleman, P. Springer, M. Tabak, A. Toor, K. Wong,

- G. B. Zimmerman, C. Deeney, R. Humphreys, T. J. Nash, T. W. L. Sanford,  
R. B. Spielman and J. S. DeGroot, *Phys. Plasmas* **3**, 2063 (1996).
- <sup>33</sup> T. J. Nash, M. S. Derzon, G. A. Chandler, R. Leeper, D. Fehl, J. Lash, C. Ruiz,  
G. Cooper, J. F. Seaman, J. McGurn, S. Lazier, J. Torres, D. Jobe, T. Gilliland,  
M. Hurst, R. Mock, P. Ryan, D. Nielsen, J. Armijo, J. McKenney, R. Hawn,  
D. Hebron, J. J. MacFarlane, D. Peterson, R. Bowers, W. Matuska, and D. D. Ryutov,  
*Phys. Plasmas* **6**, 2023 (1999).

### Figure captions

Fig. 1. Magnetic bubbles emerge near the pinch surface and converge to the pinch axis.

(a) A magnetic bubble is formed as a  $m = 0$  RT or MHD perturbation at the pinch surface. The plasma closes back behind it, producing a flux ring that carries magnetic flux and magnetic energy. (b) The magnetic bubble is driven to the axis due to both curvature stress and buoyancy force. (c) The bubble, having approached the axis, still carries the same amount of magnetic flux, but most of its energy has been dissipated in the plasma.

Fig. 2. Correlation between the total peak radiation power  $P_{rad}$  observed in Saturn and Z experiments, and scaled "cooking" power  $P_{enh} = I_m^3 l / 2c^3 \mu^{1/2} R_f$ . The dotted line corresponds to  $P_{rad} = P_{enh}$ .

Fig. 3. Time histories of radiation power and electron temperature for a low-mass carrying a current 4 MA (radial expansion).

Fig. 4. Same as in Fig. 3 for a high-mass argon plasma column (radiative collapse).

Fig. 5. Same as in Figs. 3, 4 for an optimal mass of an argon plasma column (efficient K-shell radiation generation in a "cooking" regime).

Table 1. Typical parameters, estimated kinetic energies and measured total x-ray yields for PRS experiments

Generator	Material	Ref.	$I_m$ (MA)	$\frac{R_i}{R_f}$	$l$ (cm)	$E_k$ (kJ)	$Y$ (kJ)
GIT-4	W	8	1.5	6	4	10	30
DE	Ar	9	3.5	15	4	80	140
Saturn	W	10	6.6	20	2	157	450
	W	11	8	25	2	250	750
	Al	12	8	20	2	230	1060
Z	W	13	18	25	2	1250	1800

Table 2. Results of the long-pulse Saturn experiments with W wire arrays.<sup>11</sup>

$I_m$ (MA)	$\mu$ ( $\mu\text{g/cm}$ )	$P_{enh}$ (TW)	$P_{rad}$ (TW)	$\tau_{FWHM}$ (ns)	$E_k$ (kJ)	$E_{enh}$ (kJ)	$E_k + E_{enh}$ (kJ)	$Y_{FP}$ (kJ)
6.2	710	18	49	7.5	170	134	304	368
7.4	1530	21	41	14	230	290	520	574
7.8	2160	20	40	14	260	286	546	560
7.9	2300	21	43	14.5	270	298	568	624
8.8	4609	20	30	15.5	316	311	627	465
9.1	6140	19	20	19	310	365	675	380



Table 3. Parameters of bremsstrahlung-only PRS powered by enhanced energy dissipation calculated for the radius of a steady-state Z-pinch  $R = 1$  cm. These could also be interpreted as the worst-case estimates for PRS using more efficient radiation mechanisms.

	Scales with $R_{as}$	$\hbar\omega > 2$ keV		$\hbar\omega > 4$ keV		$\hbar\omega > 13$ keV	
		$\eta = 5\%$	$\eta = 10\%$	$\eta = 5\%$	$\eta = 10\%$	$\eta = 5\%$	$\eta = 10\%$
$I$ (MA)	$R^{1/2}$	8.05	9.8	13.5	16.5	32.8	40
$\mu$ ( $\mu\text{g}/\text{cm}$ )	$R$	1010	1160	1430	1630	2580	2950
$T_B$ (keV)	$R^0$	0.68	0.87	1.33	1.74	4.34	5.65
$Z$	$R^0$	7	8	10	11	18	20
$n_i$ ( $\text{cm}^{-3}$ )	$R^{-1}$	$1.4 \cdot 10^{21}$					
$n_e$ ( $\text{cm}^{-3}$ )	$R^{-1}$	$9.6 \cdot 10^{21}$	$1.1 \cdot 10^{22}$	$1.4 \cdot 10^{22}$	$1.6 \cdot 10^{22}$	$2.5 \cdot 10^{22}$	$2.8 \cdot 10^{22}$
$P$ (TW/cm)	$R^0$	0.41	1.39	1.64	5.55	17.3	58.6
$\mathcal{R}$ (Ohm/cm)	$R^{-1}$	0.13	0.14	0.18	0.20	0.32	0.37

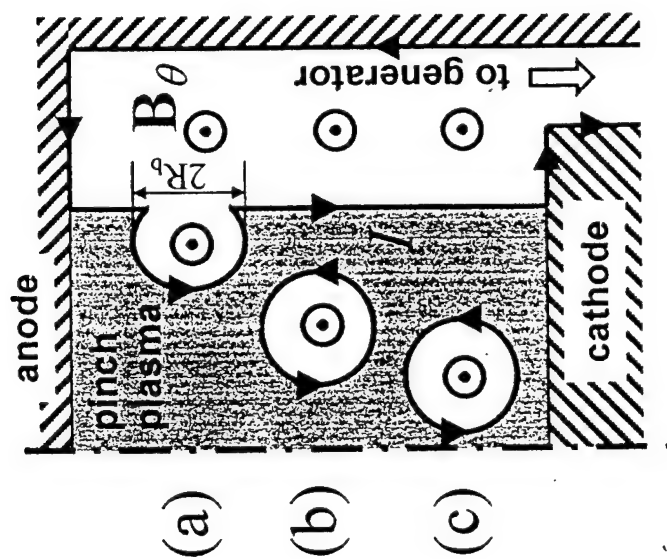


Fig. 1

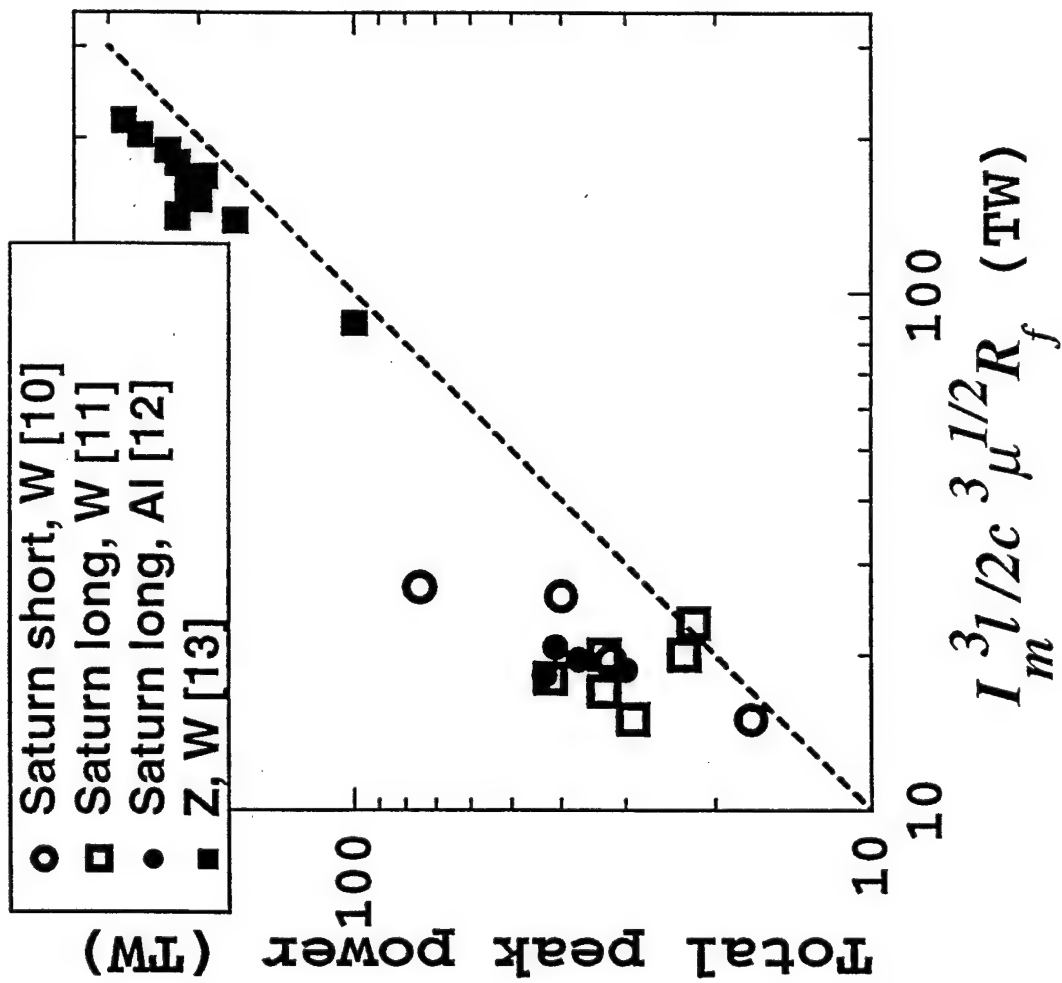


Fig. 2

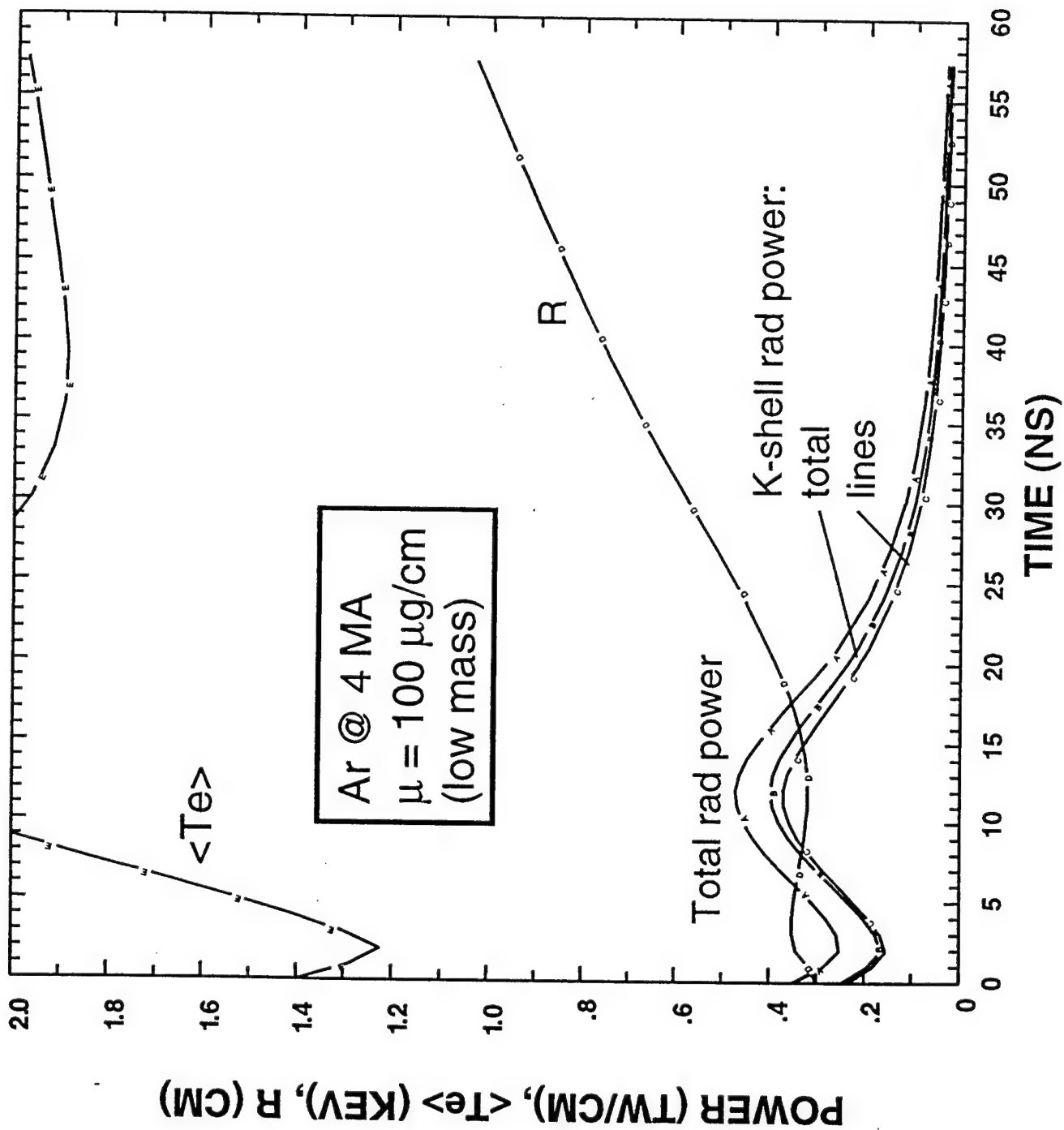


Fig. 3

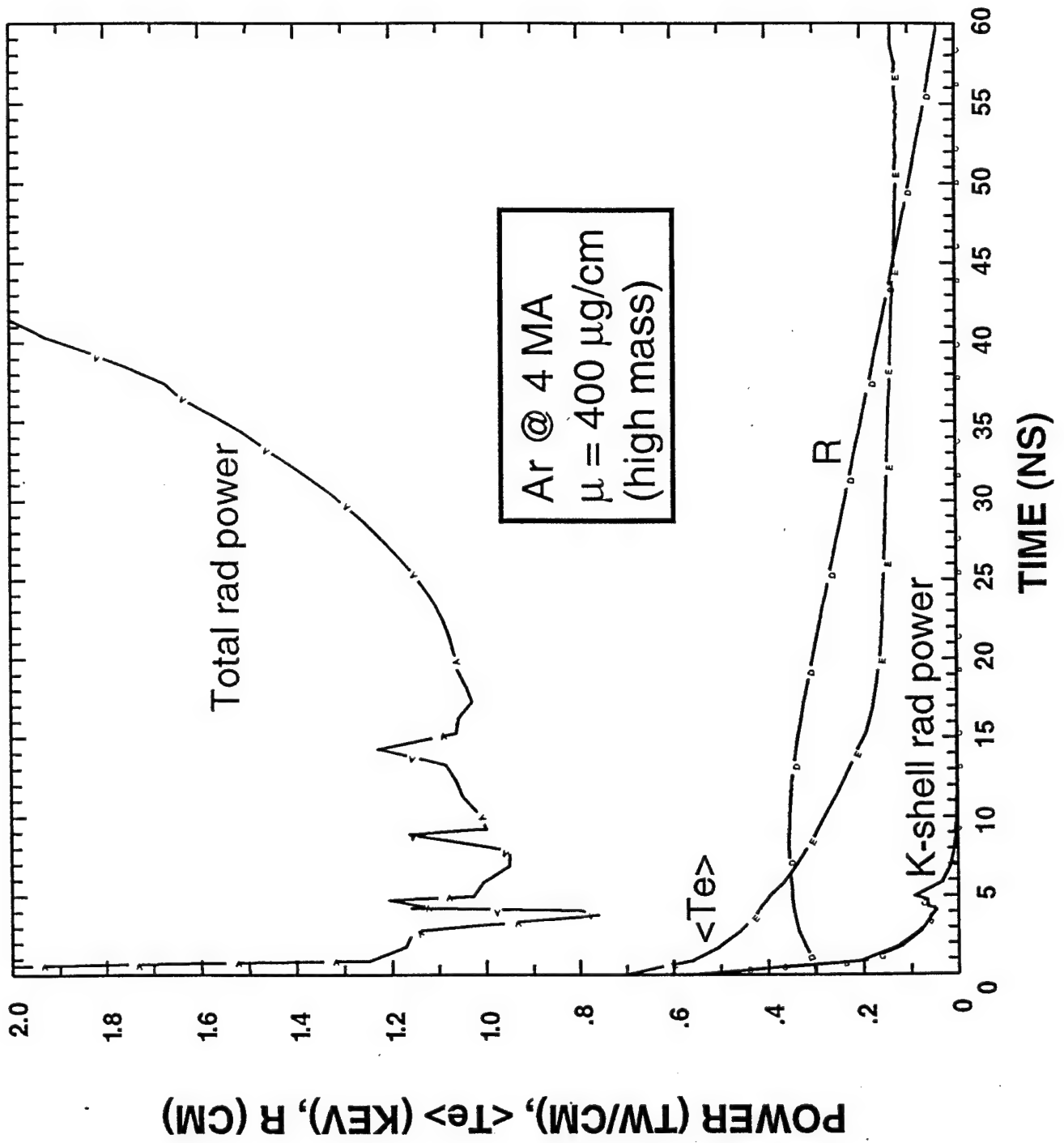


Fig. 4

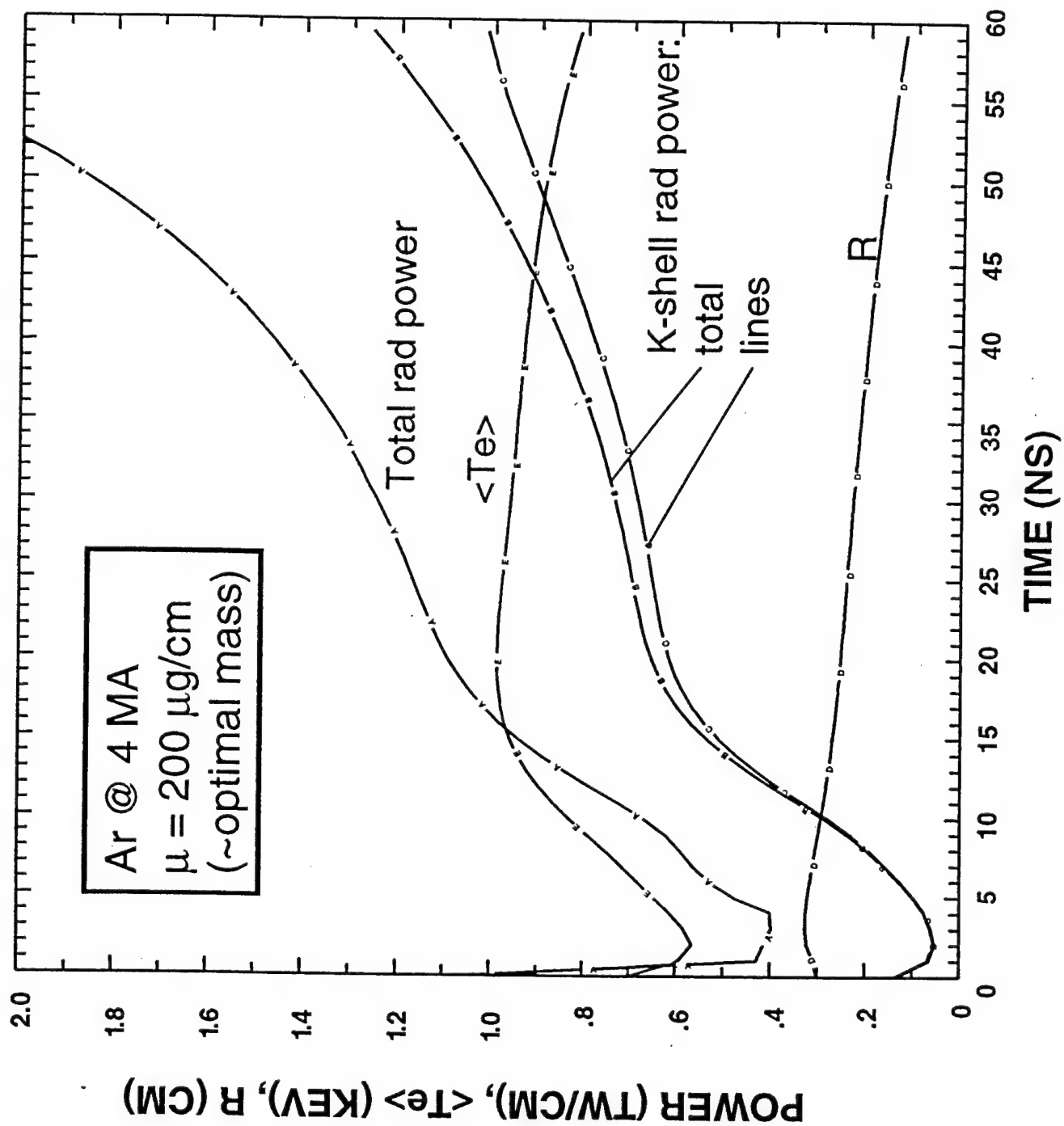


Fig. 5

## II. Comparison of Radiative Properties and Stability of Uniform Fill Versus Annular Shell Z Pinches

### I. Introduction.

Since Z-pinches are very efficient radiators, there is considerable interest in applying them to Inertial Confinement Fusion and to the production of x-rays above 3 keV.[1-3] For both applications, high density, high velocity implosions are needed. The attainment of both high velocities and densities requires large load diameters which, unfortunately, makes these loads more susceptible to the effects of initial asymmetries, as well as to an increase in the growth of Rayleigh-Taylor (RT) instabilities.[4,5] These asymmetries and instabilities can broaden and disrupt the imploding shell thus increasing the radiated pulsewidth and hence reducing the power. The broader shell will also typically produce a larger diameter, lower density pinch which can greatly reduce the production of high energy x-rays.[6]

For these reasons, the reduction of initial asymmetries and the mitigation of instabilities are critical issues for future Z-pinch developments. Various techniques have been suggested to reduce the growth of RT instabilities: snowplow (mass accretion) stabilization being the most favored. Gol'berg and Velikovich,[7] Cochran *et al*, [8] Velikovich *et al*, [9] Douglas *et al* [10] and Hammer *et al* [11] have all shown the theoretical viability of this technique for ideal gas puff Z-pinches that employ a uniform or tailored gas distribution. As pointed out by Cochran *et al*,[8] for the same initial radius, annular loads should have the optimum coupling to the generator, and therefore, in the limit of perfect stability, should produce the highest x-ray yields. However, the level of implosion asymmetry and instability can affect the pinch temperatures and densities thus raising the possibility that the uniform fill loads could radiate more effectively than the annular loads. This paper assesses which nozzle

design, either annular or uniform fill, is optimal for producing high-energy photons for a given element. Because there is a large variation in the flow characteristics of different nozzles, i.e. differences in initial axial non-uniformity, it is difficult to separate effects due to instabilities from those due to axial non-uniformity. The pre-ionization of the gas can add yet another complication, as discussed by Roussikh, *et al.*[12] In many cases, therefore, large number wire array experiments are better suited for isolating effects due to short wavelength instabilities in the radius-z-axis plane for annular implosions. Due to the axial flow gradients, gas puff experimental results are highly dependent on the specific nozzles employed because the annular loads are not really annular nor are the uniform loads exactly uniform. However, for convenience in the remainder of the paper approximately uniform fills will be referred to as uniform fills and approximately annular shells will be referred to as annular. Nevertheless it is still worthwhile to compare the two nozzle designs because, depending on the pulsed power driver, obtaining radiation in certain energy ranges is currently best accomplished by the use of gas puffs. Our investigation is performed primarily by comparing experimental results with the two nozzle designs, and it is further supported by idealized 1D and 2D detailed radiation-MHD calculations.

In initial experiments with uniform fill krypton gas puffs on the 8 MA Saturn generator, Spielman, *et al* [13] showed evidence that the instability growth was indeed reduced. They also showed that uniform fill implosions were more stable, at up to 100 cm/ $\mu$ s implosion velocities, than annular implosions with equivalent velocities. Those experiments, however, did not directly address issues of implosion asymmetries and instabilities, and their effect on x-ray yield and power as a function of atomic number.

This paper extends the analysis of the krypton gas puff experiments by focusing on performance both in terms of stability and radiation output when thick-shell annular versus uniform fill loads are compared with different atomic number elements. The implosion



time was held constant at  $70 \pm 3$  ns, which had previously been determined as the optimum for gas puff implosions on the Saturn generator. The routinely used 2.5-cm diameter annular nozzle, with a 1 cm average shell thickness, and a 4.5 cm uniform fill nozzle were tested. Their characteristics are discussed below. The 4.5-cm nozzle outer diameter was chosen to give a center of mass at a diameter in the range of 2.5 to 2.8 cm, i.e. similar to the annular nozzle. Ne:Ar and Kr:Ar mixtures were chosen to assess the effects of the different atomic numbers. In Table 1 we list the shot parameters discussed in this paper. The argon admixture was used for diagnostic purposes, specifically, it permitted the measurement of the electron densities from spectral data taken with a high resolution Johann spectrometer, as discussed in a paper by Wong, *et al.*[14]

In Section II the Saturn generator and the diagnostic suite are described. The Ne:Ar set of experiments has shown that the x-ray powers and yields are higher from uniform loads than annular loads (Sec. III). The complete set of experiments show that the x-ray power is much larger for the higher atomic number loads e.g. krypton (Sec. IV), and that the uniform fill loads produce higher densities and higher electron temperatures (Sec. V). We discuss these results in Section VI and present our conclusions in Section VII.

## II. The Saturn Generator and Diagnostics.

The experiments with gas puff loads were performed on Saturn which is a 36-module pulsed power generator.[15] Typically, Saturn delivers 8 MA beyond the insulator stack and  $7.3 \pm 0.2$  MA into a gas puff load. Figure 1 shows the typical configuration used in this experiment. This figure shows the four magnetically insulated transmission lines (MITL feeds), the post-hole convolute which couples these lines together into a radial feed. This radial feed region then connects to the load region through a small coaxial section. In Figure 1, the gas puff valve is coupled to a 2.5-cm mean diameter annular nozzle. The gas

puff valve is similar to those described in Reference 16. A solenoid is energized to lift the drum off the o-ring seal thus allowing the gas to flow from the plenum into the annular Laval nozzle. Gas flows from annular nozzles have been characterized in References 17 and 18, and are found to be annular only near the nozzle exit. The further away they are from the exit, the more they expand, approaching a uniform fill near the anode. The anode is composed of a wire mesh that is strung from the eight current return posts. The distance from the nozzle output (cathode) to the anode is 2 cm.

Some gas flows from the nozzle into a small volume containing a charged trigger pin. The breakdown of this trigger pin initiates the firing of the Saturn pulsed power generator. In this configuration, Saturn is fired some 400 to 500  $\mu\text{s}$  after the trigger pin detects the gas flow (flow delay in Table 1) to allow the gas flow to achieve a steady state condition. By varying the gas pressure in the plenum and the flow delay the initial mass of the gas shell and zippering of the implosion along the axis can be controlled. In addition to the flow delay, the annular nozzle is tilted inward by 7.5 degrees to reduce axial zippering.[19-21]

To achieve an approximately uniform gas density profile requires a careful nozzle design. Figure 2 shows a comparison of the annular nozzle and a 4.5-cm-diameter uniform fill nozzle. The uniform fill nozzle is much longer than a standard annular nozzle to allow flow forenough radial transit times to ensure a uniform density profile.

These uniform fill gas puffs and nozzles have been characterized at the Naval Research Laboratory using a He:Ne heterodyne interferometer.[22] Figure 3 shows the normalized radial density profiles, using argon gas, for the 4.5 cm uniform fill nozzle at 0.85 cm downstream from the nozzle exit at a flow time of 750  $\mu\text{s}$  and for the annular nozzle 1.1 cm downstream from the exit with Ar at 700  $\mu\text{s}$ . The density profile is relatively flat for the uniform fill nozzle compared to the annular nozzle. The magnitude of the error bars

is a result of error propagation in the Abel inversion with the limited number of chordal cuts. The error bars are only shown for the uniform fill case since they are the same for the annular nozzle.

Figure 4(a) shows the time history of the average density measured on the centerline at the nozzle exit for the 4.5-cm-diameter uniform nozzle operating at 1000 Torr of Kr:  $t=0$  corresponds to the breakdown of the trigger pin. The 450  $\mu\text{s}$  delay to the start of the gas flow is mainly due to the propagation time down the long nozzle. Optimization of the flow time indicated that the best implosions occurred with delays of 600 to 650  $\mu\text{s}$  for the uniform nozzles. However, since the density is still rising as a function of time, this leads to a gradient in the mass per unit length as shown in Figure 4(b). The gradient is much less for the annular nozzle due to the fact that this nozzle is fired during the constant pressure phase of the gas flow. By scaling the interferometer measurements, we calculate (see Table 1) that the mass loadings are  $180\pm30$  and  $290\pm50$   $\mu\text{g}/\text{cm}$  for the uniform and annular shots, respectively. Using the Saturn circuit model coupled to a zero dimensional implosion model, we infer implosion masses of  $200\pm40$  and  $300\pm60$   $\mu\text{g}/\text{cm}$  from the implosion time measurements for the uniform and annular loads respectively. The circuit calculations also indicate that the implosion kinetic energies are in the range of 100 to 150 kJ.

The Saturn generator is well diagnosed electrically and an accurate circuit model exists to calculate the effects on the circuit of the load dynamics. In particular, calibrated 0.2-mil-thick NiChrome-shielded current probes are located at a 5 cm radius from the pinch: this current is called the feed current. These probes measure the local rate of change of the magnetic field (B-dot probes are integrated numerically to give current). The calibration procedure involves placing the B-dots, which are mounted in the actual anode hardware, into a structure that is fed by a known electrical pulse. These calibrations are accurate to

better than 2%. Calibrated B-dots, which survive multiple shots, are also located in the separate MITLs upstream of the convolute; these measure the current injected past the insulator stack. The individual currents measured on each level at three locations are averaged, then summed for the four levels to give the total MITL current.

A set of photoconductive detectors [23] provided our primary kilovolt radiation diagnostics and a bare nickel bolometer[24] is used to measure the total radiated energy. Based on a series of cross calibrations with various diagnostics, we have determined that the PCDs exhibit calibration variations up to  $\pm 15\%$  so we quote a  $\pm 15\%$  error bar on our power and yield measurements. The relative change over this shot sequence is better than this absolute error. Figure 5 shows the transmissions for the filter sets used in these experiments. A gated, gold-photocathode microchannel-plate (MCP) pinhole camera gave nine 100- $\mu\text{m}$ , 100-ps space- and time- resolved images of the pinch. This camera is referred to as the Large Format Pinhole Camera (LFPHC). This camera was filtered with 4- $\mu\text{m}$  of Lexan or 25.4  $\mu\text{m}$  of beryllium. Another gated MCP camera has two time-integrated strips plus ten time-resolved strips, each with 2-ns pulse duration, gated 3 ns apart. This camera has a magnification factor of 0.5 and is filtered with 8  $\mu\text{m}$  of beryllium. This camera is called the Standard Format Pinhole Camera (SFPHC). These pinhole cameras are similar to those described in Reference 25.

### **III. Neon-Argon Admixture Annular and Uniform Fill Implosions**

Figure 6 shows an example of the measured currents and kilovolt x-ray power from an annular Ne:Ar gas puff implosion (Shot 2110). The measured MITL current (dashed curve) is 9.3 MA with just over 7 MA reaching the load.(solid curve) The emitted kilovolt x-ray pulse has a breadth of 18 ns with a relatively low peak power of  $1.7 \pm 0.3$  TW. The

total kilovolt x-ray yield is  $58 \pm 7$  kJ and the bolometer indicated a total x-ray yield of  $290 \pm 40$  kJ. The total yield exceeds the zero-dimensional implosion kinetic energy of 150 kJ that was calculated for a 10:1 compression ratio. This is likely due to some on-axis heating as discussed by Peterson *et al.* [26] and some PdV compression heating due to soft implosions and precursor plasma as calculated, for example, in Refs. 27 and 28. One interesting feature of the measured x-ray power is the large pre-cursor that correlates to the peak load current. In fact, some 20% of the kilovolt emissions are radiated during the run-in phase. Spielman *et al* [15] observed this on the very first Saturn neon gas puff implosions and explained it by the fact that the ohmic and pdV heating may be enough during the implosion phase to ionize some of the neon into the K-shell. This fact also makes the emissions from the imploding neon shell much easier to image.

In Figure 7 we compare the time-gated images recorded using the SFPHC filtered with (a)  $25.4 \mu\text{m}$  beryllium ( $>800$  eV) and (b)  $50.8 \mu\text{m}$  of kapton ( $>2000$  eV). The softer filtered image shows the imploding sheath at 60 ns whereas the  $>2000$  eV image does not show the imploding sheath. The imploding shell has ring like structures and exhibits  $<1$  mm wavelength, non-linear Rayleigh-Taylor-like structures on the outer edge. The estimated implosion velocity is  $70 \text{ cm}/\mu\text{s}$ . This annular implosion shows a 9 ns axial zipper time and the intrinsic radiation time at any given axial location is about 6 ns.

Since the SFPHC has 1 ns gates, the blurring in the images can be as much as  $700 \mu\text{m}$  ( $70 \text{ cm}/\mu\text{s}$  times 1 ns). The 100 ps resolution of the LFPHC gives much more detail of the imploding shell and the plasma on-axis. In Figure 8, LFPHC images of an annular implosion are shown. Clearly, these implosions are very unstable and asymmetric.

The kilovolt emission characteristics and the on-axis pinch quality and stability both improved when the 4.5-cm-diam. uniform fill nozzle was employed. Figure 9 shows the

measured kilovolt x-ray power and the measured MITL current for shot 2112. Comparing this to the annular data in Figure 6, we note that the pulsewidth has decreased from 18 to 13 ns and the kilovolt power has more than doubled to  $3.8 \pm 0.6$  TW. To aid the comparison, Figure 10 shows the x-ray kilovolt power pulses from an annular shot (2110) and a uniform fill shot (2113). The total kilovolt x-ray yield is larger with the uniform fill nozzle than with the annular nozzle; specifically the yield from the annular shot is 58 kJ compared to 81 kJ with the uniform fill nozzle. A very large increase is observed in the  $h\nu > 2000$  eV emissions which include the Ar K-shell. Figure 11 illustrates the differences in the higher energy PCD channels between the annular and uniform fill nozzles. The  $>2000$  eV emissions increased in power by a factor of 3 and the radiated energies increased from  $8 \pm 1$  kJ to  $25 \pm 3$  kJ. Table 2 summarizes the measured yields, powers, pulsewidths and plasma sizes for all the shots listed in Table 1, including the Kr:Ar mixtures that will be discussed in the next section.

This improved radiation performance can be correlated to the improved assembly dynamics for the uniform fill nozzle. The  $>800$  eV images for (a) an annular implosion and for (b) a uniform fill implosion are contrasted in Figure 12. The uniform fill nozzle implosion exhibits a low level of R-T instability on the outside edge of the imploding plasma and it has a more axially uniform implosion i.e. a zipper time of approximately 3 ns. This is a factor of 3 less zipper time than that of the annular nozzle. With a different tilt angle for the nozzle, the axial zipper could be reduced further as discussed by Deeney *et al.*[21] Potentially, less zippering could improve the implosion and assembly dynamics, but with the present configuration, the power per unit length for the annular implosions was 1.5 TW/cm compared to 2.2 TW/cm for the uniform fill loads. In addition, the intrinsic radiation time at a given axial location appears to be about 3 ns for the uniform fill nozzle implosions. The axial emissions from the uniform-fill implosion are more uniform (20%

variation versus 50% variation with the annular implosion) but the time-integrated pinch diameters are about the same, as shown in Table 2.

From the time-resolved pinhole images, we can also determine that the pinched plasma diameters are about the same for the two nozzles at the time of peak power. Figure 13 shows the pinch diameter versus time overlaid with the x-ray power pulses for both (a) an annular and (b) a uniform fill implosion. Figure 13 also shows that the implosion times were the same in both cases and that the uniform fill and annular implosion had very similar pinch diameters at peak power.

The LFPHC data (see Figure 14) for the Ne:Ar uniform fill implosions show a marked improvement in implosion quality compared to the annular case represented in Figure 8. The imploding sheath has a noticeable curvature i.e. an hourglass-shape, [10] which results in the pinch occurring about 1 cm downstream of the nozzle and then zippering in both directions; this is akin to the pinch phase of a dense plasma focus. The R-T instabilities have wavelengths of 0.5 to 2.0 mm with amplitudes of 1 mm or less. These improvements are consistent with the predictions in References 7 and 10.

#### **IV. Krypton-Argon Admixture Annular and Uniform Fill Implosions**

We chose Kr gas puffs to test the performance of uniform fill loads with higher atomic numbers. For the Kr:Ar admixtures, the mixture ratio of argon was increased to 50% , i.e. the number of Ar atoms was equal to the number of Kr atoms, to attempt to keep the number of argon emitters in the same range as in the Ne:Ar experiments. The Kr:Ar admixtures showed a large difference between the annular and uniform fill nozzles. Figure 15 depicts the measured currents and x-ray powers for (a) an annular implosion and (b) a uniform fill implosion. In Figure 15(a), we can see that the annular implosion has a peak

power similar to that of the annular Ne:Ar implosion of just under 1.4 TW, even though the Kr L-shell has a median photon energy of 1.85 keV compared to the 1.2 keV of the neon K-shell. However, this energy difference manifests itself in two observations different than in Figure 6. Firstly, the magnitude of the precursor is much smaller than with Ne:Ar; specifically, the precursor emits only a few percent of the total kilovolt emissions. Second, the pulsewidth of the kilovolt x-ray pulse is 10 ns which is shorter than the 18 ns for the Ne:Ar mix. The x-ray power pulse from the uniform fill load is even shorter. The calculated FWHM is 6 ns but the first peak has a width of 2 ns. These pulsewidths are comparable to those obtained with the high wire number arrays, although the x-ray powers are factors of two to three smaller than those of the wire arrays.[29,30]

The pre-cursor is still present with the Kr:Ar mix at lower photon energies. Figure 16(a) shows the radiated energy versus time, as measured by the bolometers, for the Kr:Ar and Ne:Ar uniform fill implosions. During the run-in phase, the radiated energies and powers are approximately the same. At stagnation, Figure 16(b) shows that the Kr:Ar mixture radiates  $10.0 \pm 1.5$  TW. For comparison, the Ne:Ar shots radiated about 3.5 TW. The run-in radiation from the Kr:Ar is emitted at lower photon energies, indicating a lower temperature plasma. This is evident in the fact that the PCDs filtered to measure 0.8 to 2 keV x-rays showed run-in radiation for Ne:Ar, but not for Kr:Ar. By contrast, the unfiltered bolometers are measuring about the same emitted energies during the run-in, hence we conclude that the emissions must be radiated at photon energies below 800 eV.

The time-resolved, kilo-electron-volt pinhole images in Figure 17 show that the uniform fill load produces a tighter, shorter lived pinched plasma than the annular implosions. The uniform fill implosions [an example is shown in Figure 17(b)] produce plasmas with axially-averaged diameters of  $1.4 \pm 0.2$  mm compared to the equivalent pinch diameters of  $2.1 \pm 0.1$  mm for the annular loads, as estimated from the time-integrated images. For the



uniform fill load, the intrinsic radiation time at a given axial location is less than the 3 ns interframe time of this SFPHC instrument. By comparison, the annular implosions had 6 ns intrinsic radiation times for a given axial location with an axial zipper time of 6 to 9 ns.

The LFPHC images,(Fig. 18) which were filtered with 4  $\mu\text{m}$  of Parylene\_N to make the imploding sheath more visible, show very little evidence of RT growth for the Kr:Ar uniform fill implosions. This thin, low atomic number filter transmits x-rays between 180 and 280 eV where the krypton radiates well during the implosion, remembering that no emissions are seen in the keV filtered detectors during the run-in. To ensure that the Kr:Ar was imploding at the same velocity as the Ne:Ar implosions, we analyzed radial lineouts which are plotted in Figure 19. The limb-brightening is evident in the frames at 63 and 65.5 ns and the radial motion of these features correspond to a 70 cm/ $\mu\text{s}$  velocity. Just prior to stagnation, the implosion curvature is evident, and any RT structure has long wavelengths (2 to 3 mm) with small amplitudes i.e. less than 1 mm. The final diameter of the Ar:Kr uniform fill loads was substantially smaller than that of the Ar:Ne experiments. This could largely be a consequence of the greater radiative cooling from krypton than neon. A case can also be made that the smaller implosion diameter of the Kr load may partially be due to inhibited RT instability growth. This inhibited growth may be a consequence of a plasma sheath that is broadened by current diffusing further into the plasma because of the higher resistivity and lower temperatures (greater on-axis radiative cooling rate) of the higher atomic number plasmas.

Arguments in support of this effect will be discussed in more detail in Section VI where we compare the results from the different implosions with two-dimensional and one-dimensional radiation-MHD calculations. Prior to this comparison, we present the spectral analyses that are used to infer the plasma densities and temperatures.

## V. Spectral Analyses

We have diagnosed the plasma conditions from our time-integrated spectra following the Collisional Radiative Equilibrium analysis technique described in Coulter *et al*[31] and Apruzese *et al*. [32] This technique involves self-consistently fitting the plasma size, emitted x-ray power and line ratios to simultaneously infer an electron temperature and ion density. This technique has been used to diagnose many Z-pinch experiments, and it can be very useful as well at identifying gradients within the pinch and overall trends in pinch properties especially when coupled with the use of dopants or mixtures [33,34] and used with time-resolved data [35]. Furthermore, in these experiments we had the high resolution Johann time-resolved spectrometer and Wong *et al* [14] have analyzed this data to determine time-resolved electron densities and temperatures by Stark broadening and the slope of the free-bound continua.

Figure 20 shows an example of the time-integrated spectrum from an annular Ne:Ar implosion. The neon K-shell spectrum is dominated by the hydrogen-like lines and the free-bound continua. The neon Lyman-alpha to helium-alpha ratio is 3.5. The argon spectrum has a stronger Helium-alpha than Lyman-alpha line. From this spectrawe would infer average electron temperatures of  $450\pm 50$  eV during the emission time of the neon lines,  $500\pm 50$  eV during the emission time of free-bound continua and  $1800\pm 100$  eV in the region of plasma where the argon K-shell lines are emitted. The Johann spectrometer data gave an inferred peak electron temperature of  $1250\pm 180$  eV from the slope of the neon recombination radiation at the time of peak x-ray power[ 13]. For the uniform fill nozzle, we measured higher average electron temperatures:  $600\pm 50$  eV from the neon lines;  $600\pm 50$  eV from the free bound continua and  $1900\pm 100$  eV from the Ar lines. The Johann spectrometer also indicated that a higher peak electron temperature of  $1600\pm 240$  eV.[13] was responsible for the neon continuum emissions at the time of peak

power. In Table 3, we tabulate the measured temperatures, densities and K-shell masses for all the shots discussed in this paper. Clearly there are severe temperature gradients present in these plasmas and large temperature excursions in time as indicated by the widely varying temperature measurements. Similar gradients and time variations are also routinely observed in wire array experiments.

Figure 21 shows an example of an Kr:Ar spectrum. The Kr L-shell spectrum shows the various 3-2 and 4-2 transitions from Ne- and F-like krypton. The argon helium-alpha line is the most intense with the Lyman-alpha being only 5% as strong as the helium-alpha line. This line ratio would indicate an electron temperature of only  $1000 \pm 50$  eV in support of the radiation cooling arguments made above.

From Table 3, we can see that: the uniform fill loads produce a higher density, higher temperature plasma than annular loads even though they had the same predicted and measured implosion times; the uniform fill loads with Ne:Ar achieve approximately 100% of the neon mass contributing to the K-shell emissions compared to only a 60% contribution for the annular loads..

## VI. Discussion.

As stated in the introduction, gas puffs have unique flow characteristics, i.e. different levels of axial non-uniformity that make it difficult to separate effects that are produced by axial non-uniformities from those produced by instabilities. Nevertheless, there has been significant recent two-dimensional theoretical development that ties in with many of the observations stated above. The following discussion on the results of one- and two-dimensional modeling on x-ray output is given to help quantify the extent to which imploding annular fill gas puffs deviate from ideal one-dimensional implosion behavior. It should be noted that the two-dimensional calculations are themselves somewhat idealized

since the initial gas flow conditions are not measured directly to be used as an input into the calculations, rather the initial conditions are approximated, for example, to assess the effects of curvature.

#### **A. Snowplow and curvature RT mitigation.**

The mitigation of the RT growth that is evident in the time-resolved pinhole images of the uniform fill implosions was expected by theories put forward in references 6 through 11, and reference 36. Basically, as the sheath implodes the mass accretion reduces the growth rate, especially of the longer wavelengths, by preventing the rapid mass loss out of the bubble. Roderick *et al* [36] have compared annular and uniform fill loads for Saturn using pure Kr. They concluded in their paper that RT instabilities are seeded by the white noise spectrum of modes that are naturally present in the two-dimensional expansion of gas from a nozzle. Furthermore, their calculations indicated that the mass accretion, which is enhanced in the uniform fill nozzle case, reduces the RT growth rates.

As reported by Douglas *et al*, [10] snowplowing is not the only mitigation mechanism at work in the uniform fill cases. The mass flow associated with the presence of the sheath curvature (the 'hourglass' shape in Figures 14 and 18) further reduces RT growth. An example of this process is demonstrated in Figure 23 where the iso-density contours are shown for two uniform fill krypton implosions, as calculated by the 2D MHD code, MACH2, using a simple emission model, [37]. The calculation in Figure 23(a), has an initial axial configuration that is a right-cylinder. The other calculation, Fig. 23(b), had the same mass but it had an initial axial profile that had an imposed hourglass shape with a 2.0-cm outer radius at the waist and a 2.25-cm outer radius at the anode and cathode. The hourglass shape results in mass flow from the axial midpoint to each end as the sheath implodes. This mass-flow RT mitigation has been discussed in reference 10 and it has

been shown, as in Figure 23, to advect the instabilities to the electrodes, so reducing their effective growth rates. Axial velocity shear as an RT stabilizing mechanism has also been studied in more detail.[38] Use of this mechanism was demonstrated to stabilize an implosion from large radius.[39]

In the calculations by Douglas *et al* and in those shown in Figure 23, the arc that produces the gas flow is imposed as an initial condition. It is believed that in the experiment that the hour-glass shape results from the expansion fan and axial mass-per-unit-length variations that are present with these uniform fill nozzles. Although the hour-glass shape results in a long-wavelength mode (zipper), the RT stabilization does produce a locally more uniform implosion.

#### **B. Scaling of RT wavelength and amplitude with atomic number.**

In addition to the stabilization mechanisms discussed above, clear variations in instability growth have been observed for the different atomic mixtures used in these experiments. This is most clear with the Ne:Ar and Kr:Ar uniform fills where the instability growth is not too severe even with the lowest atomic numbers. Two-dimensional radiation MHD calculations presented in Figure 24 indicate that increased atomic number implosions can have improved stability. The three iso-density contour plots shown in Figure 24 are from calculations of neon, argon and krypton uniform fill implosions with identical mass loadings, initial temperatures of 0.5 eV and 5% random density perturbations. These plots are generated at the same time during the implosion. From Figure 24, it is apparent that the higher atomic number gases develop lower amplitude, longer wavelength instabilities. This is a result of two effects. Firstly, the equation of state of the higher atomic number gases allows for more free electrons to be produced. Secondly, the radiative cooling rates are larger for the higher atomic number elements so they imploded at lower sheath

temperatures. The calculations indicate that the temperatures are about 50% lower, on average, in the Kr case versus the Ne case in Figure 24. The lower temperatures of the sheath for krypton is consistent with the measurement of kilovolt emissions during the implosion of the neon gas puffs versus the lower energy emissions seen with the krypton gas puffs. The lower electron temperatures ( $T_e$ ) in conjunction with the higher Z-bars ( $Z$ ) increase the resistivity of the imploding sheath for the higher atomic numbers, which will in turn increase the skin depth, noting that the skin depth scales as  $Z^{0.5} T_e^{-0.75}$ . As discussed in reference 38, higher resistivities lead to more field diffusion, especially with uniform fill loads, which have no defined shell thickness. The wider skin depth will tend to reduce the growth rates of the shorter wavelengths. Since the shorter wavelengths grow faster, their reduction significantly improves stability of the implosion. For thin annular loads, where the shell thickness is less than the skin depth, such effects may be minimized. In a future paper, calculations will be presented which will begin to quantify the RT effects observed in the implosions discussed in this paper, however, it should be noted that the calculations suggest that argon and krypton implosions are similar and both more stable than neon implosions. This is consistent with the pulsewidth trend shown in Figure 22. On other Z-pinches at lower currents, pre-ionization and breakdown differences may give other trends.

### **C. Effects of one- and two-dimensional behavior on the x-ray output.**

As discussed in the introduction, the quantification of the effects on x-ray output of asymmetries and instabilities in Z-pinch implosions are still active areas of investigation. Experiments have shown and calculations suggest that implosion quality has a decisive effect on the total x-ray and kilo-electron-volt x-ray powers.[6,26,35] While the corresponding yields may be less affected for low Z materials like neon, the presence of asymmetries can significantly modify them as well, as demonstrated in the zippering and non-zippering implosions described by Deeney, *et al.*[21] The size of the effects on radiation of implosion asymmetries and instabilities are difficult to assess because these mechanisms are predicted to localize the state of the plasma so that each plasma region has different radiation

characteristics. For example, when an RT induced spike region of the pinch has an order of magnitude larger density than that of a bubble region, it is also calculated to have a much lower temperature than the bubble region.

In this section, we compare the experimental data with a sequence of four one-dimensional radiation MHD calculations. These were originally performed to assess the degree to which these experiments were influenced by the load parameters that were chosen, e.g. initial mass, mass distribution, and mixture composition. However, these comparisons also make it apparent that the non-one-dimensional behavior of the implosions largely controlled some of the experimental results, and that these comparisons thereby allow one to begin to assess the degree to which the experiments were influenced by the deviations from one-dimensionality. In contrast to the experiments, the initial fill profiles in the calculations are truly uniform and the shell profiles were taken to have uniform density between 1.25 cm outer radius and 1.1 cm inner radius. In addition, in the shell calculations, there is an exponential fall-off by a factor of 20 in density from 1.1 cm radius to 0.9 cm radius. These one-dimensional code calculations have been shown to fairly accurately replicate the yields observed in high wire number aluminum array implosions.[39,40] They also reasonably reproduce the total and K-shell powers as well as the qualitative features of density and temperature gradients detected in the high wire number Saturn aluminum experiments.

In Table 4, the results from a sequence of four gas puff calculations are shown. Listed are the total powers, the 1-2 keV and  $> 2$  keV x-ray powers plus associated yields, the pinch diameters, temperatures and densities; and the x-ray pulsewidths. The temperatures and densities are mass averaged over the argon K-shell emission region and time averaged over the  $> 2$  keV FWHM pulse duration of the emission. The first of these calculations corresponds to the experimental 2.5-cm-diameter annular implosions of shots 2009 and 2110, which were 90:10 Ne:Ar mixtures with masses of approximately 300  $\mu\text{g}/\text{cm}$  each. The second calculation was taken to be a 2.5 cm diameter uniform

fill load of 300  $\mu\text{g}/\text{cm}$  consisting of a 90:10 Ne:Ar mixture. Cases 3 and 4 are uniform fill implosions that correspond with the experimental 4.5-cm diameter shots 2112 (90:10 mixture) and 2113 (80:20 mixture), respectively. The mass of each of these shots is approximately 200  $\mu\text{g}/\text{cm}$ . For the three configurations involving Ne:Ar mixtures that were calculated, the results from the relevant experimental shots are listed in Table 4, as well. The results for shots 2009 and 2110 are shown as a single average.

The total calculated power from Case 1 was 24 TW/cm, which included 19 TW/cm of  $> 1$  keV x rays. The calculated total x-ray energy emitted  $> 1$  keV was 63 kJ. These x-ray powers and energies represent what one should reasonably expect from a truly one-dimensional annular shell implosion. For example, the high wire number Saturn aluminum experiments, against which a similar set of calculations were benchmarked, produced 70 kJ of K-shell emission and 20 TW/cm of peak x-ray power from a 2.4 cm diameter aluminum, 300  $\mu\text{g}/\text{cm}$ , wire array. Given that larger pinch sizes and lower total powers (2.4 TW/cm) were observed in the annular gas puff implosions than in the one-dimensional calculations or in the large wire number, highly symmetric aluminum array experiments, we conclude that the present experiments clearly indicate the non-one-dimensional nature of these implosions. Although the powers decreased, the greater than 1 keV x-ray yield still remained close to the 63 kJ calculated yield.

Table 4 shows that the Case 2 uniform-fill distribution produces similar results to the Case 1 annular load. Thus, these results are also indicative of the lack of one-dimensionality implosion behavior in the experiments. The primary differences between Case 1 and Case 2 are that uniform-fill loads produce hotter and less dense plasmas at stagnation. This results in substantially more  $> 1$  keV photons produced by the Case 2 distribution. From a basic fluid dynamics standpoint, conservation of momentum requires that the uniform fill distribution internalize about 22 percent of the  $\text{J} \times \text{B}$  work during the run-in phase for an initial to final radius compression ratio of 10:1. Relative to the annular



profile, the effect is to produce a hotter, lower density pinch during the run-in phase that then raises the adiabat along which the pinch travels prior to stagnation. From a temperature point of view alone this would give uniform fill loads a potential advantage for producing higher energy photons.

The zippering effects in the experiment can approximately be accounted for assuming that the calculated FWHM of the radiation pulse should actually be compared to the intrinsic locally measured radiation time of 6 ns instead of the 17.2 ns listed in Table 4 for shots 2009 and 2110. In this case, the localized radiated pulse FWHM is only about a factor of two larger than the calculated pulsewidth, and the local power would be 6.9 TW/cm. This higher power would lead to a higher estimated localized ion density of  $13.5 \times 10^{19} \text{ cm}^{-3}$ . These modified numbers move the local experimental pinch dynamics significantly in the direction of the 1D results. However, because of the nonlinear dynamics of the machine-to-load energy coupling, it is difficult to tell from these locally estimated numbers whether zippering is the predominant mechanism responsible for the remaining deviations from the one-dimensionally predicted x-ray performance. Such an evaluation would be best made with a 2D code calculation that is first benchmarked in 1D against the high wire number aluminum array experiments before the inclusion of a zipper.

At present, for fill loads, there is no experimental counterpart to the high-wire-number, highly symmetric, array experiments that would allow one to reasonably assess the degree to which 1D calculations can be used to predict the radiation performance of these loads. The reason for this deficiency is that for gas puffs the initial gas distribution is inherently axially non-uniform. It is difficult enough to estimate the amount of mass in a gas puff pinch *let alone* control and measure with precision the initial gas distribution. The mass is usually inferred indirectly using circuit models and implosion time measurements. Because of this inherent lack of knowledge of the initial conditions it is difficult to design gas puff experiments that would allow one to directly benchmark 1-D calculations against experimental measurements. One must attempt instead to establish a benchmark using high-wire-number aluminum array experiments. Thus, we have used the same transport coefficient

enhancements in the uniform fill calculations as were employed in the annular fill calculations, which were benchmarked against large-wire-number aluminum array experiments.

One generally expects 1D calculations to predict pinch radii that are smaller than or equal to experimental pinch radii and to also predict powers that are larger than the experimental powers. The powers are expected to be nearly equal only for experimental conditions that are close to 1D. At first glance, a comparison of Case 3 with shot 2112's results (see Table 4) reveals that this power relationship is nearly true. However, if one takes into account that the intrinsic radiation time for the experimental fill loads is 3 ns, then one would find that the localized total radiative powers per centimeter are 4-5 times larger than the 1.75 TW/cm values listed in Table 4. These powers/cm are substantially larger than the calculated values. This makes sense, since it has been found that the use of viscosity and heat conduction enhancements provides a way to model the effects of 3-D wire gap spacing. Spacings can produce azimuthal asymmetries and they can lead to the generation of plasma arriving on axis before the bulk of the plasma stagnates. These effects are not as likely to be present in gas puff fill experiments. The lower calculated powers are also consistent with the smaller temperatures and larger stagnation densities present in the experiments.

Until a more direct uniform fill benchmark experiment is performed at relatively small radius, so that RT effects are ostensibly minimal, it is difficult to determine how accurately a 1D calculation models the local dynamics of a non-uniform fill pinch implosion. A substantially different dynamics takes place in the uniform as opposed to the annular loads, since, a significant fraction of the  $J \times B$  work is internalized in the uniform loads during run-in. Therefore, until a benchmark is established, it may be premature to definitely conclude that local powers seen with the experimental fill loads represent significant deviations from 1D behavior because of non-uniform gas distributions or instability growth.

In spite of some yield discrepancies, the present model does agree with experimental trends. For example, the calculations exhibit the same trends in pinch sizes, temperatures, and densities as seen experimentally, and they show these quantities should not significantly depend on whether the uniform fill load has a 90:10 mixture or an 80:20 Ne:Ar mixture. Likewise, the 1-D calculations are in accord with the experimental trends that the 1-2 keV yield should decrease and the  $> 2$  keV yield should increase as the mixture is changed from 90:10 to an 80:20 Ne:Ar mixture. This is expected behavior because argon is a better radiator of  $> 2$  keV photons than neon.

## V. Conclusions and Future Work.

The calculations that are described in this paper were carried out in correspondence with the experiments described in this paper. However they primarily make it clear that gas-puff Z pinch implosions are full-fledged two (and possibly three) dimensional radiation magneto-hydrodynamic fluid problems. In the case of the annular flows, the Z-pinch discharge is initiated in a pre-existing three-dimensional gas flow, and the improvement in the x-ray performance of the pinch as the nozzles are tilted inwards demonstrates the inherent three-dimensional character of the breakdown process. RT instability development is seeded in multiple ways by the three-dimensional flow, and the implosion is highly non-uniform along the pinch axis, transitioning from a shell implosion near the nozzles to more of a snowplow implosion away from the nozzles. This mixed conglomeration of implosion dynamics leads to the strong zippering effects seen in the axial x-ray emissions and to more axial non-uniformities in the kilovolt pinhole pictures than are explainable solely in terms of RT bubbles and spikes. Thus, in contrasting annular with more uniform-fill implosions, one can expect, for a number of reasons, to find the sizable improvements in the pinch's implosion uniformity and x-ray performance that were described in this paper.

From the totality of the data and analyses presented above, it can be concluded that:

- 1) for the Ne:Ar and Kr:Ar admixtures, the radiated kilo-electron-volt energies and powers are higher for the uniform fills rather than the annular gas puffs
- 2) for the Ne:Ar admixtures, the uniform fill loads produce slightly denser and hotter pinches;
- 3) the total radiative power increased with the atomic number of the gases in the gas puff;
- 4) the uniform fill profiles, that are generated by the nozzles tested in this experiment, appear to mitigate(i.e. reduce the amplitude) Rayleigh-Taylor instabilities; and
- 5) this mitigation of Rayleigh-Taylor instabilities appears to increase with the atomic number of the gas puff load.

By an appropriate mix of detailed one- and two-dimensional calculations, we have examined the roles of improved implosion stability, improved initial conditions and the effects of the radiative and plasma properties of the gas mixtures employed. This leads to the general conclusion, that uniform fill gas puff loads can result in implosions that are more one-, or at least two-dimensional in nature. As a consequence they radiate higher x-ray powers and in some cases more x-ray energy than the approximately annular gas puffs that were employed. This is similar to the trends seen in the improvements with wire arrays. In order to make future comparisons easier and to extend them to a wider range of diameters, improved annular profile and uniform profile gas injection systems should be used.[40]

We wish to acknowledge beneficial discussions with M.G. Haines of Imperial College; and D.L. Peterson of Los Alamos National Laboratory. We also would like to thank the Saturn crew for their outstanding technical support.

## References.

1. N. R. Pereira and J. Davis, J. Appl. Phys. 64, R1 (1988).
2. M.K. Matzen, Physics of Plasmas 4, 1519, (1997).
3. C. Deeney, C.A. Coverdale, M.R. Douglas, *et al*, Phys Plasmas 6, 2081, (1999).
4. T.W. Hussey and N.F. Roderick, Phys. Fluids 24, 1384, (1981).
5. T.W. Hussey, N.F. Roderick, U. Shumlak, R.B. Spielman and C. Deeney, Phys. Plasmas 2, 2055, (1995).
6. R.B. Baksht, I.M. Datso, A.A. Kim, A. Yu. Labetskii, S.V. Loginov, V.I. Oreshkin, A.G. Russkikh, A.V. Fedunin, & A.V. Shislov, Plasma Physics Reports 21, 907, (1995).
7. S.M. Golfsberg and A.L. Velikovich, Phys. Fluids B 5, 1164, (1993).
8. F.L. Cochran, J. Davis and A.L. Velikovich, Phys. Plasmas 2, 2765, (1995).
9. A.L. Velikovich, F.L. Cochran and J. Davis, Phys. Rev. Lett 77, 853, (1996).
10. M.R. Douglas, C. Deeney and N.F. Roderick, Phys. Rev. Lett. 75, 3285, (1995).
11. J.H. Hammer, J.L. Eddleman, P.T. Springer, M. Tabak, A. Toor, K.L. Wong, C. Deeney, R. Humphreys, T.J. Nash, T.W.L. Sanford, R.B. Spielman, & J.S. DeGroot, Phys. Plasmas 3, 2063, (1996).
12. A.G. Rousskikh *et al*, Phys Plasmas Reports 25, 527, (1999).
13. R.B. Spielman *et al*, Bull. Am. Phys. Soc. 40, 1845, (1995).
14. K.L. Wong, P.T. Springer, J.H. Hammer, C.A. Iglesias, A.L. Osterheld, M.E. Foord, H.C. Bruns, J.A. Emig, and C. Deeney, Spectroscopic Characterization of an Argon-Neon Z-Pinch Plasma at Stagnation, to be published in Phys. Rev. Lett.
15. R.B. Spielman, R.J. Dukart, D.L. Hanson, B.A. Hammel, W.W. Hsing, M.K. Matzen & J.L. Porter, in Proceedings of the 2nd International Conference on Dense Z-Pinches, Laguna Beach, CA, 1989, edited by N.R. Pereira, J. Davis, and N. Rostoker (AIP, New York, 1989), p3.

16. S. Wong, P. Smiley, T. Sheridan, J. Levine, and V. Buck, *Rev. Sci. Instrum.* 57, 1684, (1986).
17. R.S. Smith, W.O. Doggett, I. Roth, and C. Stallings, *Appl. Phys. Lett.* 43, 524, (1982).
18. R.S. Smith and W.O. Doggett, *Appl. Phys. Lett.* 46, 1128, (1985).
19. W.W. Hsing & J.L. Porter, *Appl. Phys. Lett.* 50, 1572, (1987).
20. T.W. Hussey, M.K. Matzen, and N.F. Roderick, *J. Appl. Phys.* 58, 2677, (1986).
21. C. Deeney, P.D. LePell, F.L. Cochran, M.C. Coulter, K.G. Whitney & J. Davis, *Phys. Fluids* 5(3), 992, (1993).
22. B.V. Weber and S.F. Fulghum, *Rev. Sci. Instrum.* 68, 1227, (1997).
23. R.B. Spielman, L.E. Ruggles, R.E. Pepping, S.P. Breeze, J.S. McGurn, and K.W. Struve, *Rev. Sci. Instrum.* 68, 782, (1997).
24. R.B. Spielman, C. Deeney, J. McGurn, *et al*, *Rev. Sci. Instrum.* 70, 651 (1999).
25. T. Nash, C. Deeney, P.D. LePell, and R. Prasad, *Rev. Sci. Instrum.* 61, 2807, (1990).
26. D.L. Peterson, R.L. Bowers, K.D. McLenithan, C. Deeney, G.A. Chandler, R.B. Spielman, and M.K. Matzen, *Phys. Plasmas* 5, 3302 (1998).
27. J.W. Thornhill, K.G. Whitney, C. Deeney, and P.D. LePell, *Phys. Plasmas* 1, 321, (1994).
28. K.G. Whitney, J.W. Thornhill, P.E. Pulsifer, *et al*, *Phys. Rev. E* 56, 3540, (1997).
29. T.W.L. Sanford, G.O. Allshouse, B.M. Marder, *et al*, *Phys. Rev. Lett.* 77, 5063, (1996).
30. C. Deeney, T.J. Nash, R.B. Spielman, *et al*, *Phys. Rev. E* 56, 5945, (1997).
31. M.C. Coulter, K.G. Whitney and J.W. Thornhill, *J. Quant. Spectrosc. Radiat. Transfer* 44, 443 (1990).

32. J. P. Apruzese, K. G. Whitney, J. Davis, and P. C. Kepple, J. Quant. Spectrosc. Radiat. Transfer., 57, 41, (1997).
33. C. Deeney, P.D. LePell, B.H. Failor, S.L. Wong, J.P. Apruzese, K.G. Whitney, J.W. Thornhill, J. Davis, E. Yadlowsky, R.C. Hazelton, J.J. Moschella, T.J. Nash & N. Loter, Phys. Rev. E 51 (5-B), 4823, (1995).
34. J.P. Apruzese, J.W. Thornhill, K.G. Whitney, *et al.*, IEEE Trans. Plasma Sci. 26, 1185 (1998).
35. T.W.L. Sanford, T. J. Nash, R. C. Mock, *et. al.*, Rev. Sci. Instrum, 68, 852 (1997).
36. N.F. Roderick, R.E. Peterkin, T.W. Hussey, R.B. Spielman, M.R. Douglas, and C. Deeney, Phys. Plasmas 5, 1477, (1998).
37. R.E. Peterkin, J.H. Degnan, T.W. Hussey, N.F. Roderick, and P.J. Turchi, IEEE Trans. Plasma Sci., PS-21, 552, (1993).
38. N.F. Roderick and T.W. Hussey, J. Appl. Phys 56, 1387, (1984).
39. U. Shumlack and N. F. Roderick, Phys. Plasmas 5, 2384 (1998).
40. A. L. Velikovich, F. L. Cochran, J. Davis, and Y. Chong, Phys. Plasmas 5, 3377 (1998).

Table 1. The gas puff experimental parameters.

Shot	Geom.	Nozzle Diam. (cm)	Plenum Press. (torr)	Flow Delay ( $\mu$ s)	Neon (%)	Krypton (%)	Argon (%)
2108	A	2.5	4400	500	90	N.A.	10
2109	A	2.5	4400	500	90	N.A.	10
2110	A	2.5	4400	500	95	N.A.	10
2112	U	4.5	4000	600	90	N.A.	10
2113	U	4.5	4500	600	80	N.A.	20
2114	U	4.5	4500	600	80	N.A.	20
2115	U	4.5	1580	650	N.A.	50	50
2118	U	4.5	1500	650	N.A.	50	50
2155	U	2.5	1200	550	N.A.	50	50
2156	U	2.5	1200	550	N.A.	50	50

Table 2. X-ray yields, powers and plasma diameters.

Shot	Kilovolt FWHM (ns)	>800eV Pinch Diam. (cm)	>200eV Pinch Diam. (mm)	Total Yield (kJ)	Total Power (TW)	1-2keV Yield (kJ)	1-2keV Power (TW)	>2 keV Yield (kJ)	>2 keV Power (TW)
2109	16.0	2.6 $\pm$ 0.2	3.4 $\pm$ 0.1	300 $\pm$ 40	5.5 $\pm$ 0.5	35	1.2	7	0.5
2110	18.4	2.8 $\pm$ 0.2	3.5 $\pm$ 0.1	290 $\pm$ 40	4.0 $\pm$ 0.5	50	1.3	8	0.4
2113	13.6	2.5 $\pm$ 0.2	3.5 $\pm$ 0.1	180 $\pm$ 30	3.5 $\pm$ 0.5	56	2.2	25	1.6
2114	14.4	2.6 $\pm$ 0.2	3.2 $\pm$ 0.1	180 $\pm$ 30	3.5 $\pm$ 0.5	50	2.0	24	1.5
2115	6.0	1.0 $\pm$ 0.2	2.2 $\pm$ 0.1	230 $\pm$ 30	10.0 $\pm$ 2.0	15	2.0	2	N/A
2118	6.4	1.4 $\pm$ 0.2	2.4 $\pm$ 0.1	320 $\pm$ 40	13.0 $\pm$ 2.0	16	1.9	2	N/A
2155	10.0	2.3 $\pm$ 0.2	3.4 $\pm$ 0.1	230 $\pm$ 30	6.5 $\pm$ 0.5	11	0.9	N/A	N/A
2156	10.0	2.3 $\pm$ 0.2	3.5 $\pm$ 0.1	260 $\pm$ 30	7.8 $\pm$ 0.5	20	1.4	N/A	N/A

Table 3. X-ray spectral analyses.

Shot	Neon F-B Te (eV)	Neon B-B Te (eV)	Neon Ni ( $10^{19}$ cm $^{-3}$ )	Neon mk ( $\mu$ g/cm)	Argon B-B Te (eV)	Argon Ni ( $10^{19}$ cm $^{-3}$ )	Argon mk ( $\mu$ g/cm)	IT Ni ( $10^{19}$ cm $^{-3}$ )
2109	450 $\pm$ 50	375 $\pm$ 25	8 $\pm$ 2	140 $\pm$ 30	1800 $\pm$ 100	0.5 $\pm$ 0.1	7 $\pm$ 2	8
2110	450 $\pm$ 50	450 $\pm$ 50	7 $\pm$ 2	160 $\pm$ 50	1800 $\pm$ 100	0.4 $\pm$ 0.1	9 $\pm$ 2	8
2113	600 $\pm$ 100	600 $\pm$ 100	9 $\pm$ 3	160 $\pm$ 40	1900 $\pm$ 100	1.0 $\pm$ 0.2	14 $\pm$ 3	12
2114	600 $\pm$ 100	500 $\pm$ 100	10 $\pm$ 3	150 $\pm$ 40	1900 $\pm$ 100	1.0 $\pm$ 0.2	16 $\pm$ 4	12
2115	N.A.	N.A.	N.A.	N.A.	1000 $\pm$ 50	1.6 $\pm$ 0.3	6 $\pm$ 2	N.A.



Table 4. One-dimensional calculation predicted yields and powers.

Case or Shot	Nozzle Diam. (cm)	Type	Mass ( $\mu\text{g/cm}$ )	Mix. (Ne:Ar)	Total Yield (kJ)	Total Power (TW)	1-2 keV Yield (kJ)	1-2 keV Power (TW)	> 2 keV Yield (kJ)	> 2 keV Power (TW)	Pinch Diam. (mm)	kilovolt FWHM (ns)	<Te> (eV)	<Ni> ( $10^{19} \text{ cm}^{-3}$ )
1	2.5	A	300	90:10	80	48	44	26	18.8	12	0.09	2.5	1600	100
2110	2.5	A	300	90:10	295	4.8	50.5	1.5	7.5	0.45	0.35	17.2	1800	8
2	2.5	U	300	90:10	140	40	68	20	26	12.6	0.11	2	1930	77
3	2.5	U	300	80:20	160	46	60	20	40	20	0.11	2	1755	73
4	4.5	U	600	80:20	40	3.8	11.4	1	12.4	2.4	0.40	5.2	2650	3
2112	4.5	U	600	80:20	180	3.5	63.5	2.6	18.5	1.5	0.35	14	1900	10
5	4.5	U	200	90:10	32	2.4	12.6	1	6.6	1.2	0.42	5.4	2840	3

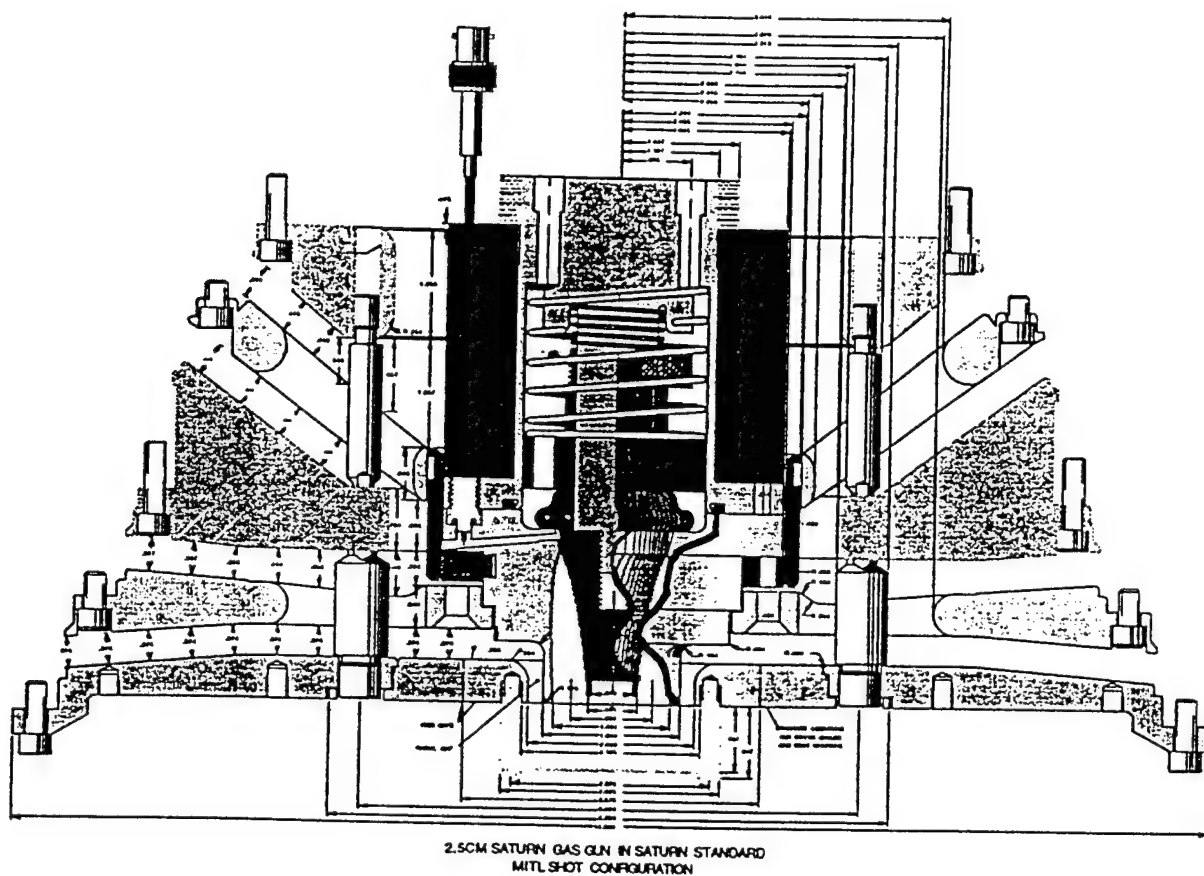


Figure 1. A schematic of the four magnetically insulated transmission lines(MITL) coupled through a double post-hole convolute to a 2.5-cm gas puff load. The anode-cathode length is 2 cm and the anode is formed from a wire mesh.

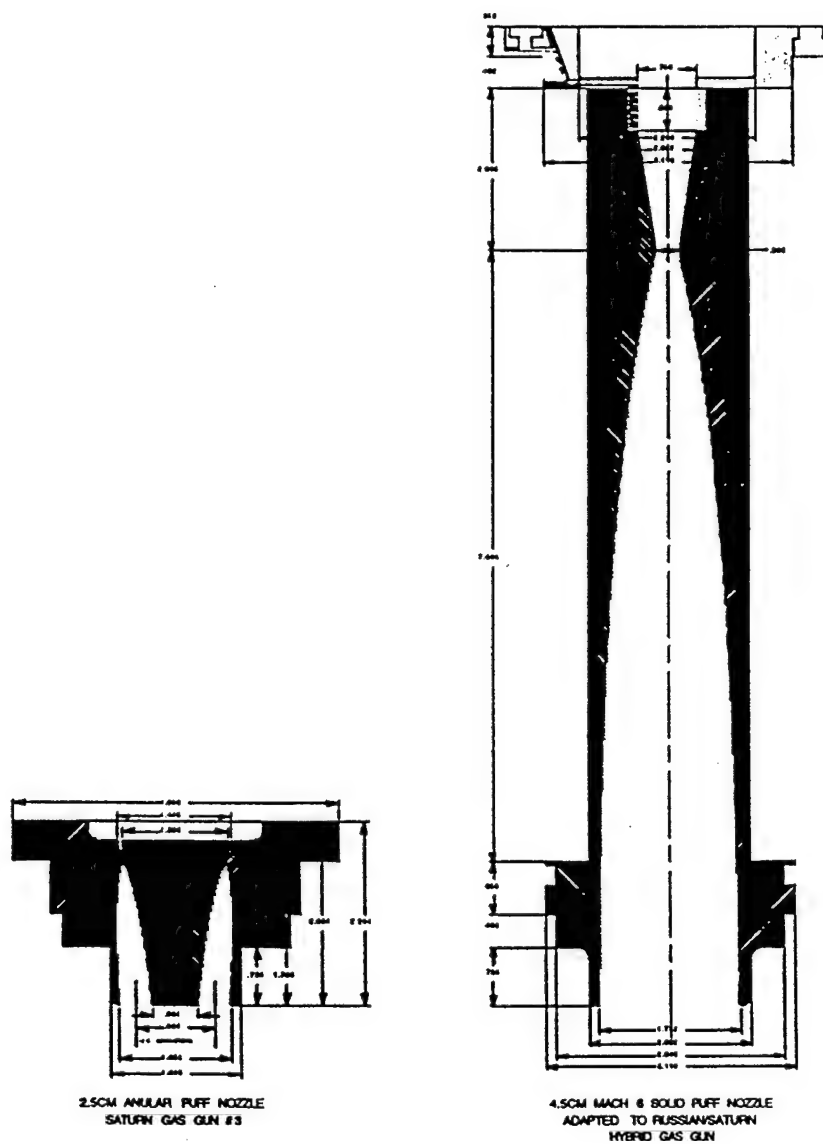


Figure 2. A comparison of the physical dimensions of (a) a 2.5-cm annular nozzle and (b) a 4.5-cm outer diameter uniform fill nozzle.

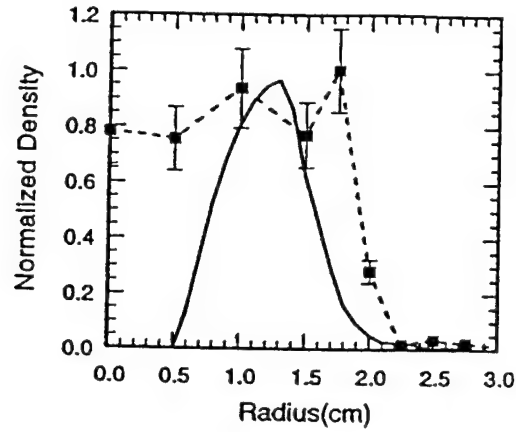


Figure 3. The measured normalized density versus radius profile for a 2.5 cm annular nozzle (solid) and a 4.5-cm diameter uniform fill nozzle (dashed) show that the uniform fill nozzle produces a more radially uniform profile. The error bars are shown for the uniform fill nozzle, and are comparable for the annular nozzle.

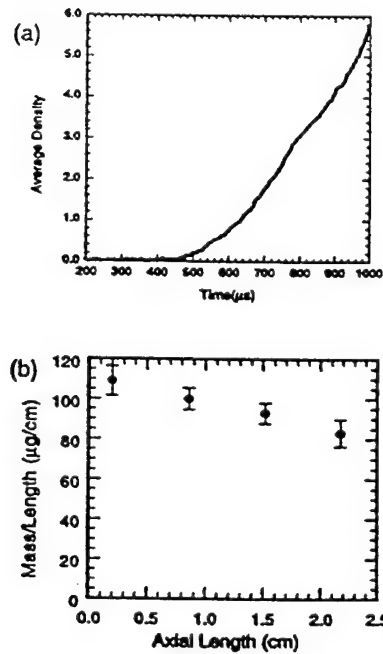


Figure 4. (a) The average density versus time is shown as measured by a heterodyne interferometer at the output of the uniform fill nozzle. The  $t=0$  corresponds to the breakdown of the trigger-pin. (b) The slow risetime of the gas flow results in a gradient in the mass-per-unit-length along the  $z$ -axis. In this plot, the location at  $z=0$  corresponds to the nozzle exit.

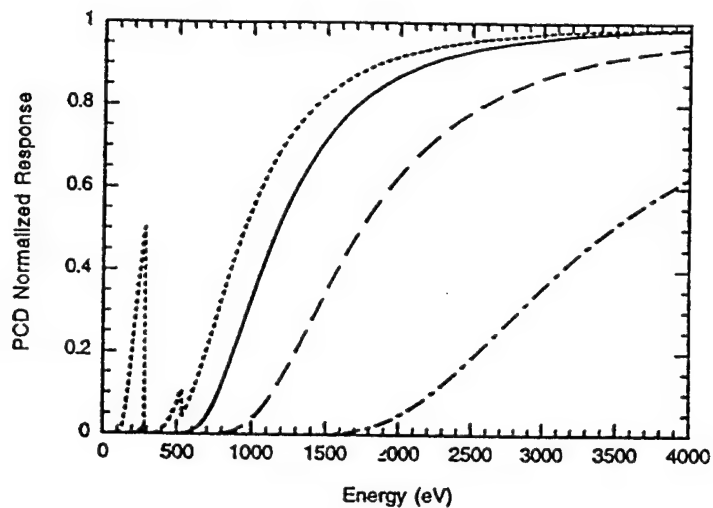


Figure 5. The normalized responses of the filtered diamond photoconducting detectors. The filters are 4  $\mu\text{m}$  of kimfol (dotted), 8  $\mu\text{m}$  of beryllium plus 1  $\mu\text{m}$  of Parylene\_N (solid), 8.5  $\mu\text{m}$  of kapton (dashed), and 50  $\mu\text{m}$  of kapton (dash-dot).

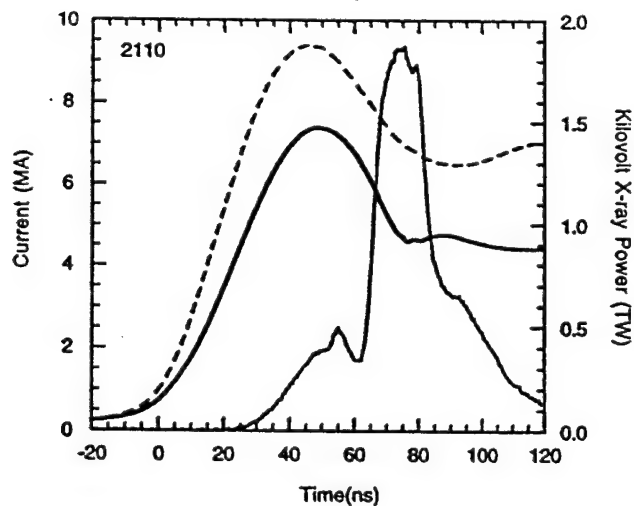


Figure 6. An overlay of the measured load current (thick solid), total MITL current (dashed), and the kilo-electron-volt x-ray power (thin solid) for shot 2110, a 2.5-cm diameter annular Ne:Ar implosion.

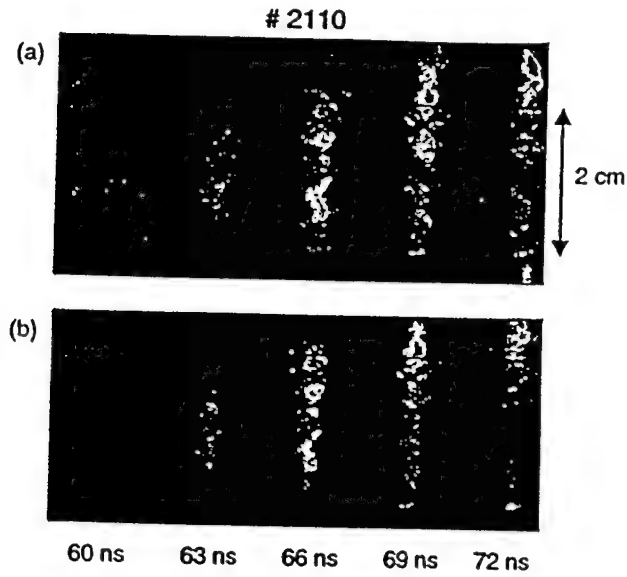


Figure 7. Time-resolved images of a Ne-Ar annular gas puff implosion, shot 2110, measured in two different x-ray energy ranges: (a)  $> 800$  eV, and (b)  $> 2000$  eV. The interframe time is 3 ns and the image durations are 2 ns.

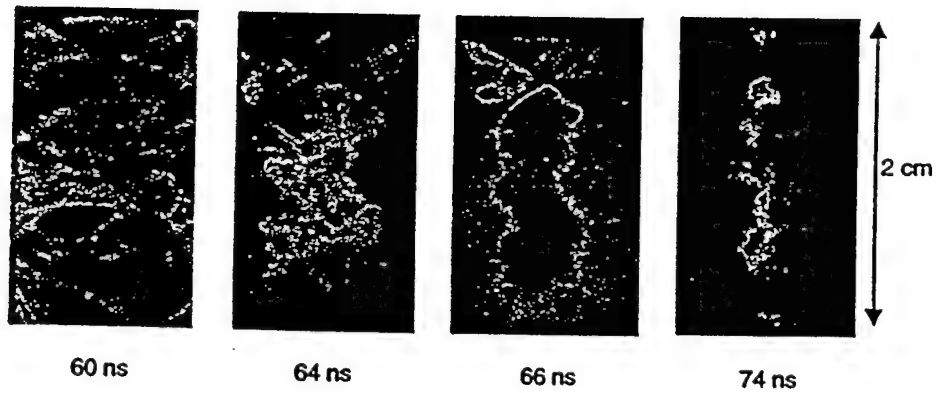


Figure 8. Four images of neon annular gas puff implosion (s2210) recorded with 100-ps gate pulses for x-ray emissions greater than 800 eV.

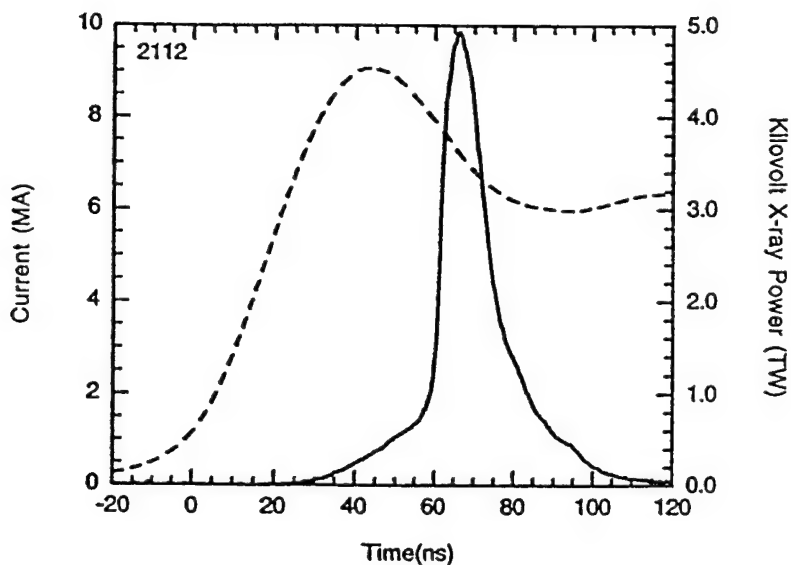


Figure 9. The measured total MITL current and the kilo-electron-volt x-ray power for a neon uniform fill implosion.

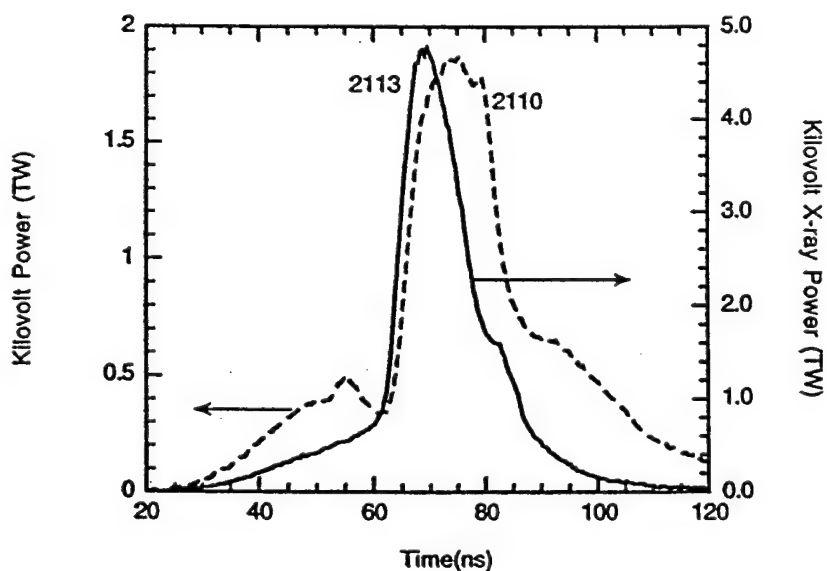


Figure 10. A comparison of the kilo-electron-volt powers measured on an annular shot (dashed curve) and a uniform fill shot (solid curve). The peak power, the FWHM and the details of the emissions during the run-in phase are very different than those shown for the annular implosion.

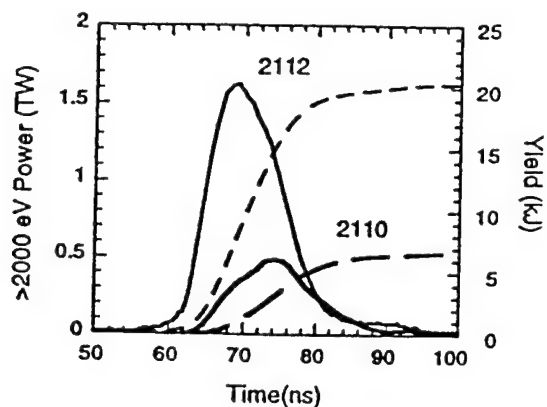


Figure 11. The measured x-ray powers and yields above 2 keV for a uniform fill and an annular shot, both with Ne-Ar mixtures. This spectral range corresponds to the argon K-shell emissions plus some neon K-shell recombination continuum. The  $> 2\text{keV}$  x-ray power (thin solid) and yield (short dash) for the uniform fill are much greater than the same measurement (thick solid for power, and long dash for yield) from the annular implosion.

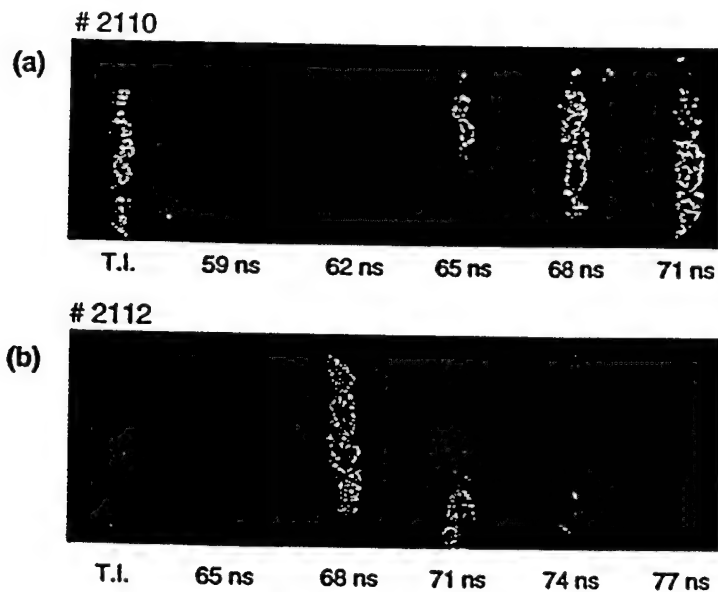


Figure 12. Time integrated plus five time resolved images for (a) an annular implosion, and (b) a uniform fill. The camera was filtered to record x-rays with energies greater than 800 eV.



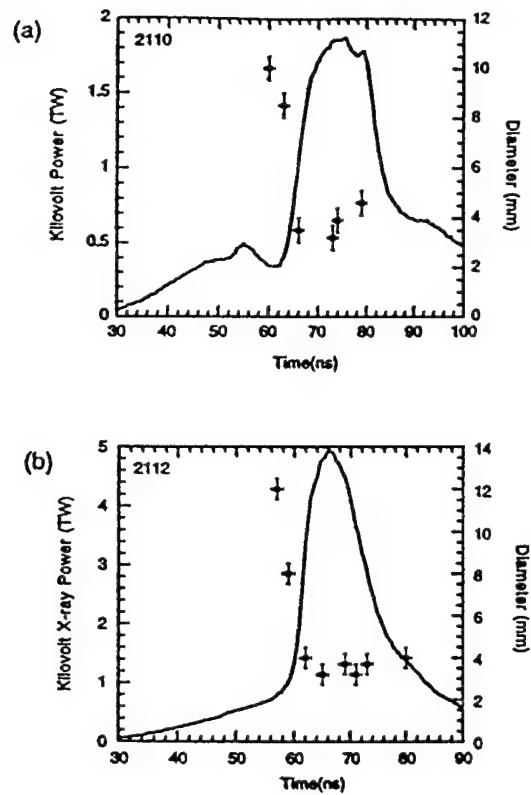


Figure 13. Overlays of the measured keV powers plus the measured pinch diameter (for  $h_\nu > 800$  eV) for (a) an annular implosion and (b) a uniform fill implosion. Both nozzle configurations produced pinches that were some 3.5 mm in diameter.

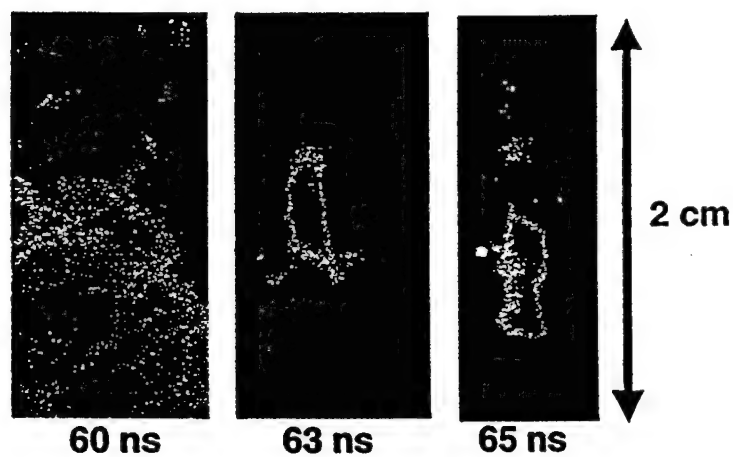


Figure 14. Three time resolved images (for  $h_\nu > 200$  eV) from a uniform fill Kr:Ar implosion (s2115).

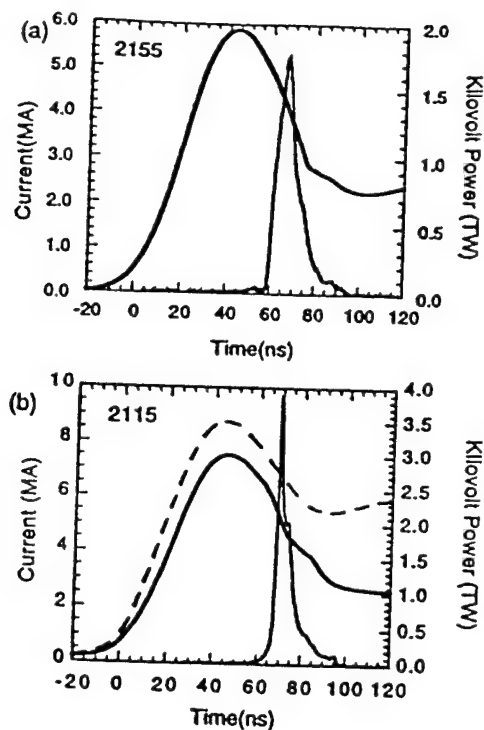


Figure 15. A comparison of (a) the load current and kilovolt power from an annular Kr:Ar implosion with (b) the MITI. (dashed) and load currents plus kilovolt x-ray power from Kr:Ar uniform fill implosion.

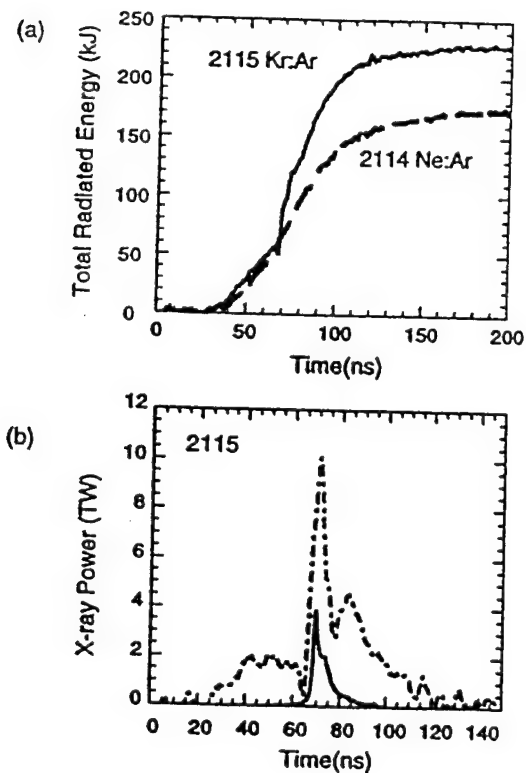


Figure 16. Comparisons of (a) the total x-ray yield, as measured by unfiltered bolometers, from a Ne:Ar (solid) and Kr:Ar (dashed) uniform fill implosions, and (b) comparisons of the total x-ray power (dashed) and keV x-ray power (solid) for a Kr:Ar uniform fill implosion.

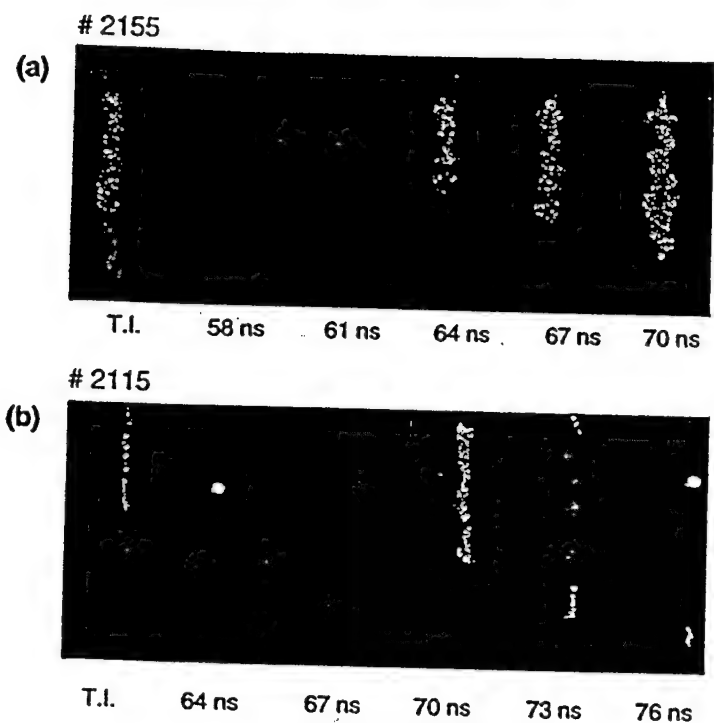


Figure 17. Time-integrated and five time resolved images ( $h\nu > 800$  eV) from (a) an annular Kr-Ar gas puff implosion, and (b) a uniform fill Kr-Ar implosion.

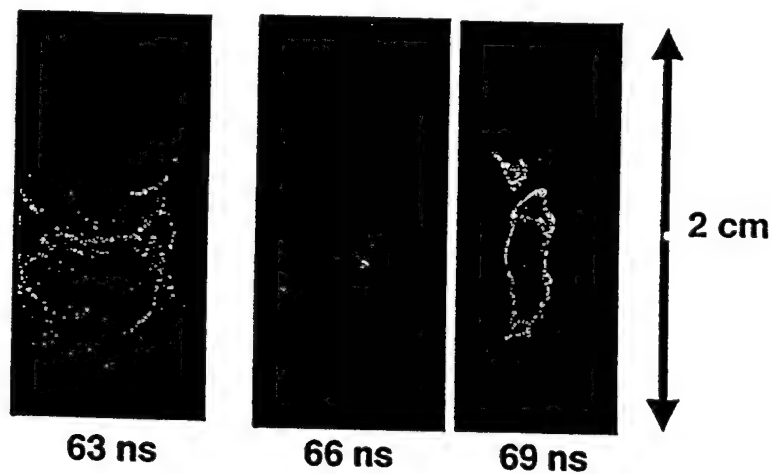


Figure 18. Three 100-ps duration images ( $h\nu > 200$  eV) of a uniform fill Kr-Ar implosion.

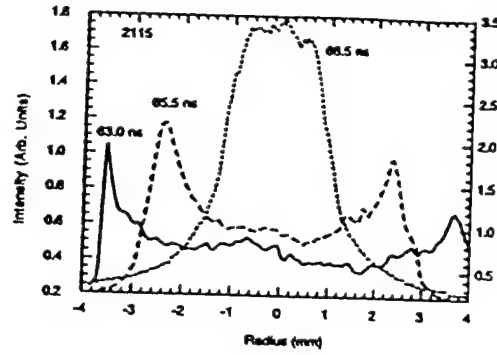


Figure 19. Intensity scans through the center 5 mm of the images in Fig. 18. The inferred implosion velocity is 70 cm/ $\mu$ s.

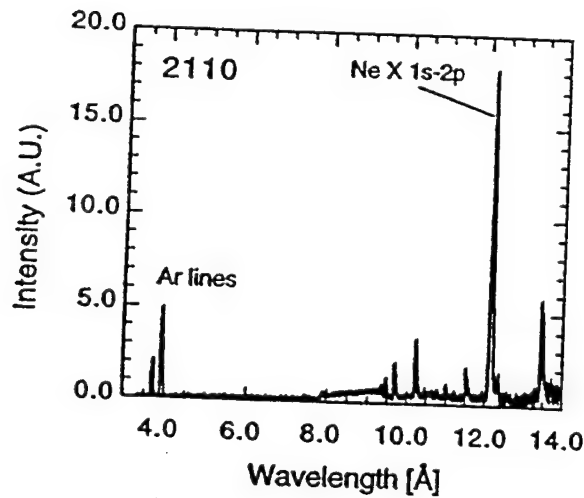


Figure 20. A time-integrated spectrum from an annular Ne-Ar implosion. The neon K-shell lines lie between 9.5 and 14 Å, with the most intense line being the Lyman-alpha line. The argon K-shell lines are at shorter wavelengths (around 4 Å).

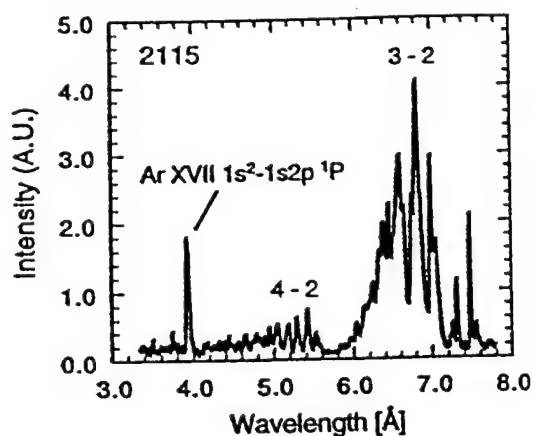


Figure 21. A time-integrated spectrum from an annular Kr-Ar implosion. The krypton L-shell lines, predominantly neon-like, lie between 6 and 8 Å for the 3-2 transitions and between 4.6 and 5.6 Å for the 4-2 lines. The argon helium-alpha is far stronger than the argon lyman-alpha.

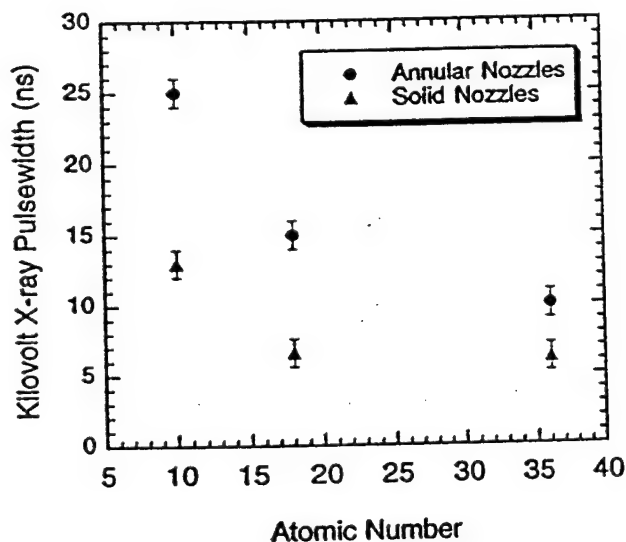


Figure 22. The FWHM of the kilovolt x-ray power pulse as a function of atomic number for both annular and uniform fill implosions. The pure argon data is shown for completeness.

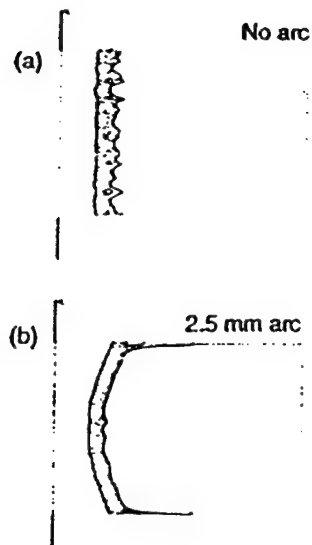


Figure 23. A comparison of two iso-density contour plots for krypton uniform fill gas puff calculations. In both cases, the outer diameters, the masses and implosion times match those in these experiments. In case (a) the gas puff is assumed to be a right cylinder, and in (b) it has a curved deflection applied with a maximum of 2.5 mm at the waist.

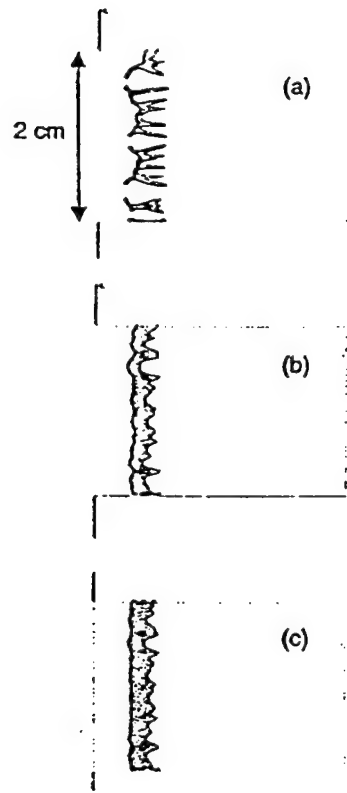


Figure 24. The effect of atomic number is shown for a series of right cylinder uniform fill implosions with (a) neon, (b) argon and (c) krypton.

### III. KINETIC ENERGY DISSIPATION IN MODERATE ATOMIC NUMBER PLASMAS

#### A. Introduction

One of the most difficult problems in the X-ray Simulator Program is how to increase the production of x rays in the 3 to 15 kilovolt energy range. Thus, the production of  $\sim 130$  kJ of 5 keV x rays from a titanium array implosion on the Z accelerator at Sandia National Laboratories is an important initial milestone; however, even in these experiments, there were challenges in load design that were unmet. When they are, significant improvements in the K-shell output from titanium wire array implosions can be expected in the future. Energetic x rays in the 3 to 15 keV interval can be produced from the K shells of moderate atomic number plasmas; however, a number of load design and machine design problems have to be solved in order to excite this emission. The main problem was theoretically defined and then experimentally confirmed over the past ten years; namely, that to efficiently generate energetic K-shell x rays in Z-pinch implosions, loads have to be designed that allow a significant fraction of a sufficient amount and kind of plasma kinetic energy to be thermalized in as short a time interval as possible. A fast thermalization process is necessary, since the faster a plasma can be ionized through the L shell and into the K shell, the more the L-shell radiation losses can be minimized along the way. However, the speed of ionization depends on both the density and temperature rise in a plasma, so that another of the main problems in load design is to achieve both.

Basically, there are two ways to thermalize kinetic energy: one is by plasma fluid compression and the other is through the nonlinear process of shock wave generation and dissipation. Recent experiments have shown that rapid compressional heating can be fairly non-uniform, leading to hot plasma cores and much cooler surrounding shells. How these gradient structures are formed is, at present, not entirely understood and predictable. It was only recently that methods were developed to begin to diagnose them from experimental x-ray spectral data.<sup>1,2</sup> Extreme temperature gradients tend to lower the fractional amount of plasma that can radiate from the K shell and to decrease the efficiency of K-shell x-ray production. At the passage of a shock front, on the other hand, a plasma can undergo large, rapid, and, in principle, predictable jumps in electron and ion temperature. However, how strongly shock waves in highly ionizable, moderate atomic number, Z-pinch plasmas are generated, what their structure is, and how they affect Z-pinch dynamics has not, as yet, been analyzed. These problems involve a sizable amount of computer resource even in a 1-D hydrodynamics calculation, and most such computer resources have been shunted into 2-D Rayleigh-Taylor calculations.

In hydrodynamics computer calculations, the development and structure of shock fronts is generally poorly modeled and not understood when ionization is involved. Artificial viscosities are used to soften the gradients generated in these calculations and to deliberately leave them inadequately resolved. To model shock formation without the use of artificial viscosities requires the use of more zones in hydrodynamics calculations than computer resources in the past have allowed, and the computation demands become greater when a non-equilibrium ionization dynamics is involved. Moreover, because of the early focus on hydrogen in the development of plasma physics, the erroneous procedures of ascribing all of the artificial viscosity to ions and of ignoring the

real viscosity's ionization state dependence were oftentimes employed independent of the atomic number or ionization state of the plasma. Over the last two years some work was begun to remedy these deficiencies. Some of this work is summarized in this section.

The process of remedying this problem took two steps. In the first step, taken last year, it was demonstrated that the electron pressure tensor has nonlinear terms that can become larger than the classical viscosity term when steep temperature and density gradients are generated in a plasma (as in a shock structure). This work applied only to spherically symmetric or planar plasmas in order to simplify an (already complex) calculation. In the second step, undertaken this year, the calculation of these nonlinear pressure tensor terms was extended to the cylindrically symmetric geometry of a Z-pinch plasma. The procedure for calculating these terms is described in a paper that will be published in the journal, *Physics of Plasmas*;<sup>3</sup> expressions for them are derived and presented in this paper. The pressure tensor is important in thermalization processes only at shock fronts and is attributable to the very sharp gradients across the front. How this thermalization process affects, and is affected by, the rapid ionization dynamics that takes place following the passage of a shock front are problems yet to be researched.

This section consists of five subsections beginning with this introduction. In subsection B, a brief discussion of the electron pressure tensor in a 1-D Z-pinch geometry is given. Then, in subsection C, a planar shock front calculation is described that demonstrates the important role that the electron pressure tensor can play in determining the relative amounts of electron and ion heating across the front. The calculation does not involve any ionization dynamics, so it must be carried out for a totally ionized plasma (the choice  $Z = 22$  was made). A 1-D hydrodynamics calculation is post-analyzed and discussed in subsection D. It illustrates the potential importance of the nonlinear pressure tensor terms discussed in subsection B. The magnitude of these terms is calculated by post-processing the 1-D hydrodynamics calculation that was described in the 1997 final report of Code 6720. This calculation was not designed for shock wave studies, but it utilized 100 zones to increase the resolution of the current profile. It was thus able to better resolve the temperature profile as well. As a consequence, it showed the existence of a sharp thermal shock front (unseen in a similar 30 zone calculation) that propagated to the axis prior to plasma assembly on axis. Finally, all of the above work is summarized in subsection E.

## B. The Electron Pressure Tensor

In a cylindrically symmetric Z-pinch plasma, the fluid pressure tensor,  $\Pi_{fluid}$ , when displayed as a matrix, has the form:

$$\Pi_{fluid} = \begin{pmatrix} \Pi_{rr} & 0 & \Pi_{rz} \\ 0 & -(\Pi_{rr} + \Pi_{zz}) & 0 \\ \Pi_{rz} & 0 & \Pi_{zz} \end{pmatrix} = \Pi_i + \Pi_e.$$

The fluid pressure tensor is the sum of  $\Pi_i$ , the pressure tensor for the ions and  $\Pi_e$ , that for the electrons. The electron pressure tensor also consists of two parts:

$$\Pi_e = \Pi_{e0} + \Pi_e^{NL},$$

where  $\Pi_{e0}$  is the classical (linear) viscosity part of the pressure tensor and  $\Pi_e^{NL}$  is the newly calculated nonlinear part, consisting of five different contributions in an (r,z) Z-pinch:

$$\Pi_e^{NL} = \Pi_e^T + \Pi_e^J + \Pi_e^{TN} + \Pi_e^{TJ} + \Pi_e^{NJ}.$$



The superscripts,  $T$ ,  $N$ , and  $J$ , on the right side of this equation refer to the dependence of the different terms on either the temperature gradient, the density gradient, or the current density respectively. The dependence on temperature and density gradients is given in terms of two dimensionless vector quantities,  $\mathbf{x}_t$  and  $\mathbf{x}_n$  whose  $r$ - and  $z$ -components are given by

$$\begin{aligned}x_{tr} &\equiv v_{th} \tau_e \partial_r \ln(T_e), & x_{tz} &\equiv v_{th} \tau_e \partial_z \ln(T_e), \\x_{nr} &\equiv v_{th} \tau_e \partial_r \ln(n_e), & x_{nz} &\equiv v_{th} \tau_e \partial_z \ln(n_e),\end{aligned}$$

where

$$v_{th} \equiv \sqrt{\frac{2kT_e}{m}}.$$

General formulas for the electron pressure tensor were derived in Ref. (3), but this discussion will be limited to their application to 1-D hydrodynamics modeling. In this case, the nonzero components of the classical electron and ion pressure tensors are given by

$$(\Pi_{e0})_{rr} = -\tau_e \left[ \left( \frac{\hat{\eta}_0}{3} + \hat{\eta}_1 \right) \partial_r v_r - \frac{2}{3} \hat{\eta}_0 \frac{v_r}{r} \right] p_e,$$

$$(\Pi_{e0})_{zz} = -\tau_e \left[ \left( \frac{\hat{\eta}_0}{3} - \hat{\eta}_1 \right) \partial_r v_r - \frac{2}{3} \hat{\eta}_0 \frac{v_r}{r} \right] p_e,$$

$$(\Pi_i)_{zz} = -0.96 \tau_i \left( \partial_r v_r - \frac{v_r}{2r} \right) p_i,$$

and

$$(\Pi_i)_{zz} = 0.48 \tau_i \left( \partial_r v_r + \frac{v_r}{r} \right) p_i.$$

The electrons have a more complicated pressure tensor than the ions because, in a Z-pinch, they are magnetized while the ions are not. The  $\hat{\eta}_0$  and  $\hat{\eta}_1$  are dimensionless Braginskii coefficients that depend on both the ionization state,  $Z$ , of the plasma and on the magnetic field,  $B$ , through the dimensionless parameter:

$$x_b \equiv \omega_e \tau_e = \frac{eB}{mc} \tau_e.$$

In Ref. (3), expressions for the nonlinear terms in  $\Pi_e$  were derived that are of the same form as the ones derived by Braginskii for  $\Pi_{e0}$ . For example, for  $\Pi_e^T$  and  $\Pi_e^{TN}$ ,

$$(\Pi_e^T)_{rr} = \frac{1}{2} \left( \frac{\hat{\eta}_0^T}{3} + \hat{\eta}_1^T \right) x_{tr}^2 p_e,$$

$$(\Pi_e^T)_{zz} = \frac{1}{2} \left( \frac{\hat{\eta}_0^T}{3} - \hat{\eta}_1^T \right) x_{tr}^2 p_e,$$

$$(\Pi_e^{TN})_{rr} = \left( \frac{\hat{\eta}_0^{TN}}{3} + \hat{\eta}_1^{TN} \right) x_{tr} x_{nr} p_e,$$

$$(\Pi_e^{TN})_{zz} = \left( \frac{\hat{\eta}_0^{TN}}{3} - \hat{\eta}_1^{TN} \right) x_{tr} x_{nr} p_e.$$

In all of the above pressure tensor expressions, the  $\eta$  coefficients are functions of  $Z$  and  $x_b$ , for example:

$$\hat{\eta}_{0,1} = \hat{\eta}_{0,1}(Z, x_b) \quad \hat{\eta}_{0,1}^T = \hat{\eta}_{0,1}^T(Z, x_b).$$

These dependences are calculated in Ref. (3) and are illustrated in Figs. (1) and (2). Fig. (1) shows both the dependence of  $\hat{\eta}_0^T \equiv \hat{\eta}_0^T$  and the ratio,  $\hat{\eta}_0^T/\hat{\eta}_0$ , on  $x_b$  for both 6 times (carbon-like) and 36 times (krypton-like) ionized plasmas. Fig. (2) shows the same information for the  $\hat{\eta}_1^T \equiv \hat{\eta}_1^T$  coefficient. These figures indicate two important features of the  $\Pi_e^T$  coefficients. One, they are both much larger than the corresponding coefficients for  $\Pi_{e0}$ , and two, they quickly decrease in size for sufficiently large magnetic field strengths:  $x_b > 0.02$ . This behavior is important at the surface of a pinch, where the bulk of the pinch current flows and where magnetic fields are largest. In this region of the plasma,  $\Pi_e^J$  does not go to zero and may become important.

### C. Steady-state Shock Structure Calculations

Since the early work on the structure of plasma shock waves,<sup>4-6</sup> ion viscosity was believed to play the dominant role in determining shock structure due to the large mass difference,  $m_i/m_e \gg 1$ , between ions and electrons. This meant that all of the heat generated in a shock front was deposited into the ion component of the plasma when shock fronts were simulated in computer hydrodynamics calculations. However, in high- $Z$  plasmas, classical electron viscosity can exceed the ion viscosity.<sup>7</sup> In this case, the role of the electron viscosity has to be reconsidered along with the energy partition between the components of the plasma that occurs during shock heating.

Shock structure calculations are oftentimes carried out in the coordinate frame of a steady-state shock front, thereby allowing the time derivative terms in the plasma fluid equations to be ignored. When a shock front passes through a highly ionizable plasma, the rapid change in electron temperature will drive a time-dependent ionization that violates the assumption of steady-state. Thus, in order to carry out a steady-state shock calculation, it is necessary to assume that the plasma is fully ionized. In this section, a planar shock wave calculation will be described, which allows one also to ignore B-field effects. Fig. (3) was used to select the degree of ionization ( $Z = 22$ ) assumed in the calculation. The red curve in Fig. (3) shows the ratio of electron to ion viscosity coefficients that is given by the formula to the right of the figure. This ratio is the same as the ratio of electron to ion pressure tensors. Only the classical (linear) viscosity for the electrons was used in these calculations. Since  $Z$  times as many electrons must be viscously heated as ions, the blue curve, which is  $1/Z$  times the viscosity ratio, is also drawn. The blue curve exceeds 1 when  $Z > 13$ . Past this  $Z$ , electron viscous heating exceeds ion heating; hence, the choice of  $Z = 22$  was made, corresponding to a fully ionized titanium plasma.

The calculation makes use of conventional Navier-Stokes shock structure equations, which can be found in Ref. (8):

$$n_i u = \text{const}_1 \text{ (mass conservation)}$$

$$m_i n_i u^2 + n_i (T_i + Z T_e) - \frac{4}{3} (\eta_i + \eta_e) \frac{du}{dx} = \text{const}_2 \text{ (momentum conservation)}$$

$$\begin{aligned}
& \frac{1}{2}m_i n_i u^3 + \frac{5}{2}n_i u(T_i + ZT_e) - \frac{4}{3}(\eta_i + \eta_e)u \frac{du}{dx} \\
& \quad - \kappa_e \frac{dT_e}{dx} = \text{const}_3 \text{ (energy conservation)} \\
& \frac{3}{2}n_i u T_i + n_i T_i \frac{du}{dx} = \frac{4}{3}\eta_i \left(\frac{du}{dx}\right)^2 \\
& \quad + \frac{3m_e Z n_i}{m_i \tau_e} (T_e - T_i) \text{ (ion energy balance)}.
\end{aligned}$$

In these equations,  $\eta_e = \hat{\eta}_0 \tau_e p_e$  and  $\eta_i = 0.72 \tau_i p_i$ . The constants in them are determined by the Hugoniot relations that hold for a given shock strength. These equations apply to charge neutral plasmas in which  $n_e = Z n_i$ . They were employed by treating the viscous subshock as a discontinuity and by solving for the structure of the electron thermal precursor in the temperature relaxation zone, whose extent is determined by the electron thermal conductivity. This zone is located in front of the viscous subshock.

Fig. (4) shows the structure for a Mach 5 shock wave for two cases: one case with and the other without the inclusion of the electron viscosity in the calculation. As noted in the figure, if electron viscosity is neglected, ion heating can be seriously overestimated by more than a factor of two in this Mach 5 example. This error would be further enhanced in cumulative flows (such as occur in Z-pinch implosions) where the shock wave is amplified as it converges to the axis. Since it is electron heating and not ion heating that produces kilovolt x rays, the omission of electron viscosity could represent a serious error in modeling moderate atomic number Z-pinch pinch implosions designed to produce K-shell x rays.

Other facets of this shock wave calculation are shown in Figs. (5)-(7). Fig. (5) shows plots of two of the dimensionless parameters defined above: the (single) components of  $\mathbf{x}_t$  and  $\mathbf{x}_n$  ( $l_e = v_{th} \tau_e$ ). Since temperature and density gradients are not resolved in this calculation in the subshock region, the main information these plots convey pertains to the temperature relaxation zone. In this region,  $\mathbf{x}_t$  and  $\mathbf{x}_n$  acquire sufficiently large values in these calculations for the nonlinear contributions to the electron heat conductivity and pressure tensor to exceed the linear expressions that are conventionally used for these quantities. Fig. (6) indicates that this effect for electron heat conduction becomes larger as the Mach number increases, reaching a point, for Mach numbers of around 13 or 14, where the calculation breaks down because flux limiting must be imposed, i.e., the calculation would otherwise allow an unphysical amount of heat to be conducted. Finally, Fig. (7) shows by how much, as a function of Mach number, the ratio of peak temperatures is changed (and electron heating increased significantly) when electron viscosity is included in this  $Z = 22$  shock wave calculation. In a Z-pinch plasma, the direct conversion of kinetic energy to electron thermal energy could have a significant impact on the amount of ionization and x-ray emission that a moderate atomic number plasma would experience.

#### D. Post-analysis of a Z-accelerator, Z-pinch Implosion

Currently, there is no computer code able to assess the impact of the nonlinear electron heat conduction and pressure tensor terms on the hydrodynamics of a Z-pinch plasma. However, by post-processing a present-day hydrodynamics calculation, it is possible to assess whether or not these terms can be expected to play an important role in this dynamics. The calculation, whose

post-processing will be discussed in this subsection, is illustrated in Fig. (8). It was carried out using 100 cells, whose boundaries as a function of time are drawn in this figure. The insert in Fig. (8) shows the current, corresponding to the Z accelerator at Sandia National Laboratories, that was used to drive the aluminum Z-pinch load in this calculation. The current peaks at 17 MA and experiences a dip as the load compresses on axis at  $\sim 134$  ns. The five equally spaced vertical lines at the top of Fig. (8) indicate the five times at which the temperature profiles in Fig. (9) were drawn.

The profiles in Fig. (9) demonstrate one of the key features of this simulated Z-pinch implosion; namely, that, prior to kinetic energy thermalization on axis, a well-defined temperature front propagates to the axis. It has two important effects on the Z-pinch dynamics that (would in general) depend on the timing of the front relative to the time of peak compression. One, just before the front arrives, a point in the inner plasma sits at a low temperature of  $\sim 20$  eV. In 2, 1, or less ns after the front has passed, the electron temperature jumps quickly up to 200 to 300 eV, producing a very rapid, and undoubtedly time-dependent, ionization in the plasma. Two, at the last of these times, the core of the plasma has been heated uniformly to a high temperature in excess of 400 eV. As the implosion continues, this core plasma is heated further and some compression continues; however, the compression is impeded by the preheating of this core region. The inability to reach high densities in the heated core of the plasma is one cause of degraded K-shell emission that needs to be overcome with better load design (such as wire nesting or fill gases).

Fig. (9) also indicates that 1-D hydrodynamics calculations, of both current and future interest, can be made to generate very large temperature and density gradients with the proper amount of high resolution zoning. Such gradients, in turn, lead to the breakdown of these calculations. To assess some of the relevance of this possibility, the implosion of Fig. (8) was post-processed to determine the magnitude of the electron relative to the ion viscosity. Note, however, that all of the artificial viscosity was used to heat the ions in this calculation. There are two fractional quantities of interest in making this appraisal:

$$f_e^{(0)} = \frac{|\Pi_{e0}|}{|\Pi_{e0}| + |\Pi_i|} \quad f_e = \frac{|\Pi_e|}{|\Pi_e| + |\Pi_i|}$$

The first ratio,  $f_e^{(0)}$ , involves only the classical, linear, electron pressure tensor, and gives the fraction of the total pressure tensor that the electron contribution makes. The nonlinear terms in the electron pressure tensor have been added to this ratio in  $f_e$ . The size of these two ratios both prior to and at the time of peak compression are of interest. These times are indicated in Fig. (8) by the vertical lines at the top of the figure: the darkened, middle line in the cluster of five and the line at 133.8 ns.

At the time prior to peak compression, the profiles of these two ratios are shown in Figs. (10) and (11). Without the nonlinear terms (Fig. (10)), the electron viscosity is larger than the ion viscosity only in the shell region of the plasma. The dip in electron viscosity in the shell region is caused by the magnetic field in this region since the electrons are magnetized, while the ions are not. With the inclusion of nonlinear terms (Fig. (11)), the electron pressure tensor in the shell region now totally dominates the ion viscosity, and, in the core region, it dominates at the temperature front. Notice that the sharp peak in  $f_e$  at the temperature front is poorly resolved even with 100 cells in the calculation.

At the time of peak compression, the profiles of the  $f_e^{(0)}$  and  $f_e$  ratios are shown in Figs. (12) and (13). Again, without the nonlinear terms (Fig. (12)), the electron viscosity tends to be larger

than the ion viscosity only in the shell region of the plasma. There is again a dip in electron viscosity in this region because of the magnetic field. When the nonlinear terms are added (Fig. (13)), the importance of the electron pressure tensor relative to the ion viscosity is extended well into the core region of the plasma. , Several peaks in  $f_e$  occur because of the severity of the temperature and density gradients that are generated at the time of peak compression in the midst of the kinetic energy thermalization process. The dip in electron viscosity brought on by the magnetic field is also enhanced by the nonlinear terms.

## E. Summary

Load designs that promote the direct thermalization of kinetic energy into the electrons have yet to be studied, because it was recognized only a year or two ago that such a possibility exists. Prior to this time, conventional wisdom assumed that all of a plasma's viscosity was generated by the ions. This wisdom derived from the heavy concentration of activities in plasma physics on experiments involving hydrogen. Thus, while the hydrodynamics calculation that was post-processed above gave some useful information about the potential importance of the electron pressure tensor in Z-pinch calculations, it mostly showed that present-day hydrodynamics calculations have the potential to be inconsistent and to give wrong answers if they are carried out for high atomic number plasmas, such as krypton, while ascribing all of the artificial viscosity effects to ions. They may also be misleading if they are carried out with insufficient zoning that inadequately resolves the gradient structure of the plasma and incorrectly computes the amount of thermalization taking place as a result of shock front formation.

In summary, the classical electron contribution to a plasma's viscosity can easily become comparable to or larger than the ion viscosity in highly ionizable plasmas. In addition, nonlinear terms make sizable contributions to the electron pressure tensor that can be larger than the classical (linear) viscosity in regions where large gradients in temperature, density, or current density are generated. At the discontinuity of a strong shock front in a highly ionized ( $Z > 20$ ) plasma, the classical electron viscosity can be expected to reduce the jump in ion temperature substantially. Finally, the production of sizable amounts of K-shell x rays from moderate atomic number plasmas may require load designs that promote the generation of shock fronts. The use of artificial viscosity in calculations of these load designs needs to be re-investigated and most likely upgraded.

## REFERENCES

1. K. G. Whitney, J. W. Thornhill, P. E. Pulsifer, J. P. Apruzese, T. W. L. Sanford, T. J. Nash, R. C. Mock, and R. B. Spielman, "Analyzing Time-resolved Spectroscopic Data from an Azimuthally Symmetric, Aluminum-wire Array, Z-pinch Implosion", *Phys. Rev. E* **56**, 3540 (1997).
2. J. P. Apruzese, P. E. Pulsifer, J. Davis, R. W. Clark, K. G. Whitney, J. W. Thornhill, T. W. L. Sanford, G. A. Chandler, C. Deeney, D. L. Fehl, T. J. Nash, R. B. Spielman, W. A. Stygar, K. W. Struve, R. C. Mock, T. L. Gilliland, D. O. Jobe, J. S. McGurn, J. F. Seamen, J. A. Torres, and M. Vargas, "K-shell radiation physics in the ultrahigh optical depth pinches of the Z generator", *Phys. of Plasmas* **5**, 4476 (1998).
3. K. G. Whitney, "First-order Calculation of the Pressure Tensor for Cylindrical, Z-pinch Plasmas", *Phys. of Plasmas*, to be published.
4. V. D. Shafranov, *Sov. Phys. JETP*, **5**, 1183 (1957).
5. J. D. Jukes, *J. Fluid Mech.*, **3**, 275 (1957).
6. M. Y. Jaffrin and R. F. Probstein, *Phys. Fluids*, **7**, 1658 (1964).
7. K. G. Whitney, "Momentum and Heat Conduction in Highly Ionizable Plasmas", *Phys. of Plasmas*, **6**, 816 (1999).
8. M. A. Liberman and A. L. Velikovich, *Physics of Shock Waves in Gases and Plasmas*, (Springer, Berlin, 1986).

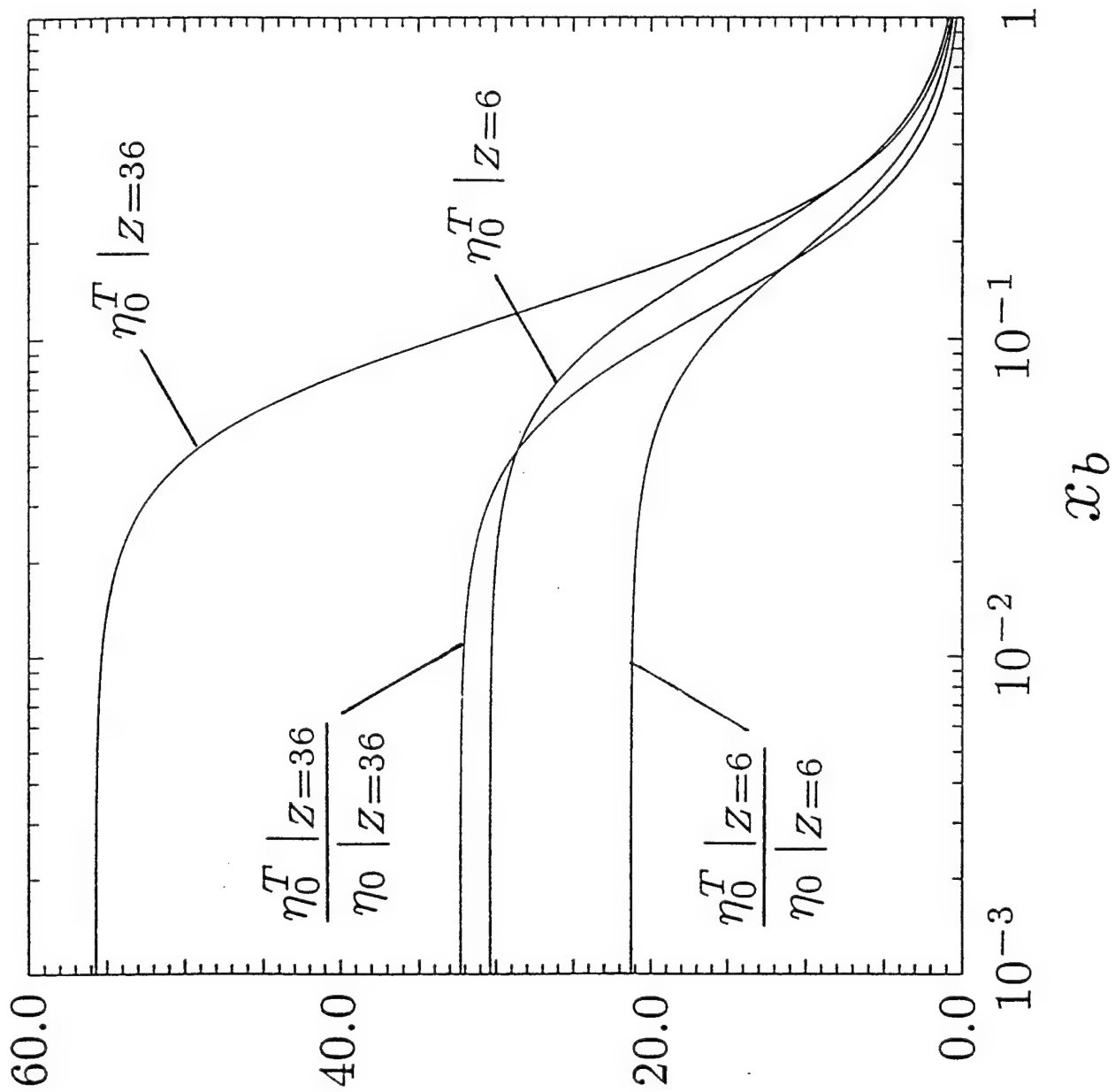


Figure 1

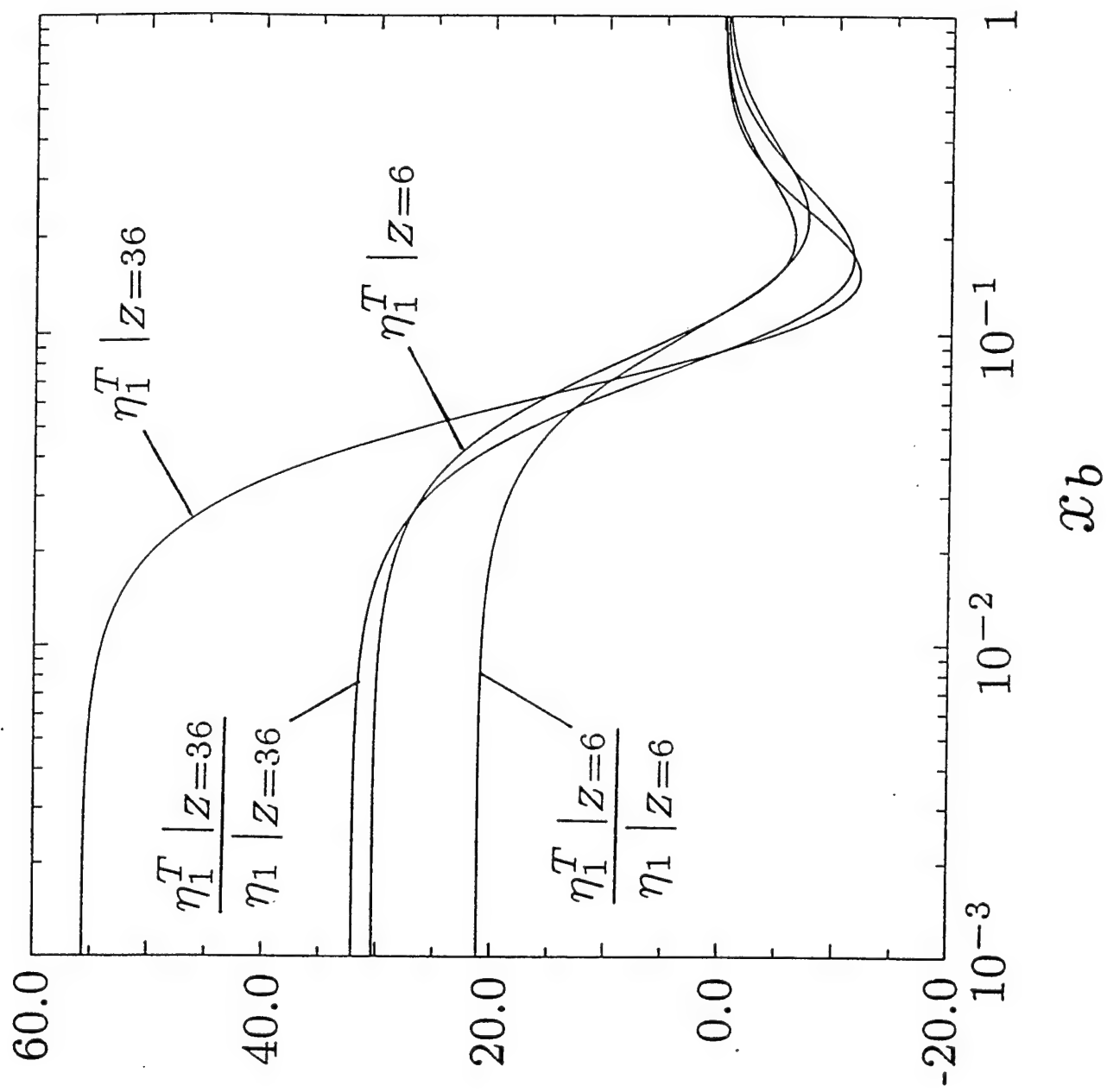


Figure 2

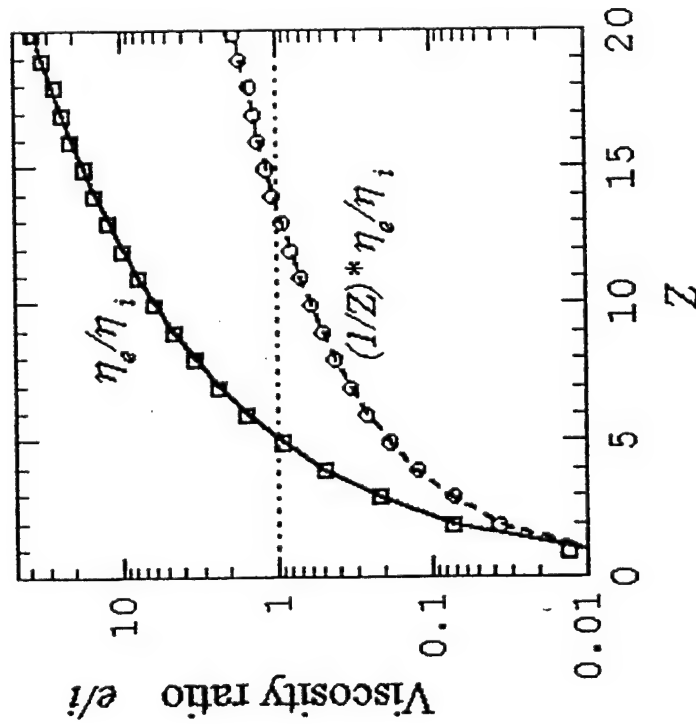


# Electron and ion viscosity compared

- In a fully ionized plasma, the ratio of electron-to-ion viscosity is given by

$$\frac{\eta_e}{\eta_i} = 1.33 \left( \frac{m_e}{m_i} \right)^{1/2} \left( \frac{T_e}{T_i} \right)^{5/2} \times \frac{Z^4 (Z^2 + 2.82Z + 1/343)}{Z^3 + 4.434Z^2 + 5.534Z + 1.78}$$

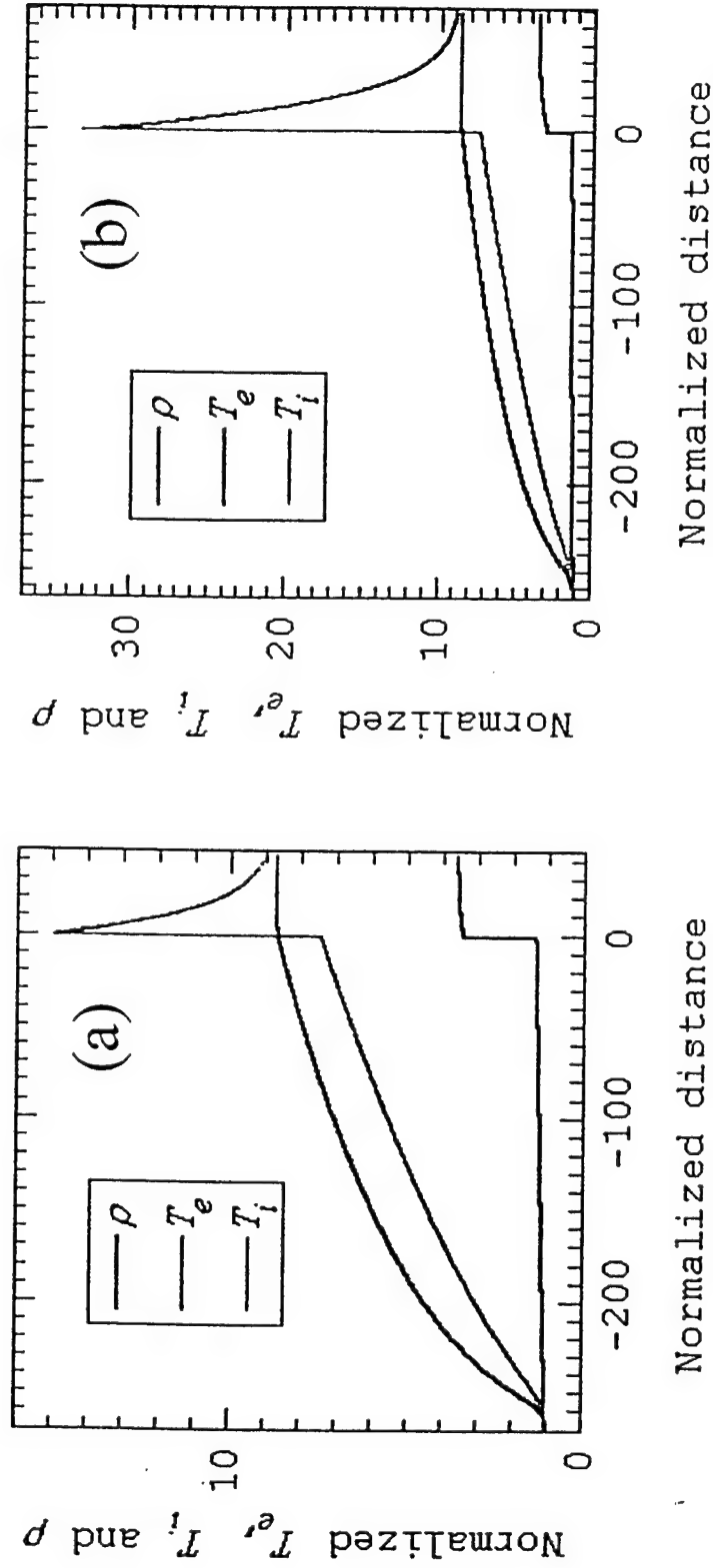
- With  $T_e = T_i$ , electron viscosity exceeds ion viscosity and  $Z$  times ion viscosity for  $Z > 5$  and  $Z > 13$ , respectively



Viscosity ratio in a fully ionized isothermal plasma. Points corresponds to exact atomic weights  $A(Z)$ , curves are plotted assuming  $A=2Z$ .

Figure 3

Structure of a  $M_I = 5$  shock wave in a fully ionized plasma ( $Z=22$ ) with electron viscosity accounted for (a) and neglected (b)



If the electron viscosity is neglected, the ion heating in strong shock waves in high- $Z$  plasmas could be seriously overestimated (more than twice, in the above example). This error might be further enhanced in cumulative flows, when a shock wave is amplified converging to a center or to an axis

Figure 4

Profiles of the parameters,  $x_n = |(1/n) \cdot dn/dx| \cdot l_e$  and  $x_{Te} = |(1/T_e) \cdot dT_e/dx| \cdot l_e$ , for a  $M_1 = 5$  shock wave in a fully ionized plasma ( $Z=22$ ) with electron viscosity accounted for (a) and neglected (b)

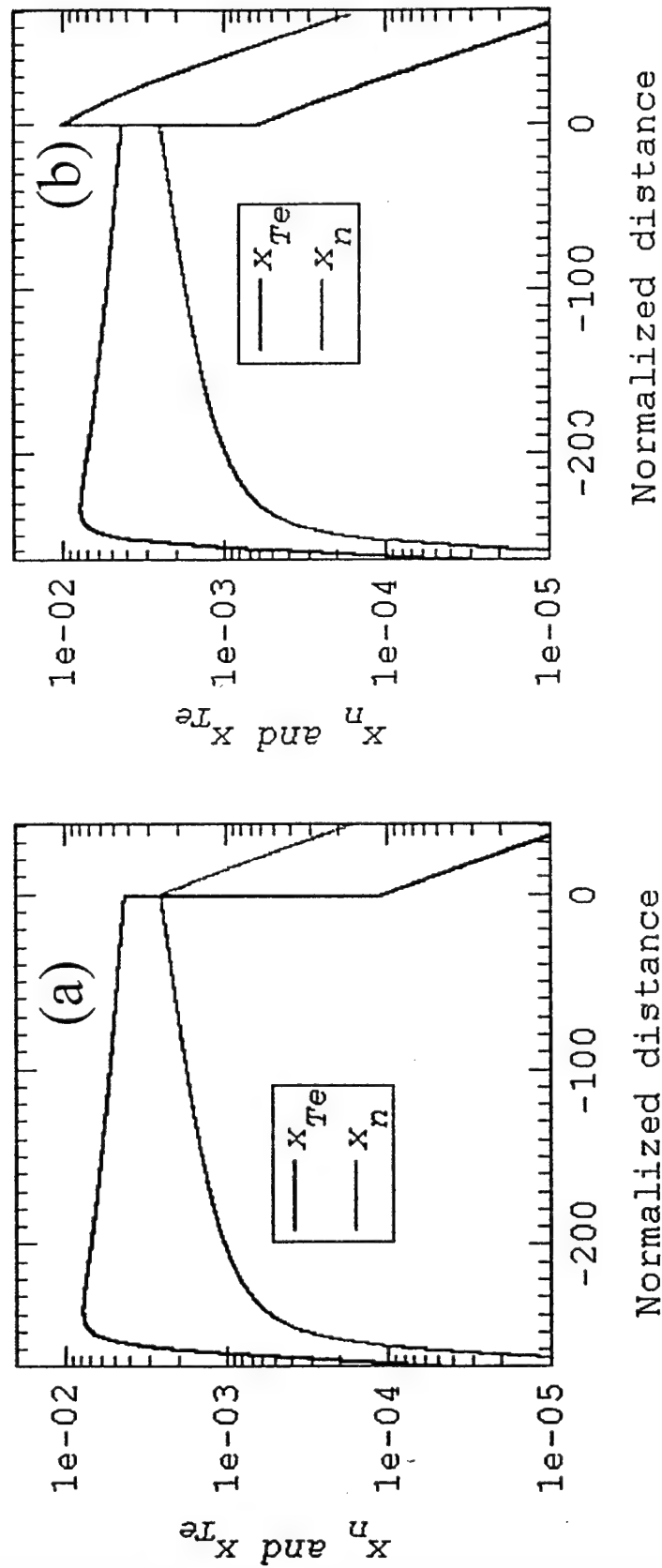


Figure 5

- In a strong shock wave, the peak value of the parameter

$$x_t = v_{th} \tau_e \partial_r \ln T_e$$

equals

$$\frac{\sqrt{Z+1}(Z^2 + 3.936Z + 1.327)}{714Z^{3/2}(Z + 0.5879)} M$$

Values large enough to make the nonlinear corrections to transport coefficients relevant are achieved in moderately strong shocks

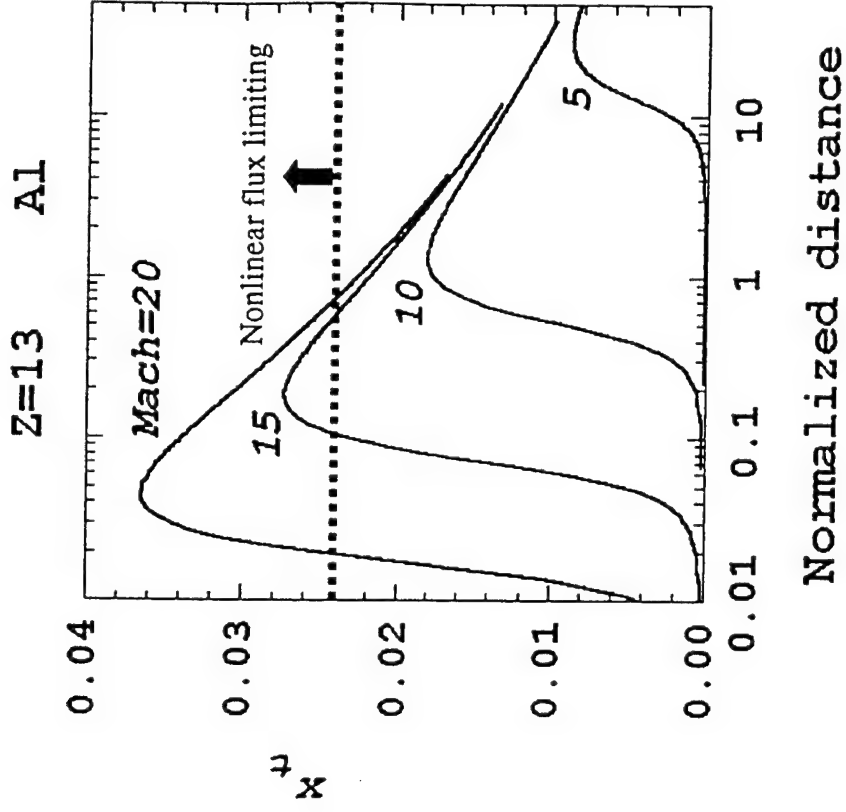
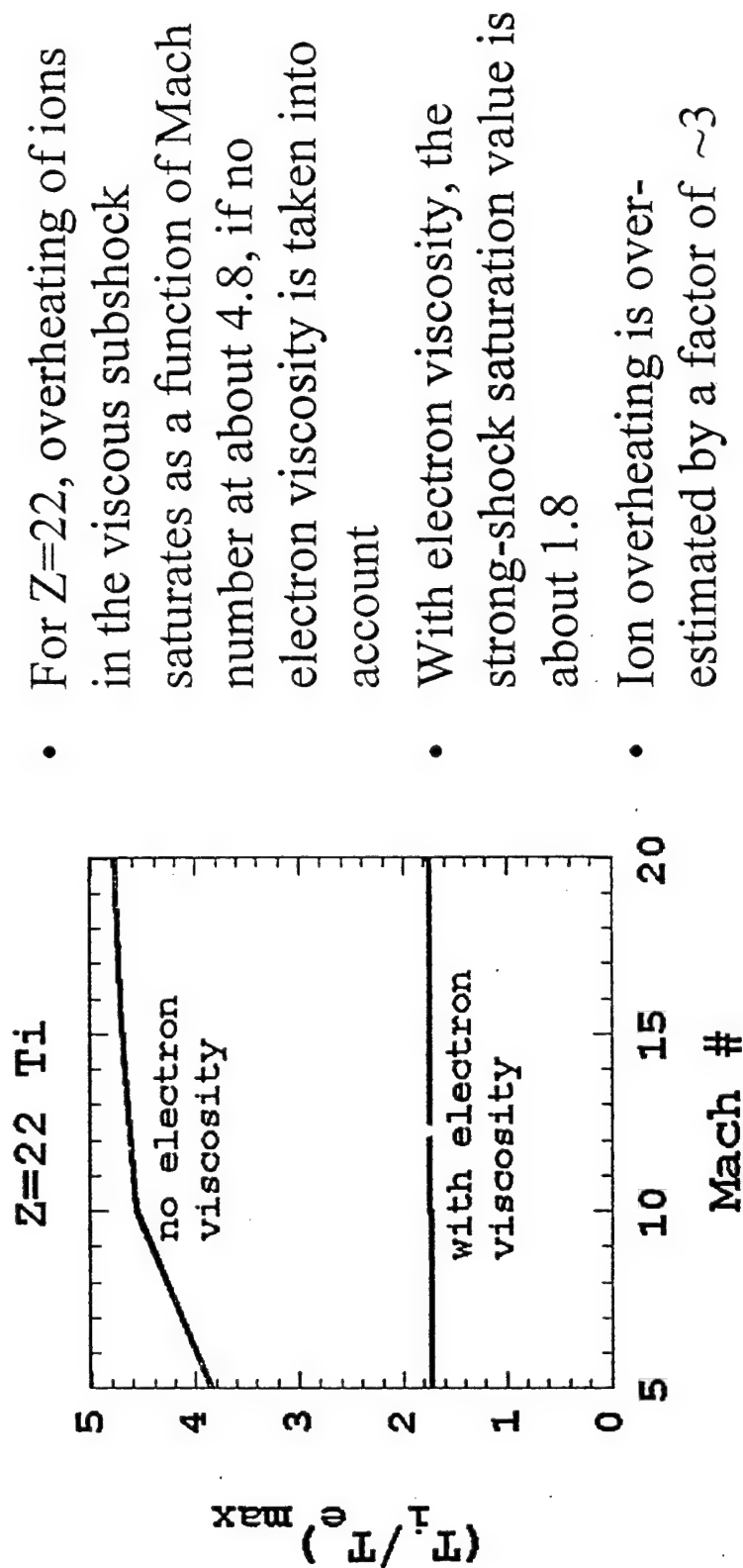


Figure 6

Overheating of ions in strong plasma shock waves could be over-estimated if electron viscosity is neglected



- For  $Z=22$ , overheating of ions in the viscous subshock saturates as a function of Mach number at about 4.8, if no electron viscosity is taken into account
- With electron viscosity, the strong-shock saturation value is about 1.8
- Ion overheating is over-estimated by a factor of  $\sim 3$

Figure 7

Implode an Al array driven by the Z-accelerator

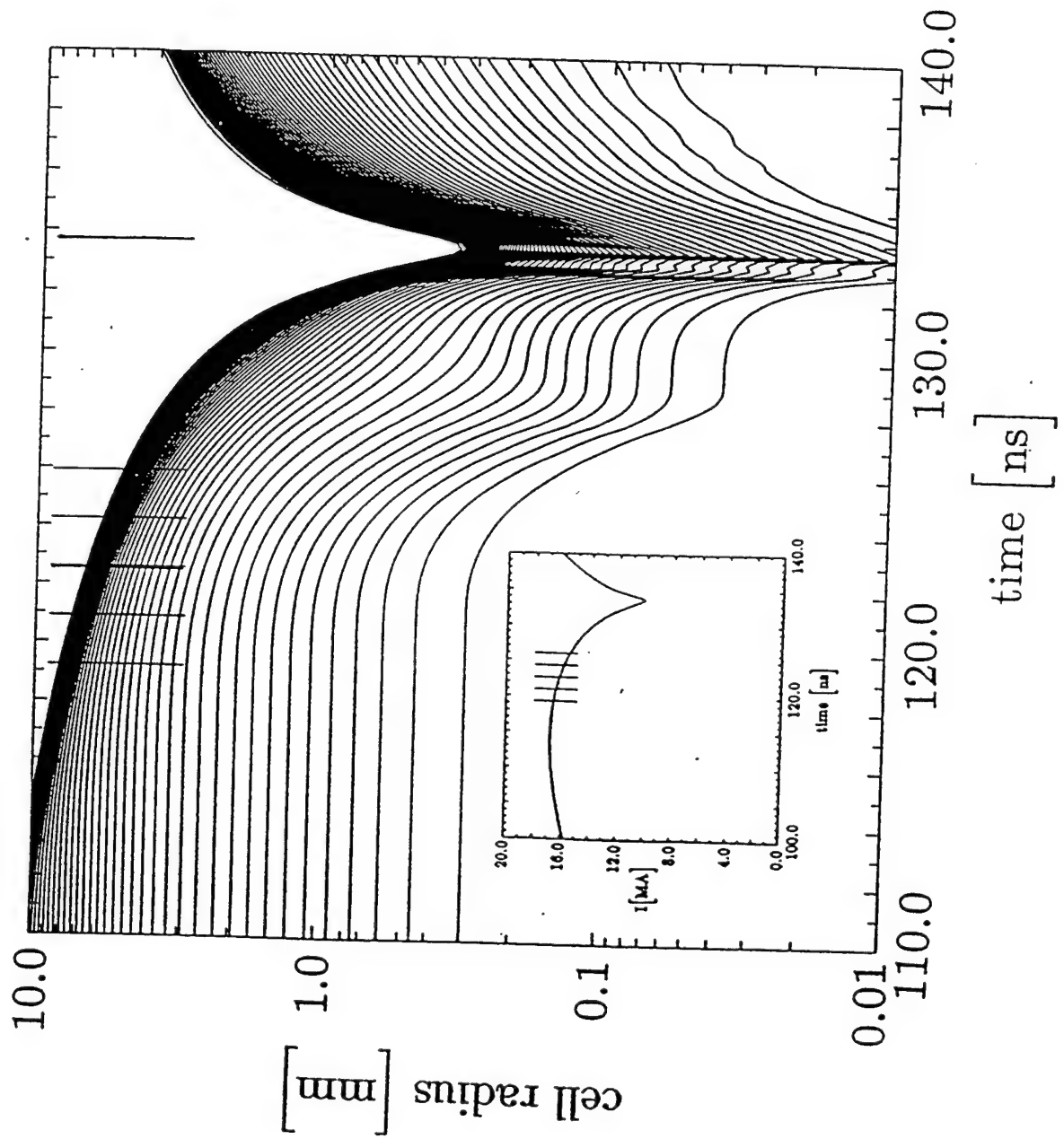


Figure 8

A temperature front propagates to the axis

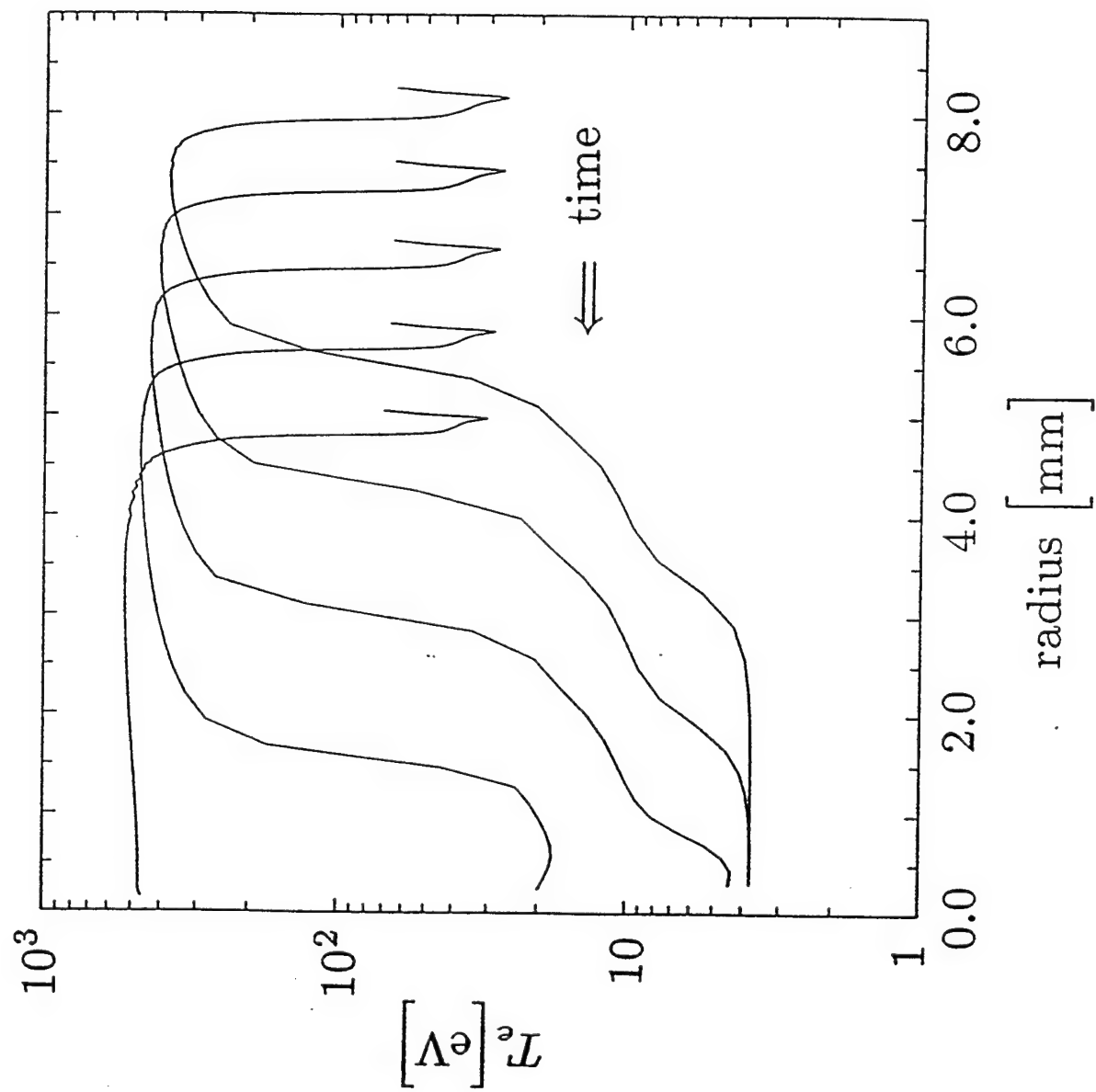


Figure 9

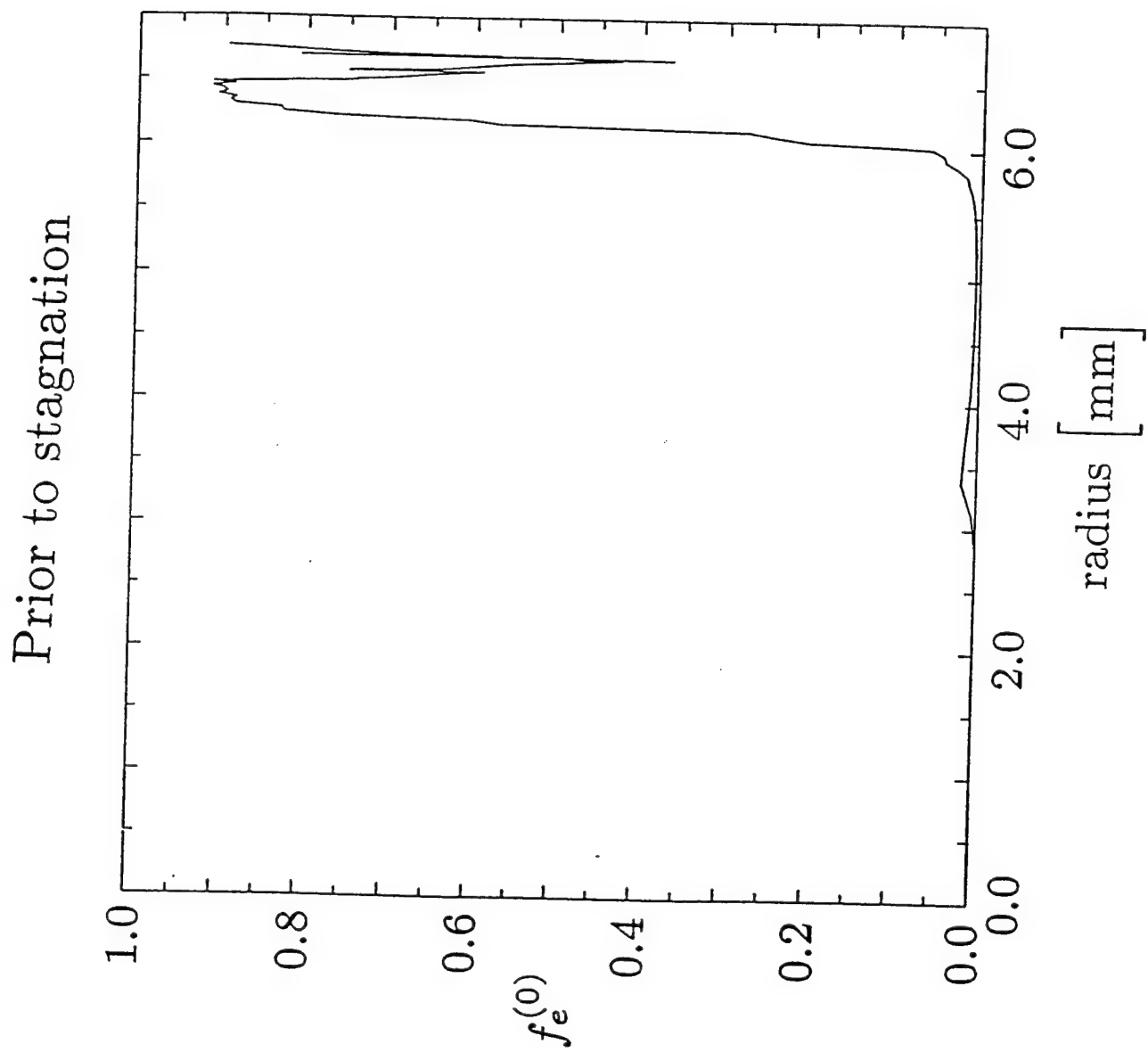


Figure 10



Prior to stagnation

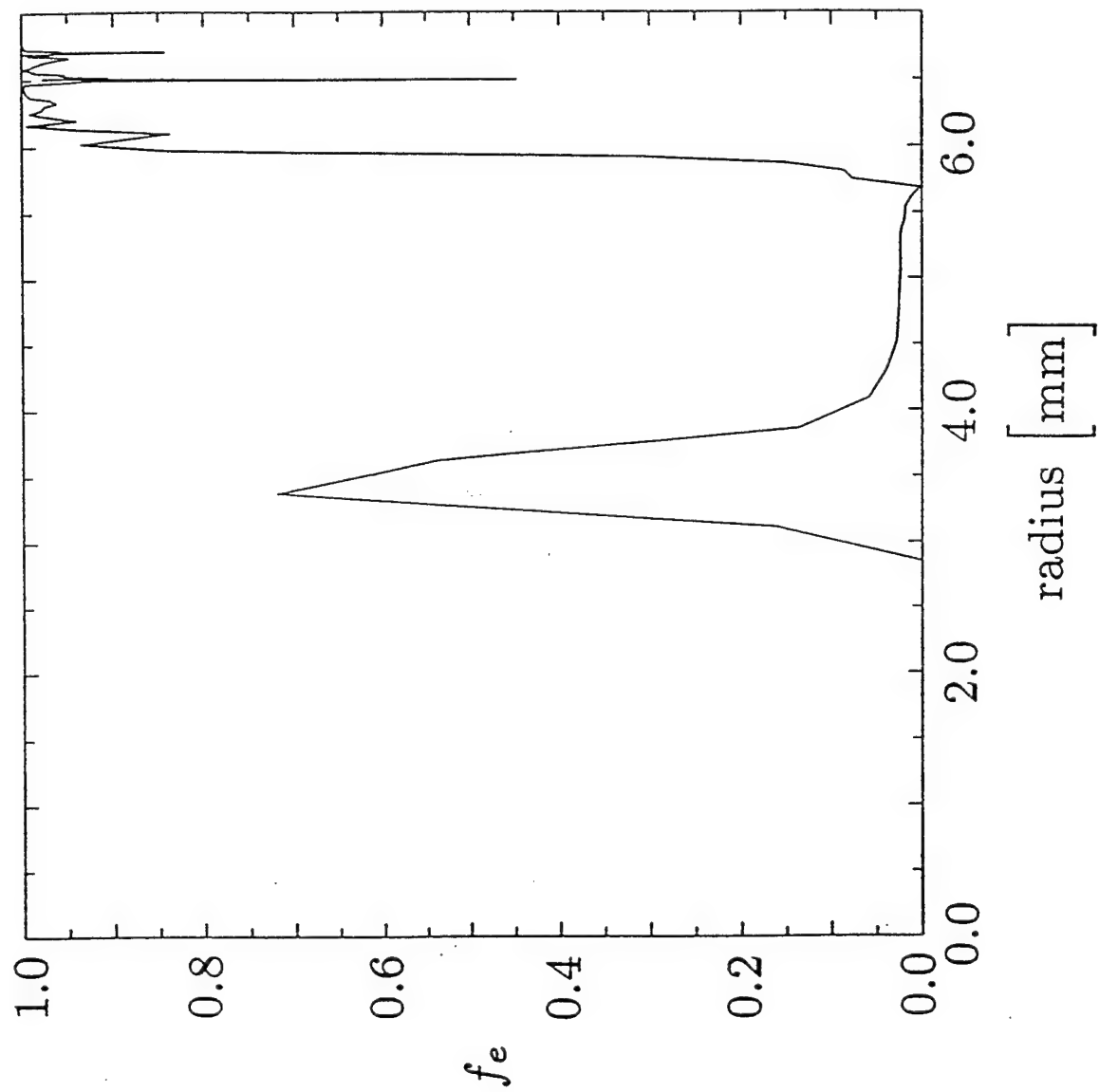


Figure 11

At stagnation

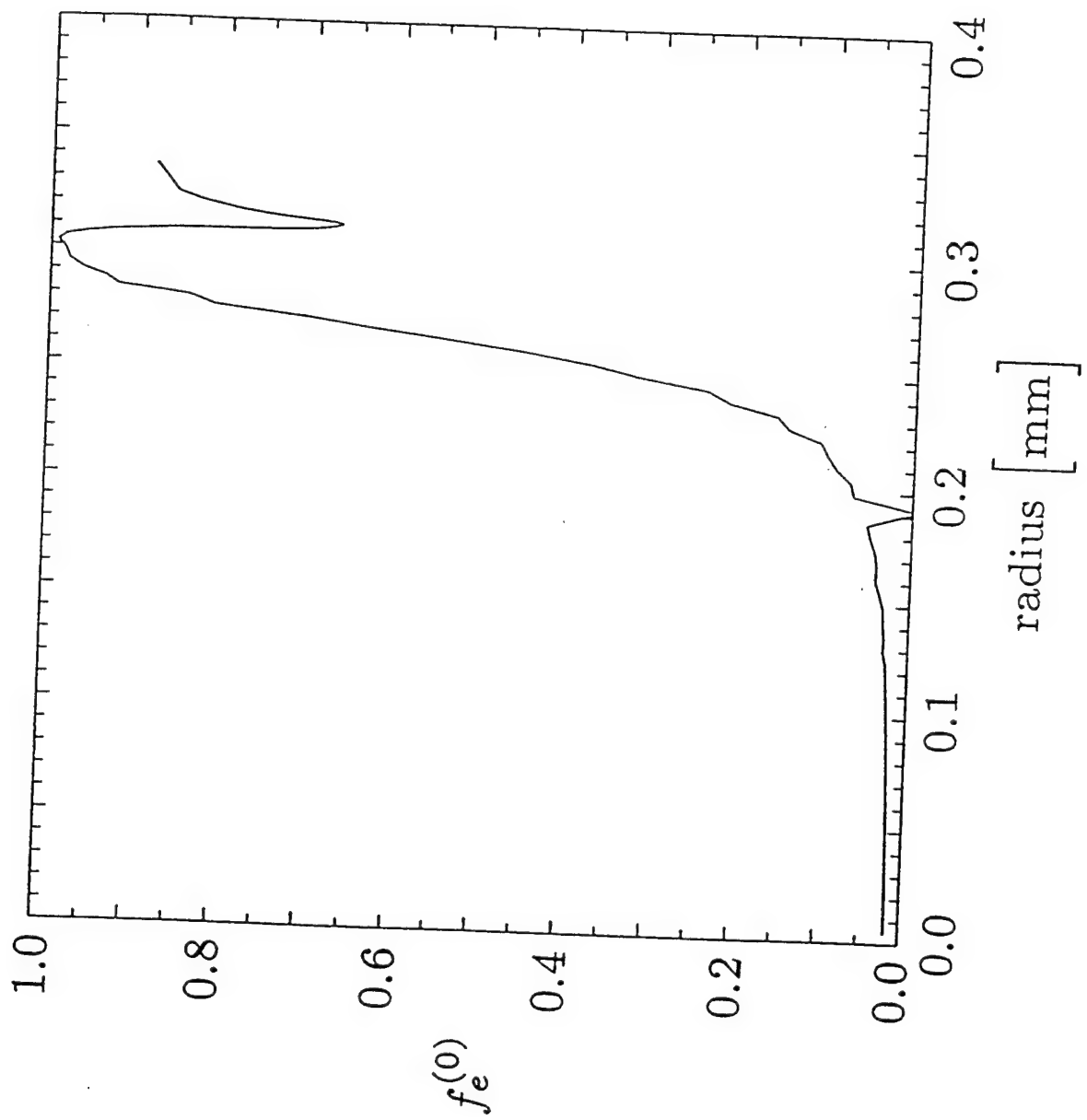


Figure 12

At stagnation

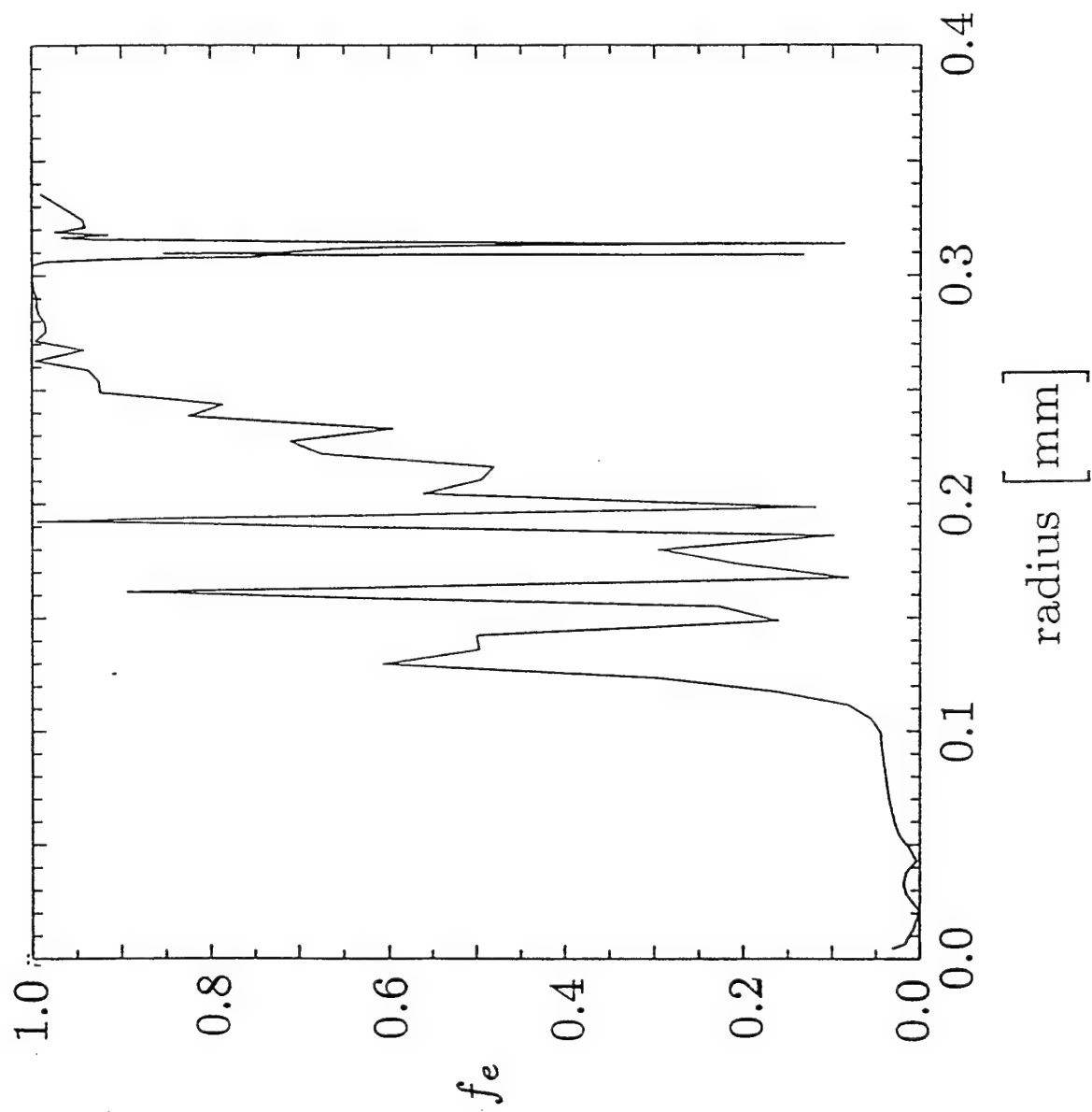


Figure 13

## IV. PERFORMANCE ASSESSMENT FOR DECADE QUAD GAS PUFF LOADS

### A. Introduction and Review of $I^2$ scaling

A long current rise time makes it essential that DECADE QUAD have the ability to efficiently extract K-shell emission from large radius loads. In this section we evaluate the future performance on DECADE QUAD of the large radius double puff nozzle load that was developed for Double Eagle and Saturn. This is a continuation of the work that was described in last years final report. In that study the 7 cm diameter uniform fill loads used in the 1998 Double Eagle and Saturn long pulse argon experiments were assessed in terms of their future performance on DECADE QUAD.

The basis of projecting the K-shell emission performance of a nozzle on one machine to its performance on a different machine in accordance with an energy or  $I^2$  scaling was outlined in the 1998 annual report. It is worth repeating the foundations, assumptions and caveats inherent in using an  $I^2$  projection:

Figure 1 displays argon K-shell yield as a function of increasing mass-per-unit length for three theoretical curves at a fixed coupled energy-per-ion,  $\eta^* = 4$ .<sup>1,2</sup> Where  $\eta^*$  is the coupled-energy-per-ion divided by  $E_{min}$  the minimum energy per ion needed to instantly heat and ionize into the K-shell upon stagnation.<sup>2</sup> For elements up to krypton  $E_{min} \simeq 1.012Z^{3.662}$  eV/ion. The first curve was obtained using a 1D radiation transport model that used classical transport coefficients in accord with some of our earliest work on K-shell yield scaling.<sup>2,3</sup> The second curve was obtained using the same 1D model with the exception that the transport coefficients were enhanced in order to match the stagnation conditions attained in a series of Double Eagle short pulse small radius aluminum experiments.<sup>4,5</sup> The third curve is very hypothetical in the sense that it is what one might obtain if one tried to match the 1D transport coefficients to the stagnation conditions attained from a series of poorly designed experiments. All three of these curves as well as many K-shell scaling experiments exhibit the characteristic  $I^4$  to  $I^2$  K-shell yield transition as a function of increasing mass load. The  $I^4$  scaling regime is characterized by radiative cooling rates that are too small to effectively influence the dynamics of the pinch. Under these low mass conditions the K-shell radiation increases at the optically thin rate, which scales as the square of the ion density ( $N_i^2$ ) or as  $mass^2$ . However at sufficiently large mass the rates will begin to affect the pinch dynamics and

the radiative yields will be limited by energy conservation to less than or equal to an  $I^2$  increase with *mass*.

Depending on the curve and mass load there can be a large range of K-shell yields spanned by the curves in Fig. 1. This is the major difficulty with using curves like these, or 0-D models based on them, to predict K-shell yield because it is not known *a priori* which curve is applicable to a given experiment. This difficulty is especially true for the larger radius experiments because they are at the frontier of new load design, where the roles that asymmetry, instability, compression, and adequate current play in influencing K-shell yield are largely unresolved. Therefore in the interest of eliminating as many model dependences as possible it was decided that it would be best to scale the experimental Double Eagle long pulse argon K-shell yields directly to DECADE QUAD using only an  $I^2$  (energy) scaling. This eliminates the need for detailed knowledge of where the  $I^4$  transition begins and ends at the sacrifice of making a conservative projection of the DECADE QUAD K-shell yield. Fig. 2 illustrates the procedure of  $I^2$  scaling by projecting a fictitious Double Eagle K-shell yield to DECADE QUAD.

The major caveat in performing an  $I^2$  projection of Double Eagle yields to DECADE QUAD is the assumption that loads using the same nozzle and that couple the same energy-per-ion (or  $\eta^*$ ) to the load behave similarly on Double Eagle as DECADE QUAD.

In order to establish continuity with this years assessment of the double puff nozzle it is worthwhile summarizing the results of last years assessment of the 7 cm diameter uniform fill loads performance:

- 1) The argon K-shell yields obtained on Double Eagle long pulse with the 7 cm diameter uniform fill load configuration  $I^2$  scales to over 40 kJ of K-shell emission on DECADE QUAD.

- 2) There is reason for concern about some of the long pulse experimental results because the maximum Double Eagle and Saturn K-shell yields were attained in a low  $\eta^*$  regime. There is theory support and experimental evidence (aluminum experiments on Saturn and Z)<sup>6,7</sup> that yield saturation can occur in this regime for large mass loads, which makes yield saturation a relevant concern for DECADE QUAD.

- 3) A comparison of the enhanced to non-enhanced voltage experimental Double Eagle K-shell

yields revealed that the 7 cm diameter uniform fill load was in an  $> I^2$  scaling regime, which implies that the 40 kJ projected DECADE QUAD yield is a conservative projection. This  $> I^2$  yield scaling also implies that the peak efficiency for K-shell yield production using the 7 cm diameter nozzle was not achieved. Experiments at higher current levels would be needed to determine this nozzle's peak efficiency. If efficiency is defined as the K-shell yield divided by the coupled energy as calculated from snowplow model with a 10:1 compression ratio, then the maximum efficiency obtained from the 7 cm diameter uniform fill Double Eagle long pulse experiments was 15 % (17.3 kJ/112 kJ). For comparison purposes the efficiency for the optimal short pulse argon load is 23 % (22 kJ/96 kJ).

## B. $I^2$ scaling of 1999 double puff experiments to Decade Quad

Figure 3 is a schematic diagram of the double puff nozzle employed in the 1999 DTRA sponsored gas puff experiments. The outer puff has an outer radius of 4 cms and an inner radius of 3 cms, whereas the inner puff has an outer radius of 2 cms and an inner radius of 1 cm.<sup>8</sup>

There are five Double Eagle shots that are analyzed and they are shown in Figure 4. They range in implosion times from 212 ns to 170 ns. The peak K-shell yield was 12 kJ, which occurred at an implosion time of 187 ns. Table I shows the results of our  $I^2$  scaling analysis of these shots. The implosion times, load mass, experimental K-shell yields, achieved  $\eta^*$  values, and Double Eagle peak current values are shown in Table I. The modeled Decade Quad peak currents and projected K-shell yields are shown in the last two columns of Table I.

The yield projection of Double Eagle shot number 2 to Decade Quad is about 36 kJ for a 4 cm length load. This yield projection as well as the  $\eta^* = 1.4$  value for which it was obtained are in good agreement with the projections from the 1998 Double Eagle uniform fill experiments.

A series of long pulse mode Saturn experiments also took place in 1999. The five shots we analyzed are shown in Figure 4. The peak experimental Saturn current as well as the modeled Decade Quad peak currents are shown in this figure as a function of mass load. Limitations on load inductance limited the length of the Saturn loads to 2 cm whereas the Decade Quad currents, displayed in Figure 4 are taken from a 4 cm length load analysis. Nevertheless, where ever the Saturn current lies above the Decade Quad current in this figure one expects the projected Decade

Quad K-shell yield to be smaller than the attained Saturn yield on a per-unit-length basis. This expectation is verified in Table II, which displays the Saturn data and Decade Quad projections in the same manner as was done in Table I for Double Eagle. For Saturn it is found that the highest projected yield to Decade Quad is about 25 kJ for a 4 cm length load. This projection is considerably lower than the 36 kJ optimal projection from the Double Eagle experiments.

A likely reason for this difference in Decade Quad projected K-shell yields between Saturn and Double Eagle is because of K-shell yield saturation in the low  $\eta^*$  scaling regime. The possibility that yield saturation in this regime could be an issue for Decade Quad was mentioned above and in last years annual report. Table III compares the experimental Saturn K-shell yields with the results of an analysis whereby the Saturn K-shell yields are projected from the Double Eagle experiments. This comparison clearly shows that for the lower  $\eta^*$  values the Saturn experiments are in a saturated ( $< I^2$ ) scaling regime whereas for the higher  $\eta^*$  values the experiments are in a  $> I^2$  regime.

A theoretical plot of titanium K-shell yield as a function of mass load is shown in Figure 5 for  $\eta^* = 1, 2$  and 3 in order to help explain the dynamics of K-shell yield saturation. One can clearly see from these theoretical curves that the K-shell yield is saturated for the  $\eta^* = 1$  curve. In these calculations the coupled energy is thermalized in accord with an energy ( $I^2$  or *mass*) scaling whereas the radiative cooling rate scales as *mass*<sup>2</sup>. Because the cooling rate is increasing faster than the heating rate as the mass load is increased (at least until opacity limits radiative losses) the plasma as a whole will have a progressively lower temperature. As the temperature drops below what is needed to ionize into the K-shell then the K-shell yield will saturate or decline as mass is increased further. Since the low  $\eta^*$  loads have the least energy-per-ion available to start with, they will be the first to exhibit the effects of yield saturation.

## C. Conclusions

There are at least two major conclusions from this years gas puff PRS performance assessment for Decade Quad. First, that K-shell yield saturation in the low  $\eta^*$  scaling regime is a potential problem for Decade Quad. In order to overcome this problem we need to implode higher  $\eta^*$  loads that make efficient usage of Decade Quad's available energy. This can be done by going to larger radius loads or by putting a larger fraction of the mass into the outer annulus of the double puff

nozzle. The second conclusion is that one of the requirements of  $I^2$  scaling of K-shell emission from one machine to another is that the load behavior be the same on both machines. Based on the strange shape (abrupt flattening of the current profile) of the Saturn peak current profile shown in Figure 4 and the fact that Saturn could not effectively implode 4 cm length loads, it is clear that Saturn with its smaller front end inductance ( $\sim 10$  nh) cannot deliver energy to a 4 cm length (possibly a 2 cm length load) load at stagnation as effectively as Double Eagle ( $\sim 25$  nh). This is an issue for Decade Quad because its front end inductance is only about 9 nh.

## References

1. J. W. Thornhill, K. G. Whitney, J. Davis, and J. P. Apruzese, *J. Appl. Phys.* 80, July 15, (1996).
2. K. G. Whitney, J. W. Thornhill, J. P. Apruzese, and J. Davis, *J. Appl. Phys.* 67, 1725 (1990).
3. J. W. Thornhill, K. G. Whitney, and J. Davis, *J. Quant. Spectrosc. Radiat. Transfer* 44, 251 (1990).
4. C. Deeney, T. Nash, R. R. Prasad, L. Warren, K. G. Whitney, J. W. Thornhill, and M. C. Coulter, *Phys. Rev. A* 44, 6762 (1991).
5. J. W. Thornhill, K. G. Whitney, C. Deeney, and P. D. LePell, *Phys. Plasmas* 1, 321 (1994).
6. C. Deeney, T. J. Nash, R. B. Spielman, J. F. Seaman, J. S. McGurn, D. O. Jobe, M. F. Vargas, T. L. Gilliland, R. C. Mock, K. W. Struve, K. G. Whitney, P. E. Pulsifer, J. P. Apruzese, J. W. Thornhill, and J. Davis, *Phys. Plasmas* 5, 2431 (1998).
7. J. P. Apruzese, P. E. Pulsifer, J. Davis, R. W. Clark, K. G. Whitney, J. W. Thornhill, T. W. L. Sanford, G. A. Chandler, C. Deeney, D. L. Fehl, T. J. Nash, R. B. Spielman, W. A. Stygar, K. W. Struve, R. C. Mock, T. L. Gilliland, D. O. Jobe, J. S. McGurn, J. F. Seamen, J. A. Torres, and M. Vargas, *Phys. Plasmas*, 5, 4476 (1998).
8. This schematic diagram was obtained from Bruce Weber of NRL.



# I<sup>2</sup> Scaling of the Double Puff Nozzle Results on Double Eagle to DECADE QUAD

Shot DE	$\tau$ (ns)	Mass ( $\mu\text{g/cm}$ )	DE K yield	$\eta^*$	DE I (MA)	DQ I (MA)	Proj DQ K-yield
1	211	212	2.0 kJ/cm	1.3	3.8	7.1	7.0 kJ/cm
2	206	200	2.7	1.4	3.8	6.9	8.9
3	187	145	3.2	2.0	3.8	5.8	7.3
4	176	118	2.4	2.4	3.8	5.5	5.0
5	170	100	1.4	2.6	3.8	5.3	2.7

Projected DQ K-yield <sub>(fixed  $\eta^*$ )</sub> = Double Eagle yield <sub>(fixed  $\eta^*$ )</sub> x (IDQ/IDE)<sup>2</sup>

Table 1

# $I^2$ Scaling of the Double Puff Nozzle Results on Saturn to Decade Quad

Shot SAT	$\tau$ (ns)	Mass ( $\mu\text{g/cm}$ )	SAT K yield	$\eta^*$	SAT I (MA)	DQ I (MA)	Proj DQ K-yield
1	207	630	4.1 kJ/cm	1.3	6.6	7.1	4.7 kJ/cm
2	172	390	6.8	2.1	6.6	5.8	5.2
3	156	285	7.5	2.4	6.0	5.5	6.3
4	146	250	7.4	2.5	5.8	5.3	6.1
5	131	175	6.2	3.2	5.5	4.8	4.6

Projected DQ K-yield  $\underset{\text{(fixed } \eta^*)}{=}$  Saturn yield  $\times \left( \frac{I_{DQ}}{I_{SAT}} \right)^2$   
 $\underset{\text{(fixed } \eta^*)}$

Table 2

K-shell yield saturation in the low  $\eta^*$  scaling regime at large mass load is an issue for Decade Quad

$\eta^*$	Sat Mass ( $\mu\text{g}/\text{cm}$ )	DE Mass ( $\mu\text{g}/\text{cm}$ )	Proj. SAT K-yield from DE (kJ/cm)	Realized SAT K-yield (kJ/cm)
1.3	630	212	6.0	$4.1 < I^2$
2.1	390	140	9.4	$6.8 < I^2$
2.4	285	118	6.6	$7.5 > I^2$
2.5	250	105	5.1	$7.4 > I^2$
3.2	175	80		6.2

Table 3

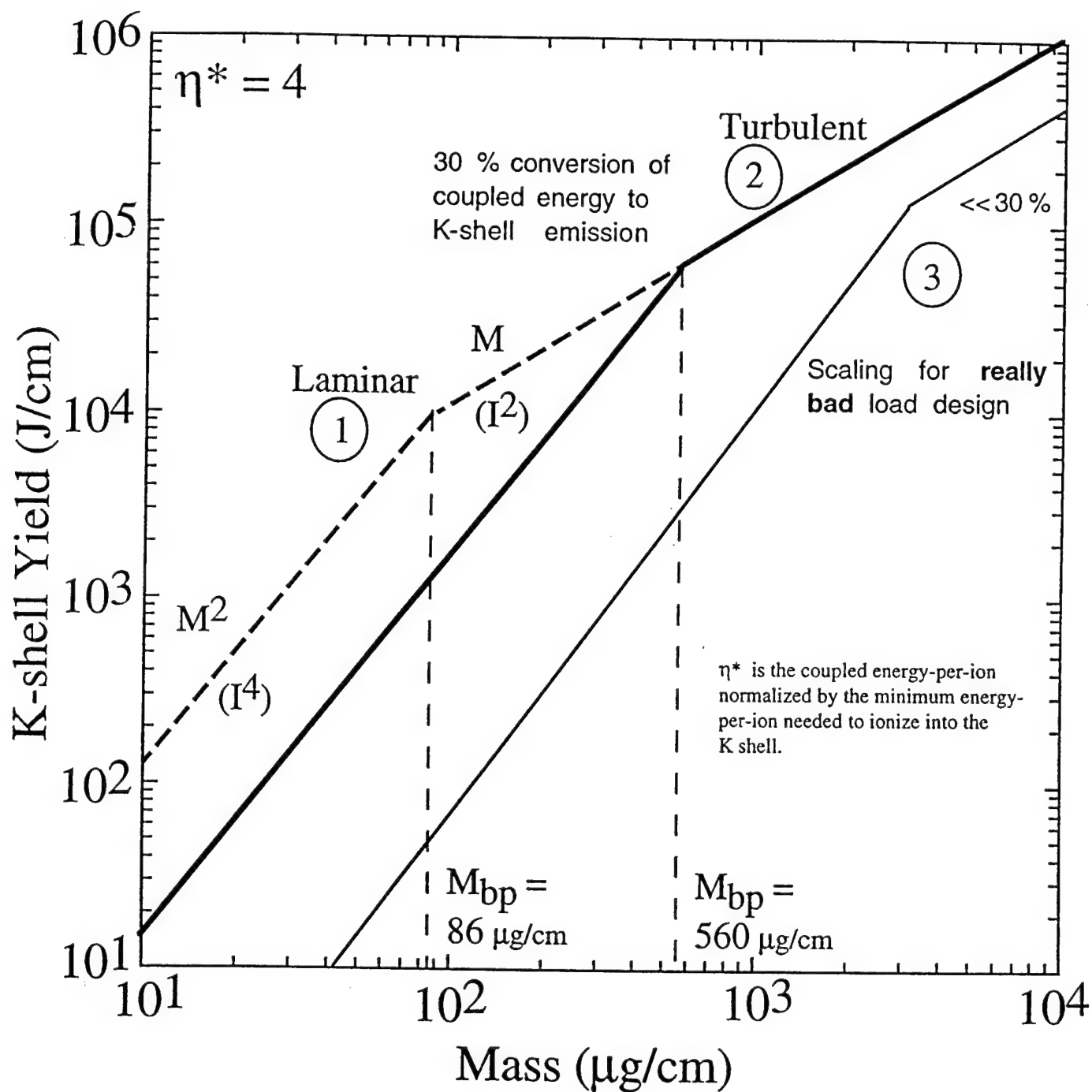


Fig. 1 K-shell yield as a function of mass for three 1D model conditions.

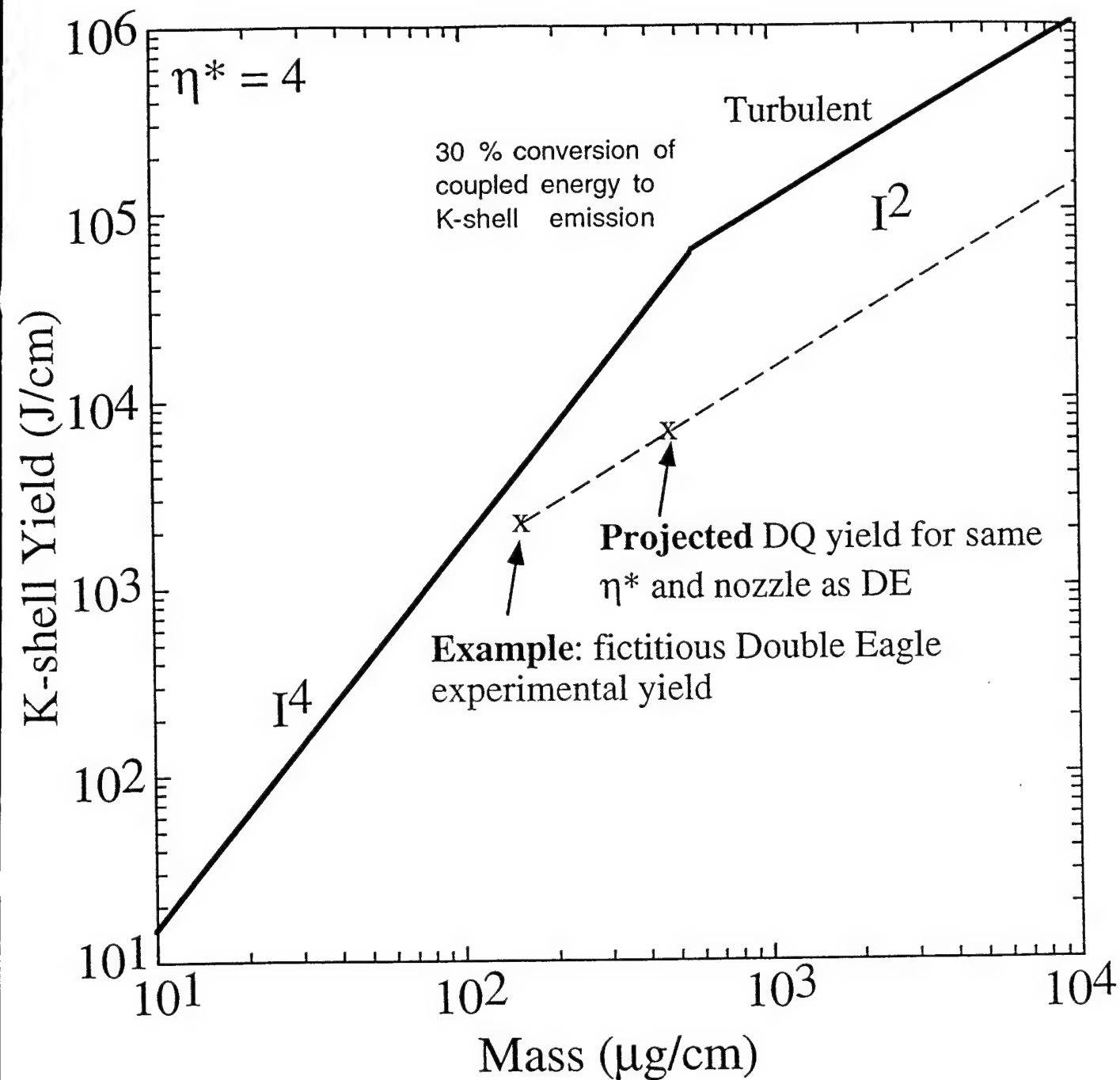


Fig. 2 Example of energy ( $I^2$ ) scaling of Double Eagle K-shell yields to Decade Quad.

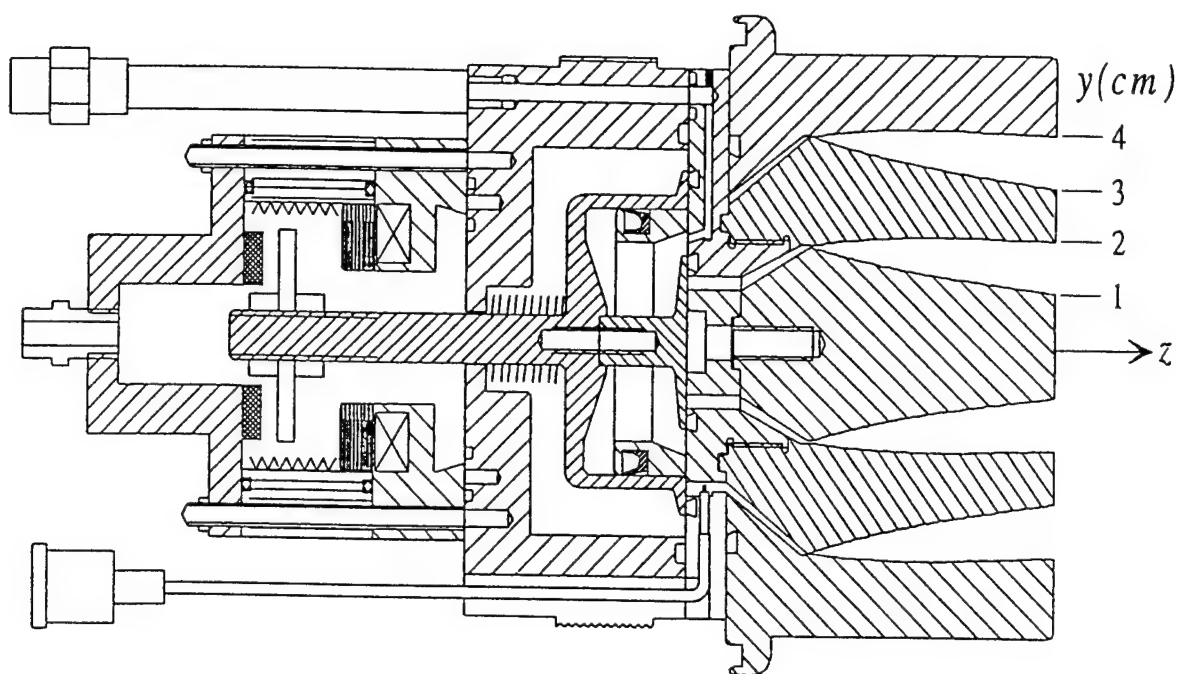


Fig. 3 Double Eagle double puff PRS nozzle  
(obtained from Bruce Weber of NRL)

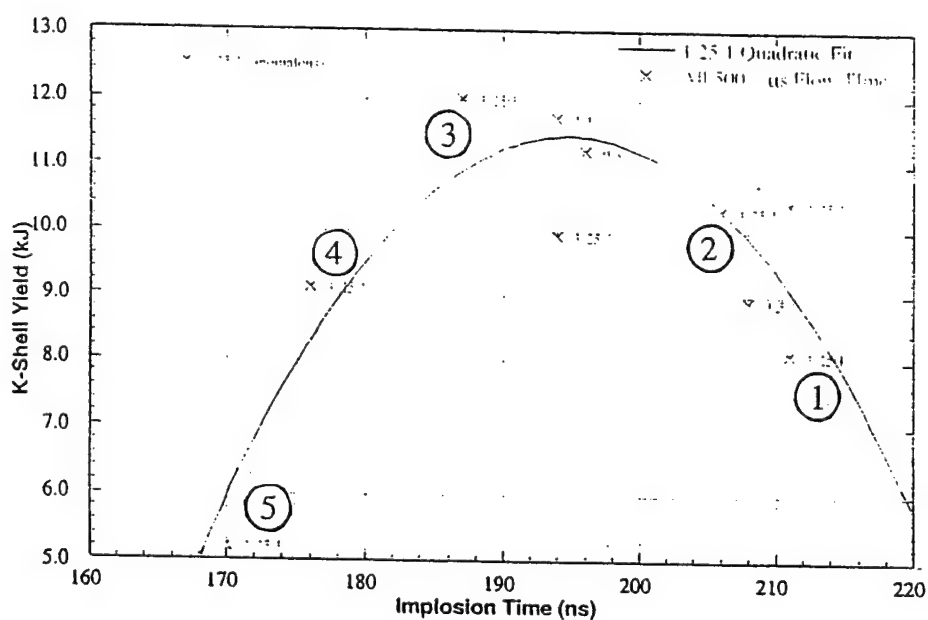


Fig. 4 Yield vs implosion time for 500  $\mu$ s flow time at various inner:outer pressure ratios for the Double Eagle long pulse double puff nozzle (obtained from Maxwell-PI Technologies).

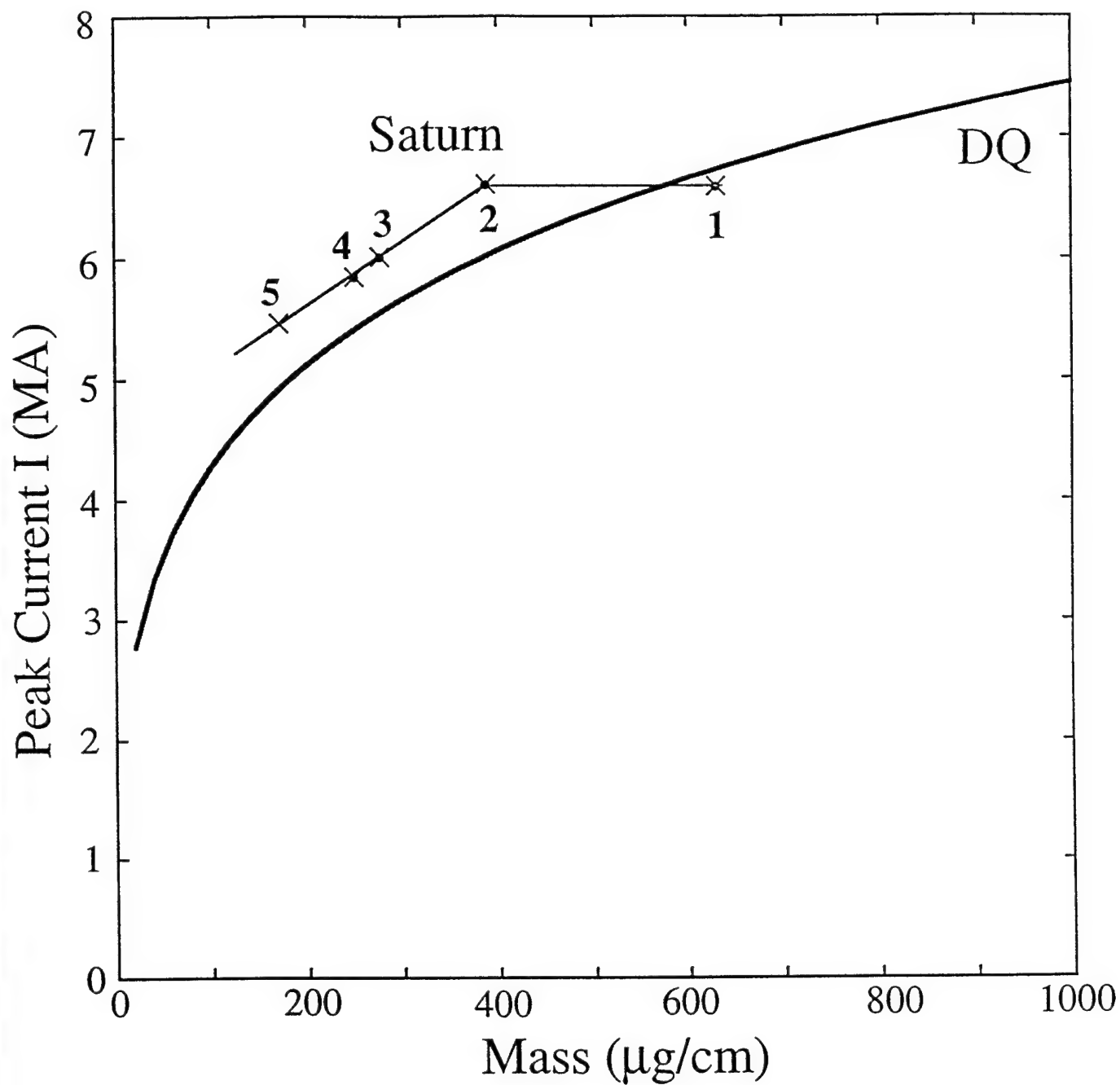


Fig. 5 Current Profile Versus Mass for Saturn and DQ for the Double Puff Nozzle

## V. Novel Approach to Producing ~10 keV X Rays with Plasma Radiation Sources Powered by Long Pulse Drivers

There is renewed interest in developing a Plasma Radiation Source (PRS) that can both harden the spectra and enhance K-shell radiation yields and possibly be a method for filling-in the low energy region of the bremsstrahlung spectra. A number of viable pulsed power design options exist that are reasonably cost effective for the design and construction of a novel generator with energy in the primary storage of the order of 24 MJ and the output current ~25 MA with the rise time between 250 and 400 ns [1].

Recall that the significant progress in nanosecond pulse power technology in the 1980-90s lead to successive creation of record-high power facilities at Sandia (from Saturn to PBFA-II to Z). This approach is based on the module principle which requires advanced and very expensive technique of adding energy fluxes that come from a large number of modules, whose output has to be synchronized through many switches by the powerful laser. An alternative Maxwell/PI approach [1] is directed to less costly options. Decreased energy cost comes at the expense of longer current pulses. This leads to a relatively unexplored territory of generating 1 to 13 keV x-rays using 300 ns or longer time PRS implosions.

Simulations performed at NRL [2] have identified one of the main problems of generating a harder spectra, even at 60 MA and 100 ns rise time. The energy exchange between electrons and ions is slow, requiring thousands of electron-ion collisions, and most of the electron energy could be lost through softer radiation of lower shells before the H- and He-like ionization states could be achieved. The only way of minimizing these losses is to increase simultaneously the stagnated plasma density and its confinement time. Then opacity would help decrease the low-energy radiative losses, and we will have enough time for ionization:



The increase in stagnated plasma density due to increased radial compression ratio is limited by the Rayleigh-Taylor (RT) instability of acceleration. Without any mitigation, the compression ratio does not exceed 10-15. A number of techniques for mitigating the RT instability, like use of nested wire arrays or double puffs [3] can effectively increase the compression ratio to ~20-30.

The use of long-pulse implosions makes RT instability a more serious problem, since a matched Z-pinch load should be accelerated from a larger initial radius. Then the final radius would be larger, and the peak density accordingly lower.

It should be emphasized that the problems discussed above are mostly important for generating >10 keV energy quanta. As for the Ar to Ti K-shell energy range, the available experimental data could be reliably scaled up to target 300 kJ yield [4].

In this White Paper, we describe three recent advancements that all lead to substantial increase in density at stagnation and confinement time of imploded Z-pinch plasmas that could help solve the problem of generating substantial yields of ~10 keV quanta using low-cost pulsed power.

1) The theory of enhanced energy deposition in Z-pinch plasmas, which has been observed in many experiments but is mostly important in long implosions (e. g., see [5]) has been developed. This theory takes into account convection of magnetic flux to the pinch axis that helps couple a large amount of magnetic energy from the vacuum cavity surrounding the pinch to the pinch plasma [6]. In long implosions, the energy coupled this way could exceed thermalized kinetic energy by a factor of 2 to 3 [5, 6]. As a result, more plasma could be maintained at a high temperature for a longer time.

2) The most direct way of increasing plasma density in the pinch at given temperature is to increase the pinch current. It turns out that for a given pulsed power driver that provides a certain peak current, the current that implodes the pinch could be increased by a factor of  $\sim 2$  within the load unit. The concept of current multiplication suggested by O. Zucker can be presented in several modifications. The simplest one, which does not include any current switches, is outlined below. A schematic of this compact current multiplier is shown in Fig. 1.

3) Tighter pinches could be obtained if an implosion starts from a smaller initial radius. Energy efficiency requires matching of the imploding load to the current generator, so that an implosion from a small radius could be effectively driven by a long current pulse generator only with some kind of a switch capable of increasing the current rise rate. However, so far the attempts to create "cheap" switches (so called POS) which could deliver without significant losses an output 10 MA or more current pulse with hundred nanoseconds rise time on the load were not successful. One of the reasons is that the current disruption in POS operation is hard to control since it involves some new physics, which is still far from being well understood. Moreover, in contrast with the POS design, the switching and load sections of the inductive switch are spatially separated, so that no plasma from the switching section reaches the imploding load.

Our new approach to current switching, inductive switch or  $L\text{-dot}$  switch, does not include any current disruption. It is based on conventional electrical engineering, and should therefore be very reliable. The switch includes two sections that contain cylindrical wire-array loads, connected in parallel to the power source. Initially, inductance of the first, switch section, is lower than that of the main, load section, so that the current starts flowing primarily through the first wire array. As it implodes toward the axis, it opens a large

cylindrical cavity, rapidly increasing its inductance. Then the current is rapidly switched to the load wire array. 0-D simulations have shown that the current rise rate could be increased by the factor of 5-10 with the 80% efficiency of energy transfer to the load. A schematic of the inductive current switch is shown in Fig. 2.

Enhanced power dissipation has been described in detail in a paper [6] that has already been presented to DTRA. Here, we only present the explicit formulas for enhanced dissipation power and the corresponding effective additional non-linear resistance derived from this theory:

$$P_{enh} = \frac{I^3 l}{2\mu^{1/2} c^3 R} = \frac{I^3 (\text{MA}) l (\text{cm})}{2\mu^{1/2} (\mu\text{g/cm}) R (\text{mm})} \text{ TW},$$

and

$$\mathcal{R}_{enh} = \frac{Il}{2\mu^{1/2} c^3 R} = \frac{I (\text{MA}) l (\text{cm})}{2\mu^{1/2} (\mu\text{g/cm}) R (\text{mm})} \text{ Ohm}.$$

Below, we discuss in more detail the concept designs of compact current multiplier and inductive switch.

The compact current multiplier (CCM) presented here is a device placed on the front-end of existing or designed pulsed power driver. CCM does not require the additional switches. This device includes two loops of input current  $I(t)$  from the generator. The load (imploding shell) is a part of a double-turn current loop. Schematic of this design of CCM is presented on Fig.1. The device is connected to the output of the driver.

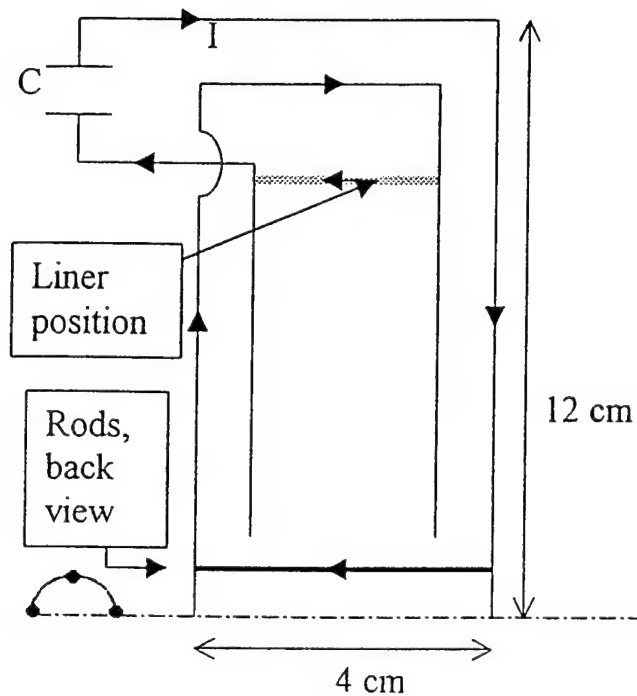


Figure 1.

The current  $I$  flows along the internal surface of the external coaxial  $c_2$ , then through the array of rods 3. Then the current flows upward in positive radial direction, then follows the “second loop” along the cylindrical section  $c_1$ , then through the load wire array, and then, through the convolution hole in the “second loop”, back to the driver. As a result, the load wire array is accelerated by the magnetic fields of the double current  $2I$ , and decelerated by the field of a single current  $I$ . The resulting increase in the accelerating magnetic pressure is 3-fold. The accelerated shell implodes, moving along the parallel disc-like “second loop” electrodes. At the end of acceleration, the plasma penetrates through the array of rods 3 and stagnates at the axis.

0-D simulation of the CCM operation has been done for the parameters of the pulsed power driver discussed in [1]. The front-end inductance, including the initial inductance of the CCM device, was taken 35 nH. The amplitude and time of current rise nearly correspond to those given in [1]. Optimization was made for final velocity  $V \approx 10^8$  cm/s. It was shown that the kinetic energy of the plasma shell, 3.75 MJ, corresponds to a 1.5 cm shell length and its mass 5 mg/cm. Compare it to the result of a similar simulation done for a conventional, "single-turn" load unit of the same initial inductance. In the latter case, the kinetic energy 3.3 MJ corresponds to the imploding shell length 4 cm and mass 1.7 mg/cm. The energy per unit length delivered to the load, which is the key figure-of-merit for a high-Z K-shell production, is increased by a factor of 3 due to the use of CCM.

There is a chance that a more advanced version of this design could work, incorporating all the ideas described in the White Paper. In this approach, the array of a few rigid rods 3 is replaced with a regular wire array, whose mass is comparable to that of the main array, the two thus forming a nested array configuration. Initially, the two arrays are effectively connected in series. The inner array is mounted at approximately half radius of the main array. Since the main array is accelerated by a double magnetic field, it implodes faster, and at some point collides with the inner array. As a result, some mitigation of the RT growth in the colliding wire arrays could be expected, and the assembled plasma shell continues to be accelerated by the pressure of double magnetic field. This is because during the short time interval before stagnation the magnetic flux stored in the mutual inductance has no possibility to decrease significantly.

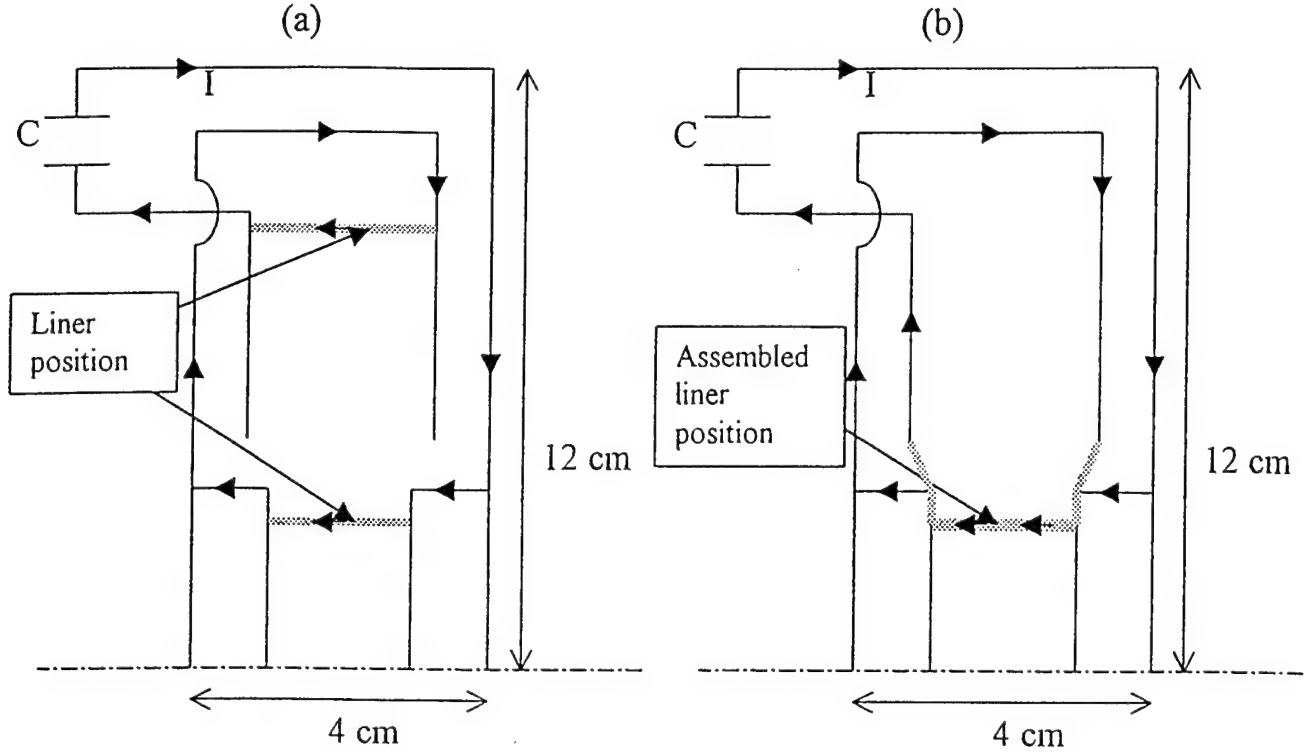


Figure 2.

Schematics of the inductive switch is presented in Fig.3 The equivalent electrical circuit for inductive energy store  $L_0$  is presented in Fig 3 (top) explains the principle of operation of this device. If the energy store is capacitor C as in DQ generator the electrical circuit is different: we should replace  $L_0$  by C, add switch to connect capacitor C with inductive energy store section, which supply by energy main imploding shell L2 (PRS) through inductive switch ( $L_1, L_2$ ). For this case  $R_S$  and  $R_{LOAD}$  are nearly zero.

Inductance  $L_1$  of cavity 1 rises in time when the plasma shell 1 implodes to the axis. If the radius of the cavity  $R_0 = 8$  cm, its length  $z_0 = 20$  cm, then  $L_1 = 50 - 100$  nH. When the wire array shell 1 cm long in the small section of cavity 1 just begins to accelerate by the current pulse increasing to  $I_{max}$  during 200 - 300 ns, the impedance  $L_1$  is small and only small part of

current flows through load in cavity 2. But when the current shell moving at the velocity  $\approx 10^8$  cm/s had open the hole with a radius  $\rho = 1\text{-}2\text{cm}$  in a big

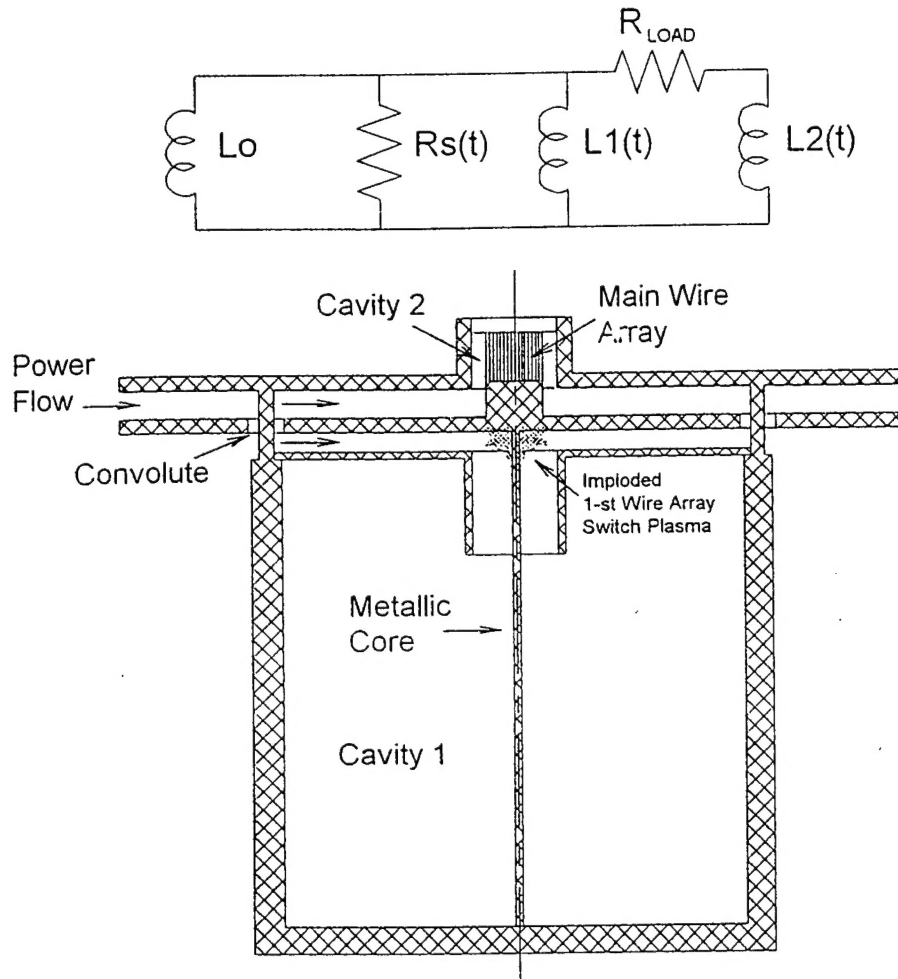
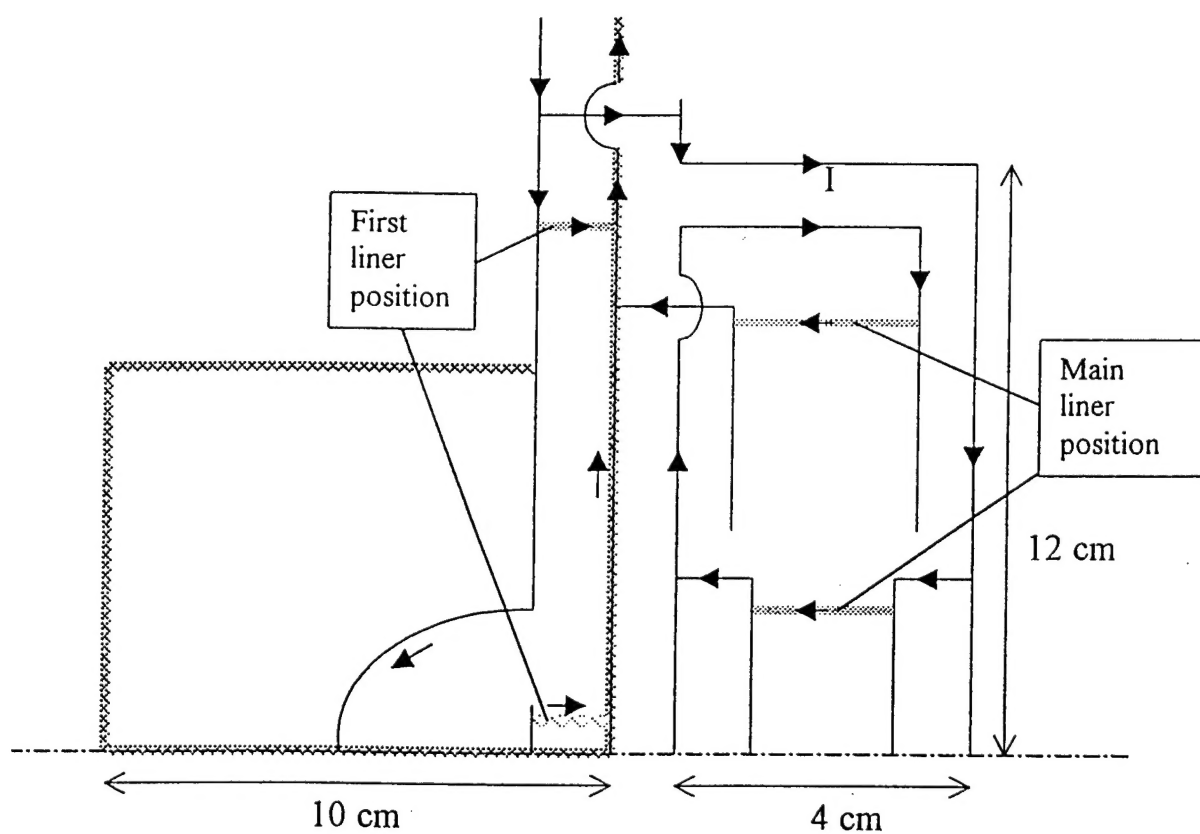


Figure 3. Inductive Switch

volume of cavity 1, then more current flows through the cavity 2. And significant part of magnetic energy stored in Pulse Power Generator could dissipate into cavity 2. It happens during the last 30 ns. To avoid enhanced energy dissipation in cavity 1 [5], metallic cylinder, diameter 4-6 mm, is placed on the axis. D. Peterson simulated imploding plasma behavior near a hole. Only a few percent of shell plasma passed through the hole. 2-D MHD simulations made by A. Chuvatin and S. Zakharov have confirmed the basic physics and performance parameters of a multi-MA inductive switch [7].

The inductive current switch could be combined in one load unit with the multiplier. In particular, this could be done with the version of the load design presented in Fig. 2, where the nested wire array technique of the RT instability mitigation is incorporated, and the additional energy could be coupled to the pinch stagnated at the axis through the enhanced dissipation mechanism. A schematic of this load unit is shown in Fig. 4.

Figure 4.





### Current status and suggestions

1) Existence of enhanced energy deposition has already been confirmed by a number of experiments, including the most relevant long-implosion experiments organized by DTRA [4] and in 2-D simulations.

2) Operation of the compact current multiplier could be tested on one of the existing multi-MA current generators. For example, we can use Double Eagle at 4 MA in the long pulse mode. According to the above estimates, this could effectively increase radiation production capacity of Double Eagle to the level approaching Saturn and offer the opportunity to produce harder K-shell radiation (Fe, Ni).

3) It would be very important to test the operation of the inductive current switch on one of the existing generators, or, in the near future, on Decade-Quad.

4) The proof-of-the-principle experiments with a current multiplier and the inductive switch, if successful, would create a firm basis of combining the novel load design concepts discussed above into a front-end device capable of producing the desired yield of  $\sim 10$  keV quanta on the pulsed power generator described in [1].

5) Before this is done, it would be helpful to do radiation hydro simulations for the best-case scenario, to find out if the plasma parameters that could be reached using the above approach are sufficiently high to produce efficient Kr K-shell generation. Alternatively, this could be regarded as a search for the main parameters (current, plasma density and confinement time) that are sufficient to generate substantial 10 keV yield and at the same time could be approached using novel load design.

## References

- [1] P. Sincerny *et al.*, "Concepts for Affordable High Current Imploding Plasma Generator", presented at the 1999 IEEE International Conference on Pulsed Power, June 28-30, 1999, Monterey, CA.
- [2] J. Davis *et al.*, in BEAMS'96, Proc. of the 11<sup>th</sup> International Conf. On High-Power Particle Beams, Prague, June 10-14, 1996, edited by K. Jungwirth and J. Ullschmied, v. 2, p. 70.
- [3] J. Davis *et al.*, Appl. Phys. Lett. 70, 170 (1997); C. Deeney *et al.*, Phys. Rev. Lett. 81, 4883 (1998); H. Sze *et al.*, "Dynamics of a Z-Pinch Using a Double Gas Puff" (1999).
- [4] C. Deeney *et al.*, Phys. Plasmas 6, 2081 (1999).
- [5] M. R. Douglas *et al.*, in IEEE Conference Record – Abstracts, 1999 IEEE International Conference on Plasma Science, June 20-24, 1999, Monterey, CA, p. 230; C. Deeney *et al.*, *ibid*, p. 232; C. Deeney *et al.*, Phys. Plasmas 6, 3576 (1999).
- [6] A. L. Velikovich *et al.*, submitted to Phys. Plasmas (1999).
- [7] A. Chuvatin and S. Zakharov, Post-deadline poster presented at the 1999 IEEE International Conference on Pulsed Power, June 28-30, 1999, Monterey, CA.